UNIVERSITÉ DU QUÉBEC À MONTRÉAL

METAL ION DETECTION IN LI-ION BATTERIES ELECTROLYTE USING SECM

DISSERTATION
PRESENTED
AS PARTIAL FULFILLMENT
OF THE DOCTORATE IN CHEMISTRY

BY
MOJGAN HATAMI

AUGUST 2022

UNIVERSITÉ DU QUÉBEC À MONTRÉAL

DÉTECTION D'IONS MÉTALLIQUES DANS L'ÉLECTROLYTE DE BATTERIES LI-ION À L'AIDE DE SECM

THÈSE
PRÉSENTÉE
COMME EXIGENCE PARTIELLE
DU DOCTORAT EN CHIMIE

PAR
MOJGAN HATAMI

AOÛT 2022

ACKNOWLEDGEMENTS

I would like to express my gratitude and appreciation for Prof. Steen Schougaard whose guidance, support and encouragement has been invaluable throughout this study. Also I would like to thank to Prof. Janien Mauzeroll for her assistance and editing the manuscripts of my articles.

From the bottom of my heart, I would like to say big thank you for my dear friend Elena Rezaie for her kind assistance and all Prof. Schougaard's research group members for their energy, understanding and help throughout my project, especially to Isabelle Beaulieu, Laurence Savignac, Jeremy Dawkins, Fariborz Chitsazzadeh, Anjana Raj, Dr. Andrew Danis, Dr. Mohammadreza Ghavidel, Dr. Sazzad Mohammad Hossain, Islam-Samah Asselah and Dr. David Polcari for all the assistance they have provided and also Prof. Joshua Byers, Prof. Ali Nazemi and Prof. Guillaume Goubert, for providing helpful comments and accompanying me in my research work.

Thanks to Nanoqam especially to Gwénaël Chamoulaud and Galyna Shul and all the participants that enabled this research to be possible.

Finally, I would like to thank my family that supported me during my studying years.

DEDICATION

To my family, my kind husband Payam, and my lovely twins Katayoon and Homayoon.

TABLE OF CONTENTS

LIST OF FIGURES

LIST OF ABRREVIATIONS

A15C5	aza-15-crown-5 ether
AdSV	adsorptive stripping voltammetry
ASV	anodic stripping voltammetry
CE	counter electrode
CG	collection/ generation mode
CNT	carbon nanotubes
CSV	cathodic stripping voltammetry
CV	cyclic voltammetry
DEC	diethyl carbonate
DMC	dimethyl carbonate
DPV	different pulse voltammetry
EC	ethylene carbonate
EV	electric vehicles
GC	glassy carbon

HEV	hybrid electric vehicles
HMDE	hanging mercury drop electrode
ISE	ion selective electrode
LFP	lithium iron phosphate
Li_2IDA	dilithium iminodiacetate
LIB	lithium ion battery
LiTFSI	lithium bis (trifluoromethanesulfonyl)imide
LMO	lithium manganese oxide
LMP	lithium manganese phosphate
LOD	limit of detection
LSV	linear sweep voltammetry
Min	minute
MV	methyl viologen dichloride hydrate
NMP	n-methyl-pyrrolidone
OPC	organic photovoltaic cell
ORR	oxygen reduction reaction,

O/R reaction	oxidation/reduction reaction
p-BQ	*p*-benzoquinone
PC	propylene carbonate
PHEV	plug-in hybrid electric vehicles
PVDF	poly vinylidene fluoride
QRCE	quasi-reference counter electrode
RC-SECM	Redox competition mode
RF	reference electrode
SECM	scanning electrochemical microscopy
SEI	solid electrolyte interface
SG/TC	substrate generation/tip collection
SHE	standard hydrogen electrode
SICM	scanning ion conductance microscopy
SMCM	scanning micropipette contact method
SPE	solid polymer electrolytes
SPM	scanning probe microscopy

SV	stripping voltammetry
SWV	square wave voltammetry
$TEABF_4$	tetraethylammonium tetrafluoroborate
TG/SC	tip Generation/substrate Collection
TiO_2	titanium dioxide
TMF	thin mercury film electrode
UME	ultra microelectrode

LIST OF SYMBOLS AND UNITS

°C	degree Celsius
µA	micro ampere
µm	micro meter
$1/\tau$	frequency of the SWV
A	ampere
a	radius of microelectrode
C_i	concentration of species i
cm	centimeter
d	current-surface distance in approach curve
D	diffusion coefficient (m^2/s)
ΔC	gradient of concentration
D_i	diffusion coefficient of species i
ΔV	gradient of potential

E	potential
E^0	standard potential
E_{eq}	potential at equilibrium
E_{sample}	potential of sample
E_{step}	step size (potential) in SWV
E_{sw}	pulse amplitude in SWV
F	Faraday constant (96485 s A mol^{-1})
g	gram
h	hour
I	current
I_f	current response for the direct potential sweep in SWV
I_r	current response for the reverse potential sweep in SWV
i_T	current of the tip of SECM
$i_{T,\infty}$	current of the tip in bulk of SECM
J_i	flux of species i
kWh	kilowatt hour

M	molar concentration
mol	mol
n	number of transferred electrons
nA	nano ampere
pH	negative logarithm of the activity of H^+ in a solution
Q	charge (coulomb)
R	gas constant $(8.314\ \text{kg m}^2\ \text{s}^{-2}\ \text{K}^{-1}\ \text{mol}^{-1})$
RG	diameter of the microelectrode sheath divided by the diameter of electroactive area
s	second
T	temperature
t_i	transference number of species i
V(x)	velocity of movement of species
V	voltage (volt)
WE	working electrode
Ω	ohm
φ	potential

RÉSUMÉ

La conception des batteries lithium-ion est l'une des réalisations industrielles les plus importantes du siècle en raison des caractéristiques uniques de ces batteries rechargeables. Par exemple, elles offrent une densité d'énergie élevée et une efficacité coulombienne élevée. En plus, elles ont un taux faible d'autodécharge, un effet de mémoire très limité. Grâce à ces avantages, elles peuvent être utilisées dans des nombreux appareils électroniques tels que les ordinateurs portables, les téléphones portables, les appareils photos et les équipements médicaux. L'une des applications les plus importantes de ces batteries est l'alimentation des véhicules électriques. Cela signifie qu'ils jouent un rôle important dans la résolution du problème de la pollution, qui est un grand défi mondial de notre temps. Bien que ces batteries soient utilisées en tant de sources de courant depuis plus de 30 ans, en vue leurs importance industrielles et économiques, incluant leurs application dans des véhicules électriques, leurs différentes caractéristiques ont toujours été étudiées.

Selon la littérature, un grand nombre des recherches scientifiques vise à étudier des matériaux d'électrodes pour augmenter la performance de batteries. Par exemple, l'utilisation de manganèse dans les matériaux d'électrode positive a été augmenté grâce à leur capacité de débit élevé, leur coût et leur toxicité bas par rapport au matériau cathodique en oxyde de cobalt, par ex. $LiCoO_2$. Cependant, la stabilité des matériaux cathodiques de type spinelle, par ex. le *spinelle*-$Li_xMn_2O_4$ doit être amélioré. L'inconvénient principal de l'utilisation de ces matériaux de type spinelle est la lixiviation vers l'électrolyte. Ce processus diminue la performance de la batterie à cause d'une diminution de la capacité pendant les cycles de charge/décharge, ainsi limitant l'utilisation de matériaux spinelle au manganèse en tant que cathode des batteries au lithium. Alors, tous les travails de recherche qui visent à atténuer ce problème sont extrêmement important.

La discussion ci-dessus est la motivation principale d'évaluation d'une méthode pour étudier Mn^{2+} dissolution à l'échelle microscopique. La microscopie électrochimique à balayage (SECM) a été appliquée parce qu'elle est capable de détecter le flux d'espèces localement à l'interface solide/liquide avec une haute résolution. Dans ce but, le chapitre 2 a été consacré à la conception d'une microsonde pour détecter des ions Mn^{2+} afin d'étudier les matériaux cathodiques Mn-spinelle. Cette microsonde fabriquée a monté une limite de détection basse (14 µM). Comme il existe très peu de rapports sur

ce sujet, le développement de cette sonde est pratique pour les études futures de LIBs. En plus, l'instrumentation et les différents modes du SECM qui sont utilisés comme technique dans cette thèse a été élaboré dans le premier chapitre.

La détection quantitative des ions Li^+ dans les matériaux de batterie est détaillée dans les chapitres 3 et 4. Transport d'ions Li^+ a un rôle fondamental dans les cycles de charge/décharge de la batterie. L'étude de ce transport est importante car elle démontre les caractéristiques de transport de masse à l'interface solide/solution. Ainsi, l'objectif principal du chapitre 3 est de développer une technique pour détecter la quantité d'ions Li^+ dans la solution d'électrolyte. L'application de cette technique a été élaborée en détail dans le chapitre 4. Dans ce même chapitre, la résolution spatiale de la technique est évaluée en utilisant de courant d'ion de Li par micro-trou. La conclusion de cette recherche a été présentée dans le chapitre 5 ainsi que les méthodes expérimentales pour les études futures.

L'objectif principal d'étude présente est de développer une technique analytique pour quantifier les cations qui sont libérés de l'électrode, afin d'améliorer les performances de la batterie et d'atténuer les effets négatifs des ions manganèse qui nuisent à l'efficacité de la batterie.

Mots clés : SECM, La batterie lithium-ion, Matériaux cathodiques de type *spinelle* au manganèse, ASV, SWV, Détection quantitative des ions dans les composants de la batterie.

ABSTRACT

The development of lithium ion batteries is one of the most important industrial achievements of the last 100 years due to the unique features of these rechargeable batteries. For instance, they offer high energy density and high coulombic efficiency. In addition, they have a low self-discharge rate, and no memory effect *etc*. Therefore, they can be used in the body of many electronic devices such as laptops, cell phones, cameras, and medical equipment. One of the most important recent applications of these batteries is to power electric vehicles. Although these batteries have been used as power supplies for more than 30 years, due to important industrial and economic influence, including the electric vehicle market, their various features continue to be a target of study.

According to the literature, a large number of scientific studies are devoted to the study of electrode materials to increase battery performance. For example, the use of manganese in positive electrode materials has been targeted for their high rate capability, lower cost, and toxicity in comparison to cobalt oxide cathode material e.g. $LiCoO_2$. However, the stability of the *spinel*-type cathode materials e.g. *spinel*-$Li_xMn_2O_4$ should be enhanced. The main disadvantage of using these spinel-type materials is the leaching to the electrolyte. This process is reflected in the performance of the battery as the capacity fades during battery charge/discharge cycles. In turn, the practical use of manganese materials as the cathode of lithium batteries is limited, so research work to mitigate this problem is extensively important.

The above discussion is the main motivation behind developing a method for studying Mn^{2+} dissolution on the microscale. Scanning Electrochemical Microscopy (SECM) is targeted due to its ability to local detection of the flux of species at the interface of solid/liquid with high resolution. As a result, the chapter 2 is devoted to design of a microprobe for Mn^{2+} ions detection to study Mn-*spinel* cathode materials. The microprobe demonstrated low limit of detection (14 μM). Since there are very few reports on this topic, developing this probe is useful for future studies of LIBs. Moreover, the instrumentation and the different modes of SECM that is utilized in this dissertation are elaborated at the first chapter.

In addition, the quantitative detection of Li^+ in battery materials is detailed in chapters 3 and 4. Li^+ transportation has a fundamental role in charge/discharge cycles of the

battery. The study of this transportation is important because it reveals the mass transport features at the interface of solid/solution. So, the main goal of chapter 3 is to develop a Li^+ measurement technique in electrolyte solution. In chapter 4 the application of this technique is elaborated, moreover, in this chapter, the spatial resolution of the technique is evaluated using the current of Li^+ from a micropinhole. Finally, the conclusion of this research and also the experimental works for future studies are presented in chapter 5.

The main purpose of the present study is to develop an analytical technique to quantify the cations, which release from the electrode, to enhance the battery performance and mitigate the negative effects of manganese ions that hinder the battery efficiency.

Keywords: SECM, Lithium ion battery, Manganese *spinel* type cathode materials, ASV, SWV, Quantitative ion detection in battery components

INTRODUCTION

0.1 Development of Lithium Ion Battery

0.1.1 History of Lithium Ion Battery

Nobody could imagine that the shiny and combustible metal that was identified in the 1817 by Johan August Arfwedson would change the world of energy storage devices and make a multitude of headlines long afterwards (Weeks & Larson, 1937). In 1818 Jakob Berzelius reported the presence of a new element in the mineral ore of Petalite ($LiAlSi_4O_{10}$) and named it Lithion. From the first days of detection, the most challenging part was its isolation because of its high reactivity. Eventually in 1821 lithium metal was obtained from the voltaic pile of lithium oxide (Winter et al., 2018). This was the first combination of lithium and electrochemistry which would almost two centuries later be the subject of Nobel Prize of chemistry. It took a long time to recognize the power of lithium in electrochemistry and it mainly coincided with the time that scientists noticed the particular properties for application in lithium batteries (Tarascon, J.-M., 2010). For instance, the lowest reduction potential in the periodic table belongs to lithium. Consequently, lithium-ion insertion anodes can have the lowest electrochemical potential, and which allows for the highest battery potential of all possible elemental insertion ions. Moreover, Li containing batteries provide high gravimetric (3860 mAh g^{-1}) and volumetric (2061 Ah L^{-1}) capacity because of the light-weight and small ionic radius of lithium ions (Nitta et al., 2015). There are some multivalent cations like Al^{3+} or Be^{2+} with higher volumetric capacity, but the additional charge has negative effect on their mobility in the solution environment, a major

obstacle for designing an Al or Be battery (Winter et al., 2018). Combined, Li has significant advantages for use in the body of batteries in comparison to other elements.

After the Second World War, use of oil in the form of gasoline or similar products increased significantly in the United States which led to problems of shortage in domestic resources and dependency on import of oil from foreign countries, especially from the Middle East (Ryssdal, 2016). Fear of the oil deficit to heat homes or run various sectors of the economy led to an "energy crisis" that directly promoted public demand for new alternative sources of clean, available, and storable energy, such as electricity. Subsequently, batteries became especially important as devices for storing electrical energy. The main goal was to restrict the use of fossil fuel. The conventional batteries like lead-acid or nickel-cadmium could not offer satisfying energy densities and so searching for more efficient energy storage devices with better performance was a necessity.

In the same years Professor Whittingham from the Exxon Company prepared a lithium-ion battery using the metallic lithium as the anode. The titanium disulfide that was used as the cathode of this battery had layered structure and was an excellent host for Li^+ from the anode (Whittingham, 1976).

According to Whitingham, storage of Li^+ in cathode layers causes only slight changes in the crystal structure of the host, so the Li^+ exchange process is very reversible. He named it “intercalation” (Whittingham & Gamble Jr, 1975). This battery was commercialized by Exxon Company in the late 1970s. However its usage was halted very soon due to various safety issues (Whittingham, 2004). A big part of the problem was the formation of “dendrite” defects at the anode of metallic lithium. During charging dendrite formation is caused by an uneven nucleation of Li on the surface of the anode that leads to growing of a non-uniform surface of metal. Such dendrites or uneven pointy crystals on the surface of lithium can cause short circuits between the

interior parts of the battery and raise the risk of explosion (Figure 0.1). Moreover, although the presence of TiS_2 in the body of the battery has some important advantages like high capacity of intercalation, the release of highly flammable H_2S makes them very unsafe (Li et al., 2018).

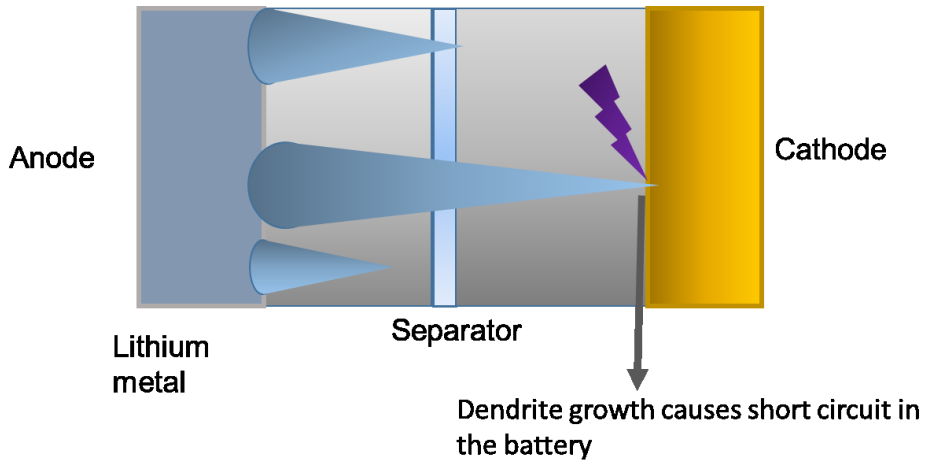

Figure 0.1 Scheme of dendrite formation at the surface of the anode of the battery.

Given these problems and the relatively low voltage (2V vs. Li/Li^+), a modification in the structure of the battery was needed. In the early 1980s based on Goodenough's efforts, a new battery was designed. He and his co-workers proposed using transition metal oxides due to their stability during battery operation and ability to provide higher energy. The cathode of the battery, TiS_2, was replaced with the layered cobalt oxide. This new battery can store even more Li^+ in comparison to TiS_2 and with this feature the capacity of the cells is doubled (Mizushima et al., 1980, 1981). The proposed cathode material is still used in some type of batteries.

After these innovations on energy storage field on mid-1980s, many research groups were eagerly working on different components for promoting the efficiency of Li-ion

batteries (LIBs) including a group of researchers from the Asahi petroleum. Specifically, Prof. Yoshino was inspired from reports on the lithiation/dilithiation of layers of graphite and decided to use a carbonaceous host as the anode material (Yoshino, 2012). This battery consisted of a $LiCoO_2$ cathode and a petroleum coke anode (Blomgren, 2016). In the new battery, some key features such as safety and longer life had been upgraded compared to previous batteries (Goodenough & Mizuchima, 1981; Yazami & Touzain, 1983). Figure 0.2 is a simple scheme of lithium-ion battery with the different types of anode and cathode materials which were introduced in the previous paragraphs.

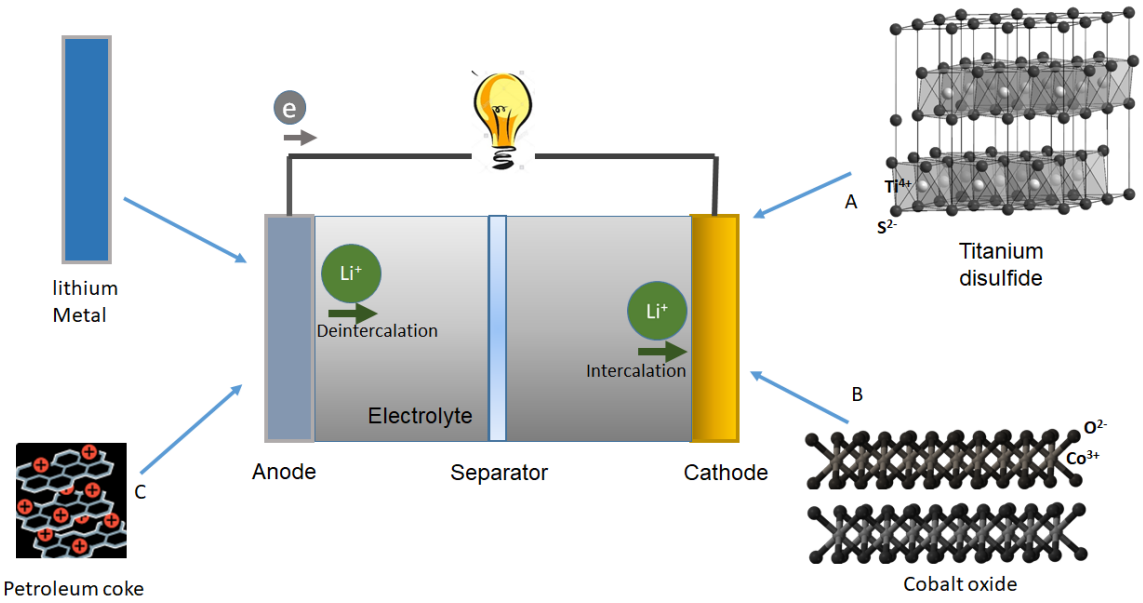

Figure 0.2 Schematic of the lithium based battery. Whittingham's battery which consisted of the lithium metal as anode and titanium disulfide as cathode material (A). Goodenogh's battery with lithium metal as anode and layered cobalt oxide as cathode material (B). Yoshino's battery with Petroleum coke as anode and cobalt oxide as cathode material (C).

As a result of this effort and after almost 20 years of attempt by different researchers, finally the first generation of commercial LIBs were introduced to the world by Sony

Corporation in 1991 (Dunn et al., 2011; Zaghib et al., 2003). A consequence of this innovation was reduction in the size and weight of the batteries in electrical products like hand-held cameras.

0.1.2 Lithium Ion Battery in Road Transport

Problems of using fossil fuels and oil on environmental issues like pollution and climate change are flagging the need of using a green source of energy such as wind or solar power. However, the problem is that the sun is shining for a limited number of hours of the day and the wind is not continuously blowing. Thus in this situation, there is an absolute requirement to have a proper storage system for the renewable energy resources (Scrosati, 2011).

The idea of utilizing batteries in vehicles comes from this requirement too. Batteries are mainly used in two different groups of vehicles, hybrid electric vehicles (HEV) and electric vehicles (EV). HEVs have an internal combustion engine and an electric motor. In HEVs, the battery is not plugged in for charging, it uses regenerating breaking and combustion engine instead. Because of this extra provided power by the electric component, it is possible to have a smaller engine and less fuel consumption in these vehicles (Energy, 2017; Zubi et al., 2018)

In comparison, in an EV, there is no combustion engine and electricity is fully powering the vehicle. Therefore, the capacity of the battery used in EVs should be high enough for the vehicle's engine operation which starts roughly from 18 kWh (Zubi et al., 2018). Thus, normally an EV has a much larger battery in comparison to the HEV.

The plug-in hybrid electric vehicles (PHEV) is a technology that combines the HEV and EV technology, and uses an intermediate battery size that can be recharged from

the grid and can provide adequate electric energy for a short trip (between 10- 40 miles). For longer distances the PHEV vehicles again use fuel energy and electric together for reducing the level of fuel consumption (Chen, A. & Shah, 2013).

0.1.3 Importance of the Lithium Ion Battery in Québec

For providing the battery manufacturing raw materials, Québec is an ideal place. Lots of mineral resources for electrode preparation such as graphite, iron, nickel, cobalt and phosphate are located in Québec region. The province also has a significant resource lithium resources. However, the quality of some of these products should be increased to be sufficient for use in batteries. A number of factors are favoring industrial development in Québec in the field of LIBs (Houde, 2019):

1. Globally, the usage of EVs in 2030 is estimated to be 26 times more than today. This means there will be high demand of raw battery materials for battery manufacturing in the province.

2. Québec is located in proximity to Ontario and United-States automobile manufacturing centers. It also has good access to expert centers of developing and assembling electric truck, snowmobiles and buses. Moreover, the operation costs for battery manufacturing in Québec is relatively low for North America.

3. Numerous universities and research centers in Québec are working on the LIBs and sub technologies. Researchers are developing energy-related courses and projects in Hydro Québec's Center of excellent in transportation electrification and energy storage, National Research Council of Canada, National Center of

Electrochemistry in Environmental Technologies and Institute of innovative vehicle (IVI) are very few examples which are located in Québec (Houde, 2019).

0.2 Basic Operation of LIBs

0.2.1 Fundamental of Battery Operation

A battery consists of negative and positive electrodes that are immersed in electrolyte (Figure 0.3.A). A separator, i.e. a thin porous membrane physically separates the positive and negative electrodes. The presence of separator is necessary for avoiding short-circuits in the battery.

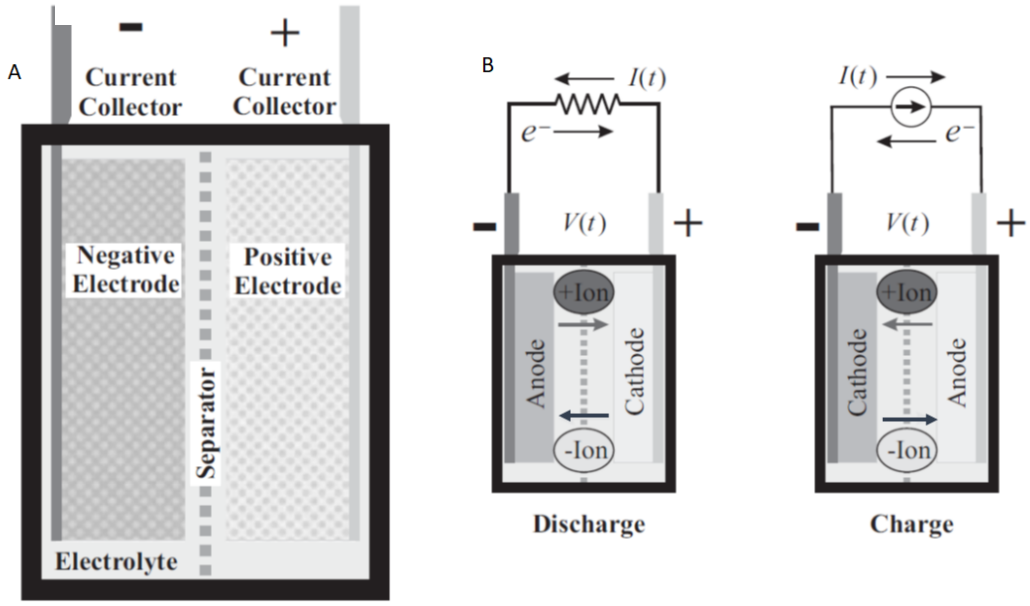

Figure 0.3 The main battery components (A), a battery under charge ,discharge process (B) (Rahn & Wang, 2013)

Figure 0.3.B shows the process of battery charge/discharge. During discharge electrons flow from the anode to the cathode *via* the external circuit. In the electrolyte solution, the positive ions are moving toward cathode and negative ions are moving in reverse direction. Two current collectors work as the electronic connection of the positive and negative electrodes to the external circuit. The most well-known current collectors are Al or Cu. The basis of a battery operation is the exchange of electrons from the redox reactions that are taken place at the electrodes. During charging, an oxidation reaction at the positive electrode causes the liberation of positive ions and electrons. These electrons are "consumed" at the negative electrode for intercalation of positive ions from electrolyte by a reduction reaction. In a lithium-*ion*-battery, both electrode materials are based on Li intercalation/deintercalation. (Aifantis et al., 2010).

The classic Sony battery electrode reactions are

$$Li^+ + e^- + C \rightleftharpoons Li_xC \qquad (0.1)$$

$$LiCoO_2 \rightleftharpoons CoO_2 + e^- + Li^+ \qquad (0.2)$$

Where during charge Li^+ is inserted into vacancies between graphite layers in the anode and reversely in the positive electrode material, $LiCoO_2$, the Li^+-ions release from the structure to the electrolyte. During discharge the process is reversed, positive ions inside the electrolyte move toward the positive electrode and negative ions are moving in the opposite direction as electrons flow through the external circuit (Rahn & Wang, 2013).

Beside important advantages of the LIBs such as their long lifespan, good cyclability with low self-discharge rate and low cost, they offer high energy density. This is due to the high voltage of these batteries (i.e. 4.1 V) and high capacity (Nazri & Pistoia, 2008; Rahn & Wang, 2013).

0.2.2 Lithium Ion Battery Electrode Material

As discussed in the previous section, the energy density of a LIB battery consisting of $LiCoO_2$ cathode and graphite anode has much higher than the energy density than Ni or Pb batteries. However, due to the high demands for LIBs, it is important to enhance the battery characteristics such as price, safety, life span, capacity or effect on the environment. As such, a key research topic is to find an alternative for graphite and $LiCoO_2$ in the body of the battery. (Doughty & Roth, 2012; Williard et al., 2013).

One important consideration in LIBs is their crystal structure modification during Li^+ intercalation/deintercalation and the free energy of the redox reaction of the transition metals in the body of the electrode. In other words, during battery cycling the intercalation of Li^+ affects the host crystal structure and causes instability in the electrode (Yuan et al., 2011). Therefore, electrode materials with various crystal structures have been examined to find the proper candidate, which can tolerate lithium-ion exchange between electrodes.

0.2.2.1 LIB Positive Material

Nowadays usage of $LiCoO_2$ as a cathode material is less common, mostly due to the instability of layered CoO_2 structure caused by conversion of Co^{3+} to Co^{4+} during charging which reduces the life span of the electrode. The practical capacity (140 mAh g^{-1}) is therefore reduced in comparison to the theoretical one (274 mAh g^{-1}). Moreover, Co toxicity and its high cost make it an unfavorable choice (Aifantis & Hackney, 2010).

In comparison, the oxidation reaction of $LiFePO_4$ (LFP), an alternative cathode material, involves interconverting stable Fe^{2+} and Fe^{3+} ions. Having a long lifetime near 10000 cycles and good temperature tolerance (approximately form -20 to 70°C) makes

$LiFePO_4$ an important cathode material. (Deng, 2015). Figure 0.4.C shows the crystal structure of the $LiFePO_4$ with the Li^+ that transport through its channels during battery operation.

In order to propose cathode materials with lower cost and toxicity and higher capacity, many different materials have been studied. Generally, there are four main types of crystal structures for cathode electrode, including *olivine*, *spinel*, *tavorite* and *layered* (Figure 0.4) (Yuan et al., 2011). The *layered* cathode materials such as $LiMO_2$ exhibit good cycling plus long life but the most important problem with them are safety. As previously described, $LiCoO_2$, as the most well-known material in this family, has the lowest thermal stability compared to other electrode materials. Even replacing Ni or Mn with Co in this structure does not completely solve the safety problem and the delithiated form or MO_2 is not thermodynamically stable. In fact, these compounds have a tendency to transition from the *layered* to the *spinel* structure. Moreover, it is difficult to synthesize some of these layered oxides like $LiNiO_2$.

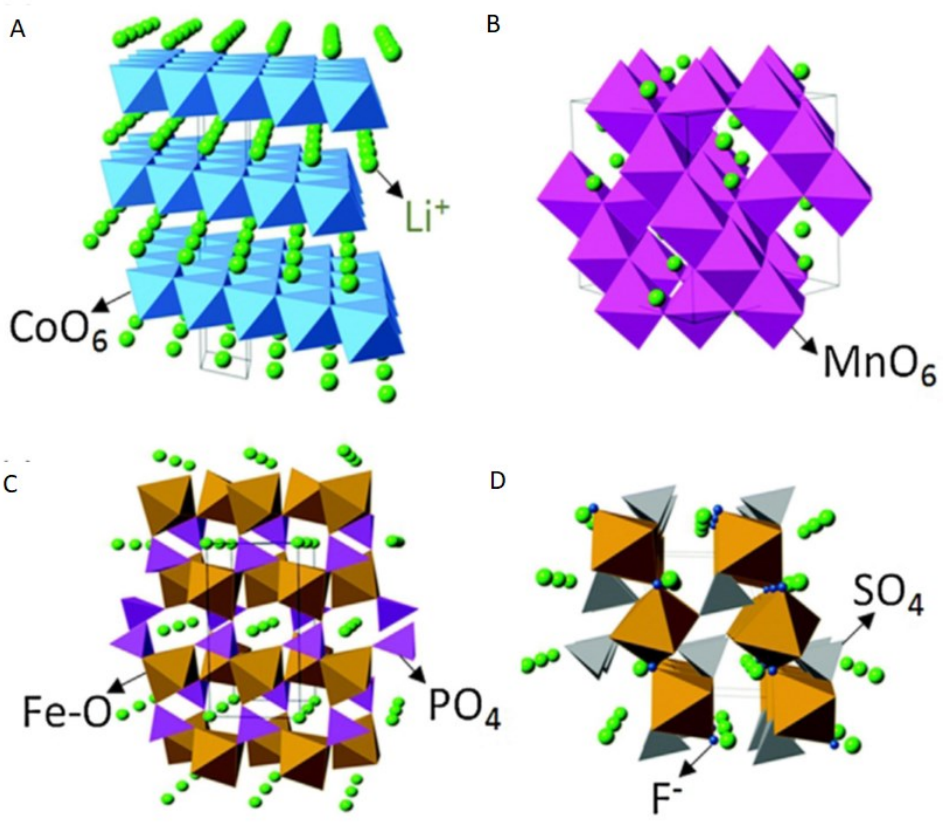

Figure 0.4 Crystal structure of battery cathode material $LiCoO_2$ (*layer* cathode material) (A), $LiMn_2O_4$ (*spinel* type) (B), $LiFePO_4$ (*olivine* type) (C), $LiFeSO_4F$ (*tavorite* type) (D).(Nitta et al., 2015)

In order to reduce the problems of $LiCoO_2$, coating with metal oxides such as TiO_2, Al_2O_3, ZrO_2 has been proposed. The chemical and mechanical stability of these coated metal oxide layers prevent the reaction of $LiCoO_2$ with electrolyte and increase stability, reduce structural changes and improve the performance even after deep cycling (Cho et al., 2001; De Picciotto et al., 1984; Scott et al., 2011).

The LiM_2O_4 crystallizes in the *spinel* structure where M can be V, Ti or Mn. The last one is the most well-known *spinel* type cathode material that offers faster charge/discharge cycling because of high lithium-ion conductivity in the structure in

comparison to $LiCoO_2$. (Daniel et al., 2014). Choosing $LiMn_2O_4$ as cathode material in comparison to the $LiCoO_2$ has several other advantages as will be detailed in the section of manganese containing cathode materials (0.3).

When examining the advantages of the *spinel* structure, it is important to note that due to the difficulties of synthesis, few spinel type materials (with V, Mn and Ti) are synthesized for use as cathode materials. Generally when synthesizing *spinels*, it is hard to stabilize the high oxidation state of M^{3+}/M^{4+} by normal high temperature methods (Manthiram, 2020).

According to the previous part $LiFePO_4$ as a representative of the *olivine* structure offers some unique features that make it desirable for use in the body of LIBs. In the *olivine* structure, the strong bonding between oxygen and phosphorous reduce the risk of oxygen release that can fuel a thermal runaway reaction. This is the main reason of thermal stability of *olivine* structures (Yuan et al., 2011). Conventional polyanions in $(XO_4)^{3-}$ are usually one of the elements of Si, S, P, or Mo and the presence of this large anion in the structure makes it easier for lithium ions to pass through the open three-dimensional framework. (Nanjundaswamy et al., 1996). Besides having high-power capability, the other members of this category, which contain Ni or Co, provide higher voltage (around 5 V vs. Li/Li^+) (Doughty & Roth, 2012; Padhi et al., 1997).

In continuation of this research, the general structure of $AM(TO_4)X$ was proposed where A is the member of the first or second group of the periodic table, M is a transition metal, X is O, F or OH and T is an element of P-block. Collectively, these materials crystallize in the *tavorite* structure, which has some exceptional properties as an electrode material. These include high thermal stability, capacity, and high rate for lithium intercalation (Mueller et al., 2011; Reddy et al., 2009). Several *tavorite* compounds such as $LiAl(PO_4)F$ or $CaTiO(SiO_4)$ are known and some of them like $LiFe(SO_4)(OH)$, $LiVO(PO_4)$ and $LiV(PO_4)F$ have been evaluated as cathode materials.

For instance, $LiV(PO_4)F$ shows the voltage of about 4.2 V vs. Li/Li^+, and capacity of 115 mAh g^{-1} while $LiVO(PO_4)$ offers the capacity of 126 mAh g^{-1} at 3.8 V vs. Li/Li^+ (Barker et al., 2003; Kerr et al., 2000). Research is ongoing on the chemical and electrochemical aspects of these categories of material.

0.2.2.2 LIB Negative Material

Graphite is one of the most important electrode materials in commercial batteries. Normally the carbon-based materials are classified in two main categories: Graphitic and non-graphitic. Graphitic carbons have nearly perfect crystalline planner layers, but in the structure of non-graphitic type, there are nooks caused by cross-links causing amorphous areas of the hexagonal carbon network. Non-graphitic anode materials show higher capacity than the graphitic type because there are more places to absorb Li^+, but capacity fading after first cycle is very serious in these types of materials.

Li-metal was utilized in the first batteries (Murphy & Christian, 1979) as reviewed in the previous sections. One of the most important challenges of Li-metal is the formation of dendrites inside the battery. These can cause short circuits that can cause fires and eventually kills the battery. Moreover, Li containing anode materials have poor life cycle as such carbon-based anode materials and especially graphite were introduced as an alternative. (Nitta et al., 2015).

The *layered* structure of graphite (Figure 0.5) is a good host material for Li^+ which can intercalate easily and fast, with good reversibility without structural changes with intercalation during battery operation (Megahed & Scrosati, 1994). Generally, parameters such as crystallinity and morphology of the structure, in addition the texture and thickness of the fabricated electrode have a critical role on the efficiency of the anode for lithium-ion insertion. For instance, graphite with perfect layer structure can

absorb twice as much Li in comparison of petroleum coke or turbostratic carbons. These materials are forming Li_xC_6 in which $0 < X < 1$ for graphite and $0 < X < 0.5$ for the petroleum coke (Fong et al., 1990; Shu et al., 1993).

Graphite could be found in by-products of petroleum. Figure 0.5 shows the layer structure of graphite. Studies on various types of carbon-based materials and carbon nanotubes (CNT) shows excellent Li^+ hosting ability. Recent efforts are mainly focused on choosing a composition of these compounds with graphite for having the maximum capacity. (Yuan et al., 2011).

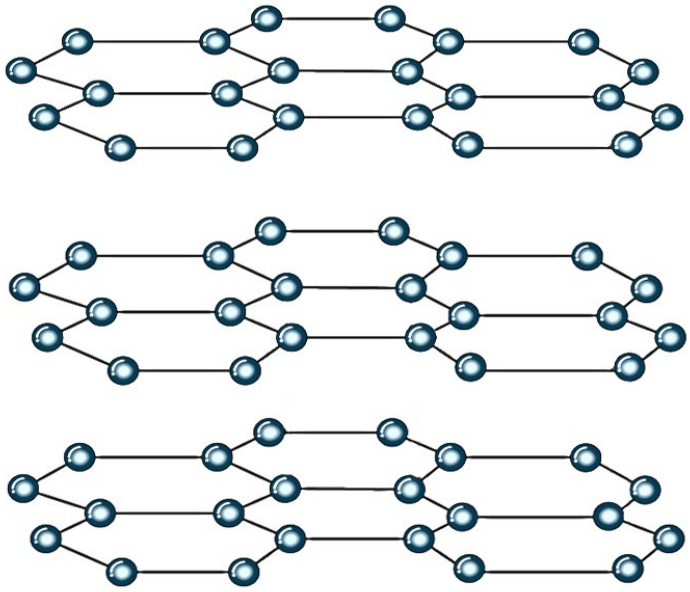

Figure 0.5 Graphite layered structure

During the time of carbonaceous material discovery, some efforts were started on intermetallic anode materials. For instance, some metals such as Si, Sn, Bi, Pb or In could be used as host without having the problem of dendrite formation. Although the preliminary results were promising, the large volume changes during Li^+ ion insertion/ release became an important issue (Rao et al., 1977; Wang et al., 1986). It is important

to mention that the graphite has mechanical stability during expansion but in most of the studied metals, deep cracks are formed after intercalation/deintercalation of Li^+. The result is a massive battery capacity loss after the first cycle. This issue has prevented commercializing most metals as anode material (Aifantis, 2010).

Of the materials studied, Si and Sn were shown to have a good ability for hosting Li^+. They can accept four times more Li^+ than graphite but their large volume expansion is still an issue. One innovative approach to solve this problem is using the composites that contain binary materials such as Si/C. During reaction, Si lithiates to make $Li_{4.4}Si$ which boosts the capacity, while C is responsible for absorbing the stress of the ensuing volume changes. The combination of Si and C or SnO_2 and C have meet with significant success (Dimov et al., 2007; Winter & Besenhard, 1999). Another anode composite example is iron oxide, an abundant and environment-friendly material, combined with carbon, which can deliver high capacity and controlled volume change (Zhang et al., 2014), (Poizot et al., 2000). TiO_2 is the other important example of metal oxides. Its capacity is lower than the one for graphite but the lithium ion insertion is happening at 1.5 V vs. Li/Li^+ and dendrite formation is prevented. (Nitta et al., 2015). Therefore, these materials can be considered as an alternative of graphite for anode of the LIBs, because of their safety. Among other Ti compounds, TiO_2 and $Li_4Ti_5O_{12}$ seem to have been the subject of battery materials more than others due to their diverse crystal structures and structural stability. However, despite having excellent features for being as anode material, TiO_2 does not have high electrical conductivity, in addition, the mobility of Li^+ in this structure is low (Chen, Z. et al., 2013; Mei et al., 2016; Zhu et al., 2012).

Studies are still ongoing with various research groups to find new anode materials, but scientists believe that silicon nanomaterials and composites are a good choice for anode material and could even replace carbon-based anodes in the near future. However, their

high cost is a negative factor in order for them to be recognized as a popular battery material (Deng, 2015).

0.2.3 Lithium-Ion Battery Electrolyte and SEI Formation

During battery operation, Li^+ are exchanged between anode and cathode continuously inside the battery. The typical liquid electrolyte consists of a salt of Li^+ such as lithium-hexafluorophosphate ($LiPF_6$) or lithium-perchlorate ($LiClO_4$) dissolved in an organic solvent (Zubi et al., 2018). Initially the solvent was propylene carbonate–diethyl carbonate (PC-DEC), however, nowadays a solution of lithium salt (especially $LiPF_6$) in the ethylene carbonate (EC), dimethylcarbonate (DMC), (EC-DMC) and a mixture of EC plus linear carbonates are the commercial electrolytes for LIBs. EC-DMC shows high ionic conductivity (10 mS/cm) and good stability (up to 5.1 V vs. Li/Li^+) (Flamme et al., 2017; Gu, Y. et al., 2021; Scrosati, 2000).

Although these liquid organic electrolytes are the most popular electrolytes, the organic solvents are flammable and the risk of thermal runaway or fire is high. As a result, alternative materials are eagerly pursued. Generally, in addition to liquid electrolytes the different types of electrolytes can be categorized as follows (Yuan et al., 2011):

a. Ionic Liquids: Non-flammability and high thermal stability are the key features of these electrolytes which reduces the safety issues. In general, lithium salts have high solubility in these kinds of solvents, another positive factor. However, the high viscosity of ionic liquids causes Li^+ to move more slowly, which is one of their disadvantages (Diaw et al., 2005; Hu et al., 2004).

b. Solid Polymer Electrolytes (SPE): Polymer electrolytes composed of Li salts dispersed in a polymer matrix are acting as both electrolyte and separator in

batteries. Polyethylene oxide (PEO), polycarbonate, and some other compounds based on it are examples of common solid polymeric materials used in the body of batteries (Bekaert et al., 2017; Scrosati, 2000).

One important feature of using SPEs is eliminating the Li dendrite growth. Combined with their low flammability this increase the safety. (Yao et al., 2019). The high flexibility of the polymer structure enhances the life span of the electrodes by preventing crack formation in the electrode structure (Meyer, 1998). However, the serious problem of SPEs is their low conductivity, for instance for the PEO-based polymer electrolytes the ionic conductivity is less than 10^{-5} S cm^{-1}, therefore, it is mandatory to work at 60°C or higher to reach a higher conductivity (10^{-3} S cm^{-1}). The minimum temperature for transit from crystalline structure to amorphous in PEO-based polymer electrolytes is 60°C (Varzi et al., 2016). Addition of Li soluble salts such as LiTFSI and using the nanostructures in these types of electrolytes help to improve conductivity. (Bekaert et al., 2017; Scrosati, 2000)

c. Inorganic Solid Electrolytes (ISE): The high ion-conductive inorganic solid electrolytes (ISEs) are a good choice for the electrolyte since they have silver or sodium ions in the structure which can provide high ionic conductivity. With a wide electrochemical window and a safe and non-flammable nature, they have an important priority over organic liquid electrolytes. Nevertheless, in most cases, the volume change at the electrode/electrolyte interface in this type of material is relatively large and this problem must be solved before commercialization. Thio-LISICON (lithium superionic conductor) with the formula ($Li_{3.25}Ge_{0.25}P_{0.75}S_4$) is an example of these materials, which has the conductivity of 2.2×10^{-3} S cm^{-1}. It is one of the most conductive solid materials for Li^+ (Bachman et al., 2016; Inada et al., 2009).

d. Hybrid Electrolytes: There have been some attempts to use a mixture of two or three types of these electrolytes together. It seems possible to take advantage of

different groups at the same time. However, more studies on these hybrid systems need to be pursued and information is currently limited (Han et al., 2020).

0.2.3.1 SEI Layer Formation

The formation of Solid Electrolyte Interface (SEI) layer is a common phenomenon in all of LIBs. The discussion about the role of SEI is very complicated because although it is one of the most important reasons of losing capacity in batteries, without this layer, batteries operation is not possible.

In simple terms, when a battery experiences its first cycle of charging, at potentials below the electrochemical stability window of the electrolyte, a reduction process of electrolyte occurs at the negative electrode. As a result, a passive layer of degraded electrolyte forms at the top of the anode. Basically, this layer is composed of both organic and inorganic degradation products (Tasaki et al., 2009). The formation of SEI layer depends on multiple parameters. It is interesting to note that different research groups have very different reports on the composition of the SEI layer (Heiskanen et al., 2019). Importantly, the Ti type anode materials which was elaborated in 0.2.2, has high operational voltage and does not experience the formation of SEI layer. Therefore, it has a long life span (Zhu et al., 2012).

The SEI passive layer protects electrode against continued solvent decomposition at very negative voltages, as well as solvent intercalation in the anode material and subsequent deep exfoliation (Besenhard et al., 1995). According to studies, solutions containing cyclic alkali carbonates such as EC form more effective passive layer. This is one of their advantages for use in batteries as electrolytes (Aurbach et al., 1996).

Importantly, if formation of the SEI layer continues in each cycle of battery operation, and this layer becomes increasingly thicker, it will completely halt the battery. The main reason that the battery can continue to work is that Li^+ can easily pass through the SEI layer. Thus, this layer makes the battery electrode more stable without stopping the battery cyclic operation. As we saw above, SEI formation is vital for battery operation cyclability, and the electrode stability (Verma et al., 2010).

0.2.4 Effects of Concentration Gradients on the Performance of the Battery

0.2.4.1 Mass Transfer in an Electrochemical Cell

The movement of the species in the electrochemical cell arises either from the difference in the chemical and/or electrical potential between two electrodes inside the solution. The modes of mass transport are migration, diffusion and convection. Migration is due to charged body movement under the influence of an electric field. The diffusion of species occurs under the influence of concentration gradients and convection is mainly related to a hydrodynamic movement, i.e. a flow of the species due to the force of a stirrer or the gradient of density in solution *etc*. (Bard & Faulkner, 1983).

The equation of Nernst-Plank shows the mass transfer of these three parts:

$$J_i(\mathrm{x}) = -D_i \frac{\partial C_i(x)}{\partial x} - \frac{z_i F}{RT} D_i C_i \frac{\partial \varphi(x)}{\partial x} + C_i V(x) \qquad (0.3)$$

In which the three terms from left to right are representative the diffusion, migration and convection, x is the position and J_i the is the flux of species i (mol $s^{-1}cm^{-2}$). The terms of $\frac{\partial C_i\,(x)}{\partial x}$, $\frac{\partial \varphi(x)}{\partial x}$ are the concentration and potential gradient in that order. C_i and z are concentration (mol cm^{-3}) and charge while R is the gas constant and T (K) is the temperature. In the equation 0.3, D_i represent the diffusion coefficient which is generally the magnitude of the flux through a surface per unit concentration gradient ($cm^2\ s^{-1}$). The last part of the equation which is related to convection includes $V(x)$ the velocity of movement of the species in the solution (cm s^{-1}).

Depending on the electrochemical experiment design, one or two terms of mass transport can be eliminated from the equation of the flux. Normally by assembling a cell without stirring, the effect of the convection is negligible. To mitigate the effect of migration in mass transfer, adding the proper amount of an inert electrolyte is a good solution and can neutralize the effect of migration in the chemical cell. The concentration of the inert electrolyte should be higher than the concentration of redox material in the solution. Generally, an inert electrolyte or supporting electrolyte contains non-electroactive ions within the experiment potential range. The presence of the support electrolyte in high concentration makes the term of $\frac{\partial \varphi}{\partial x}$ negligible and eliminates the migration part from the equation 0.4. Apart from the effect of support electrolyte on the migration of ions in the solution, the presence of an inert electrolyte reduces the resistance and therefore, the potential of working electrode will be more precisely controllable (Bard & Faulkner, 1983, 2001) .

0.2.4.2 Concentration Gradient Formation in a Lithium Ion Battery

At the beginning of the discharge of an LIB, Li^+ migrates from the negative electrode (i.e. graphite) toward the positive electrode ($LiCoO_2$) due to the difference in potential of two electrodes. In contrast, the potential difference triggers anions to migrate in the opposite direction (Figure 0.6). Initially, since there is a constant initial concentration of electrolyte typically 1M of $LiPF_6$ dissociated into 1M of Li^+ and PF_6^- ions, there can be no diffusion and all charge/mass transport is migration. As soon as current is applied to the cell, the Li^+ ions are transported toward the positive electrode, however, the rate at which Li^+ is transported is insufficient to maintain the cell current.

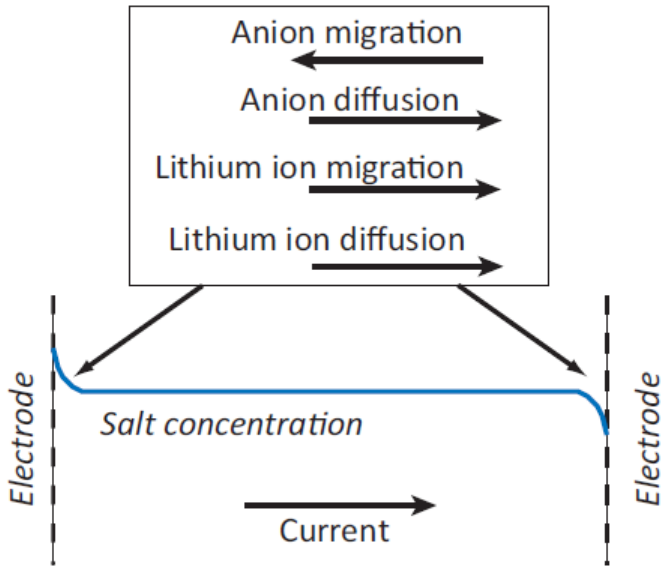

Figure 0.6 Scheme of the mass transport in the electrolyte of LIB (Nyman, 2011)

It is important to consider the movement of both positive ions (Li^+) and negative ions (PF_6^-) as charge carriers because these positive and negative ions do not move at the same velocity in the solution. The fraction of the current carried by Li^+ and PF_6^- ions is defined as their transference number (Bard & Faulkner, 2001). According to the literature, the transference number (or transfer number) of Li^+ (t_{Li^+}) is smaller than the one for PF_6^- anion ($t_{PF_6^-}$) (Nyman, 2011). This insufficient transport of lithium ions combined with the release of the Li^+ from the negative electrode, leads to a rise of the concentration of the Li^+ at the electrolyte phase near the graphite layers. (Nyman, 2011). This mechanism continues along the whole cell toward the positive electrode where the unoccupied sites take up Li^+. Therefore, the insufficient transport of Li^+ by migration causes a significant concentration decrease close to the positive side of the cell. The combination of concentration profiles related to both electrodes shows the formation of a concentration gradient during the application of high cell current density. e.g. Figure 0.7 demonstrates the concentration profile of Li^+ across the cell for two different current density (-30 mA cm^{-2} and -3 mA cm^{-2}). In both cases, the

migration of the species causes the build up of a concentration gradient in the solution, but it takes more time in solutions with less current density. Considering the effect of diffusion, in low current density, the diffusion rate of Li^+ inside the electrode material corresponds to the consumption of Li^+ by the positive electrode, therefore, the chance of formation of high concentration gradients due to the lack of charge carriers is very limited. In this situation (low current density) since the concentration gradient form over a longer time, there is more time to "even it out" by diffusion of species (Chhin et al., 2020).

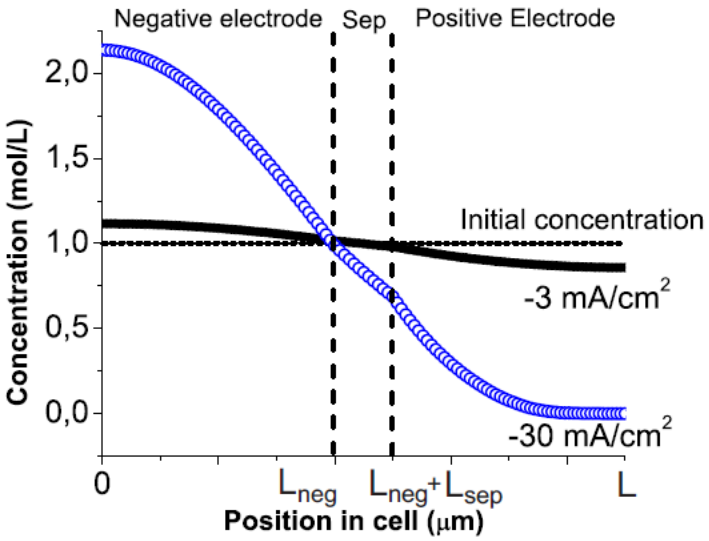

Figure 0.7 Concertation profile of Li^+ in the electrolyte solution across a LIB for high and low cell current densities (-30 mA cm^{-2} and -3 mA cm^{-2}) (Chhin et al., 2020).

In general, transference number is an important factor that determines the performance of the electrolyte in LIBs. It is defined as:

$$t_i = {Z_i F J_i}/{I} \qquad (0.4)$$

Where t_i is the transference number, Z_i is the charges of species i, F is the Faraday constant, J_i is the flux of the ion i relative to the solvent and I is the current density. Using transference number is one way to determine how fast the stored energy in the body of the LIB can be delivered and this is undoubtedly related to the performance of the electrolyte of the battery (Xu, K., 2004; Zhao et al., 2008). Since the transference number of an ion is the fraction of the current carried by that ion species in the solution of an electrolyte, so a transference number close to 1 for a specific ion is ideal for a good contribution of particular ionic species for transporting the charge across the cell solution. In contrast, a small transference number indicates that only a small fraction of the total current is carried by the specific ionic species (Atkins & De Paula, 1998). A low transference number of Li^+ in an electrolyte solution demonstrates that a large fraction of the current is transported by the non reacting counter ions of Li^+ (For instance PF_6^-). Therefore, a high concentration gradient is developed in the solution (Klett et al., 2012; Musil & Vondrák, 2014). In this case, there is a high probability of lithium plating at the anode of the battery as well.

It is important to note that the formation of a concentration gradient is affected by the microstructure of the electrode. The effect of the electrode structure is reflected in the tortuosity of the electrode structure, which is introduced as the ratio of average of actual Li^+ pathway to the straight or shortest possible pathway inside the composite electrode (Kia et al., 2017). This parameter depends on the porosity of the electrode material and the average particle size of the solid electrode material. Because of the tortuosity effect in the electrodes, Li^+ ions are redirected from their straight path, thus all the mass transport properties of Li^+ deviate from their intrinsic properties in free solution. For instance, the diffusion coefficient and conductivity in the system are affected by the tortuosity of the electrode (Chhin et al., 2020; Jiang & Peng, 2016). Eventually, changes in the transport properties have an important impact on the formation of the concentration gradient.

0.2.4.2.1 Concentration Gradient in Battery Active Materials

The transport of the Li^+ ion in the liquid phase directly affects the intercalation/ deintercalation of Li^+ in the solid active materials of electrodes. Obviously, the rate of Li^+ diffusion into the active material, which is followed by a reduction reaction to form Li inside the active material, is very important in the battery capacity.

The number of Li^+ ions that needs to intercalate at the positive electrode material surface is directly related to the current applied to the cell during charging. As such, Li^+ rate of transport during intercalation is different under the application of a high current density (-30 mA cm^{-2}) and a low current density (-3 mA cm^{-2}). With the application of -30 mA cm^{-2}, the Li^+ intercalating into the structure accumulatse only at the surface of the particle, as the rate of diffusion toward the center of the particle is slow in comparison to the rate of the intercalation to the surface. As a result, the concentration of Li at the surface of the particle is very different from the center of the particle. Consequently, a large Li concentration gradient is created in the active material. Besides the accumulation of Li on the surface, the vacancies far from the surface remain unoccupied, therefore, a poor capacity at high cell current is observed under these conditions. Applying low cell current density (-3 mA cm^{-2}) can improve this effect and better match the rate of Li diffusion inside the particle to the concentration of intercalated Li^+ at the surface of the particle. As a result, there will be a more uniform distribution of Li in the active material (Chhin et al., 2020).

0.3 Advantages of Manganese Cathode Material

0.3.1 Features and Advantages

Perhaps the primary motivation for choosing manganese compounds in the body of battery materials is cost. Manganese is a very abundant element with roughly 1/10 price of Co. As a result, the battery companies were very eager to replace Co with Mn to lower costs and enjoy the other benefits, such as environmentally friendliness. One of the attractive characteristics of manganese oxides such as MnO_2 is their stability and ability to keep the O in their structure i.e. Mn (IV) in MnO_2 is a stable compound at room temperature, which makes it very safe compared to Co (IV) and Ni (IV) in CoO_2 or NiO_2. As a result, the risk of fire and explosion in manganese-containing batteries is lower than in Ni or Co batteries. (Fritsch & Navrotsky, 1996; Greenwood & Earnshaw, 2012; Johnson, 2007). $LiMnO_2$ (lithium manganese dioxide) or LMO was proposed as a battery material around thirty years ago, but serious issues with the synthesis of this material such as poor crystallinity and non-stoichiometry have limited their exploration (Armstrong & Bruce, 1996; Gu, M. et al., 2013). In addition, LMO is prone to structural change to *spinel* $LiMn_2O_4$ (also LMO) during delitiation. This Mn type material enjoys many positive features as a battery cathode material (Nitta et al., 2015). Once lithium ions exchange during cycling, they pass through three-dimensional channels rather than two-dimensional ones (Nitta et al., 2015; Thackeray et al., 1992). The theoretical specific capacity of the Mn *spinel* structure is 148 mAh g^{-1}, however, the practical specific capacity is approximately 120 mAh g^{-1}, sufficient for most industrial applications (Chan et al., 2003; Danis, Gateman, et al., 2015). Moreover, the fully charged compound Mn_2O_4 is able to maintain the *spinel* structure, which is not possible in *layered* CoO_2 and NiO_2. As a result, Mn type cathode materials are further removed from the risk of explosion. (Lee et al., 2014).

0.3.2 Mn Disadvantages and Negative Effect on SEI Layer

It is recognized that the *spinel* Mn contained batteries suffer from a severe capacity fading during battery charge/discharge cycling. While the mechanism is not fully understood, two main mechanisms are proposed, both of which are related to the dissolution of Mn^{3+} into the electrolyte. The first mechanism is related to the 3^+ oxidation state of Mn, which is not stable due to the Jahn-Teller effect. As a result, a disproportionation reaction is possible (Lee et al., 2014):

$$2\ Mn^{3+} \rightarrow Mn^{2+} + Mn^{4+} \qquad (0.5)$$

Jahn-Teller distortion is a mechanism of symmetry breaking (mainly in the octahedral complexes) to reduce the energy of a molecule. This effect mainly can be seen in the octahedral molecules that has odd numbers of electrons in their e_g orbitals such as d^4 in high-spin Mn^{3+} (Bunker et al., 1998). Therefore, Mn^{3+} is not stable and form Mn^{2+} and Mn^{4+}. Mn^{4+} remains in the cathode material and will not have an adverse effect on battery performance. In contrast, Mn^{2+} can dissolve in the battery electrolyte and transfer to the anode. The subsequent thickening of the SEI causes a shortening of the operational life and reduce power performance of the LIB (Danis, Gateman, et al., 2015; Wohlfahrt Mehrens et al., 2004).

The second model focuses on the storage of the LIB in the charged state where the chance of the oxidation of the positive electrode at the interface with electrolyte drastically increase due to the catalytic role of electrode material. It seems that this oxidation coincides with the oxidation of carbon black at the surface of the electrode and formation of HF which can exacerbate manganese dissolution and electrolyte degradation (Amatucci et al., 1997; Guyomard & Tarascon, 1995; Tarascon, J. et al., 1995; Thackeray et al., 1984). Importantly, the problem of manganese leaching from the positive electrode material becomes more serious at elevated temperatures. Various

efforts by battery researchers such as Prof. Tarascon and Prof. Gummow with their research teams have increased the cyclability of Mn containing LIBs, and these studies have been able to increase charge/discharge cycling up to 2000 cycles at room temperature (Gummow et al., 1994; Tarascon, J. et al., 1994). Based on the latest results of the research by Tarascon et al., the most accessible way to improve these batteries operation at high temperatures is to reduce the interface interaction of the electrode and electrolyte, in which the species are dissolved to the electrolyte. As the surface area decreases, the chance of self-discharge will be greatly reduced.

There are different approaches to solve the problem of Mn dissolution from *spinel* type cathode materials. For instance, one possible solution is to apply a passive film on the surface of the cathode (Amatucci et al., 1997), or using a doped cathode that stabilizes the *spinel* cathode materials (Jang et al., 1998; Nitta et al., 2015).

0.4 Thesis Outline and Objective

This thesis introduction provides information on the development of LIBs and the impact of the LIB invention on EVs and electronic devices, highlighting the importance of the LIBs as the most promising energy storage technology in recent decades. A section of the introduction describes the LIB components and their function, and explains the main materials for the cathode, anode, and battery electrolyte. Also, the result of some of the efforts to replace and use the new generation of components in LIBs to have better performance were discussed. The remainder of this dissertation is organised as follows

Chapter 1 discusses the SECM technique as a powerful tool with unique features for detecting metal cations in LIBs.

Chapter 2 deals mainly with the problem of manganese dissolution in the LIB electrolyte from *spinel* battery materials and the quantitative detection of dissolved Mn^{2+}. Chapters 3 and 4 are devoted to the introduction of a probe for the local detection of Li^{+} released from the cathode of battery materials. This detection bears very important information about the electrolyte transport characteristics as discussed in the section of transport properties in LIBs (0.2). Chapter 5 summarizes and concludes the dissertation.

The main purpose of this thesis is to provide a methodology for the local detection of metal cations such as Li^{+} or Mn^{2+} ions that are released from the battery electrode material to the electrolyte. This information should pave the way for a more detailed understanding of battery operation and help solve some of the problems that hinder LIB performance.

CHAPITRE I

SCANNING ELECTROCHEMICAL MICROSCOPY

Summary

An important strategy for improving the battery performance is to discover the details of electrochemical reactions during charge/discharge. For example, *in situ* study of the concentration of Li^+ exchanged between two electrodes or detecting the quantity of the Mn^{2+} ions that can be dissolved in the electrolyte solution from the cathode material. Scanning Electrochemical Microscopy (SECM) makes this type of study feasible by providing localized measurements with the required sensitivity. In this chapter we will elaborate the components of the SECM technique, its modes of operation and some of the different probes being used for local detection in this technique.

In order to detect metal cations in LIBs, two well-known voltammetry techniques are used in combination with SECM. These are anodic stripping voltammetry (ASV) and square wave voltammetry (SWV) capable of providing adequate detection limit and sensitivity (in µM range). The last part of the chapter is dedicated to the fabrication of Pt, Pt/Hg and Pt/Ga microelectrodes SECM probes used in the later chapters.

1.1 History and Instrument

In 1989, with the introduction of scanning electrochemical microscopy (SECM) by Bard and Engstrom as a technique that utilizes a working electrode with μm to nm diameters, it became possible to obtain electrochemical data for a specific location of the surface. A device with such a capability was in fact a kind of revolution in electrochemistry (Bard et al., 1989; Engstrom & Pharr, 1989) and a few years later, 1800 peer-reviewed articles and several scientific reports had been published by different researchers (Mirkin & Horrocks, 2000; Polcari et al., 2016). This volume of scientific work reveals the crucial importance of this technique in analytical science. Figure 1.1 shows the simple scheme of SECM. The bipotentiostat of the SECM records the electrochemical responses of the probe (WE1) and sample (WE2), for example an electrochemical condition is imposed at WE2 and measured locally at WE1. The potentiostat must be very sensitive to be able to record low currents (down to fA). The response of the microelectrode provides topographical information convoluted with the electrochemical activity of the substrate. The key feature of this instrument is the 3D position system which includes a piezo motor, that allows the probe to get close to the surface (less than 1μm) and record the current. In addition, the horizontal position of the probe can be changed with great accuracy. As a result, the current can be recorded with high spatial resolution. The last part of the SECM in Figure 1.1 is a data acquisition system that includes software that processes the bulk data from the electrochemical experiment.

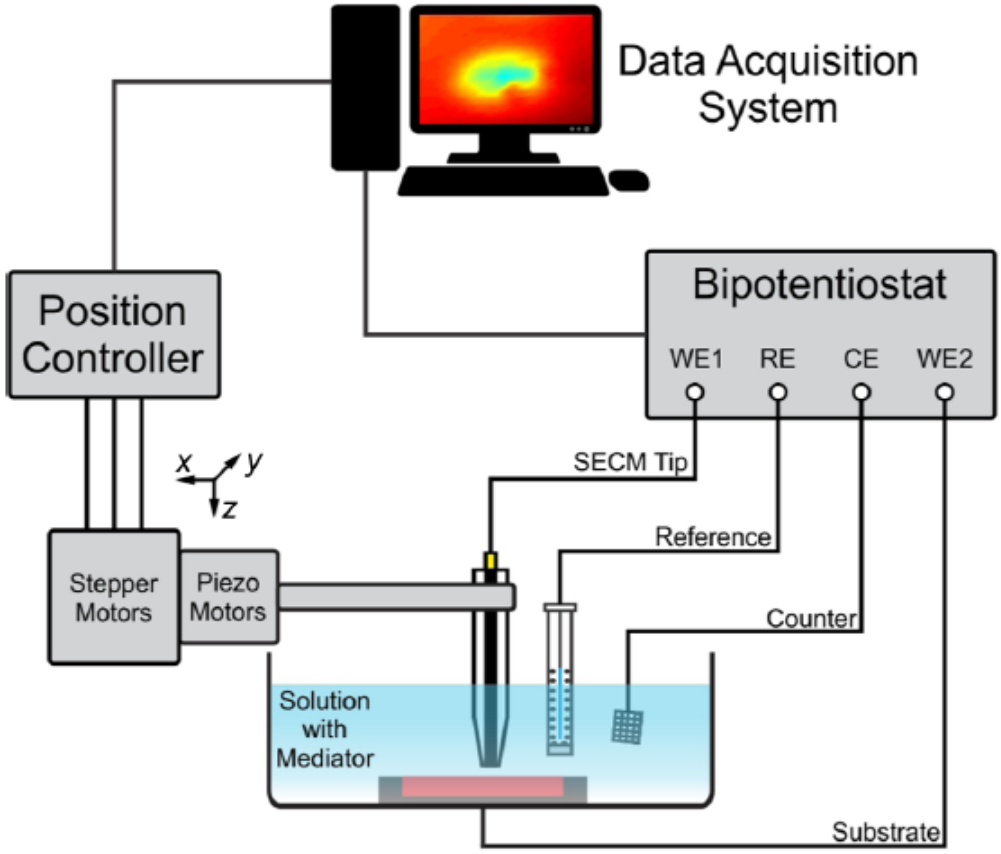

Figure 1.1 A simple scheme of a SECM set up. (Polcari et al., 2016)

1.2 SECM Operational Modes Fundamentals

1.2.1 SECM Positioning System

SECM experiments can be performed at a constant distance or at a constant height. In the experiments with constant distance which is used for evaluation of the topography and the local reactivity, the electrode moves in all three axis directions. Conversely, in the constant height mode, the electrode moves only in the x and y directions keeping

the z position constant. Because of the experimental ease, SECM studies often are carried out in constant height (Morkvėnaitė-Vilkončienė et al., 2017; Nebel et al., 2013). In general, there are several operating modes for SECM, which are used for characterizing the interface of the solid sample and solution (Mirkin & Horrocks, 2000). In the next section, we will detail SECM operational modes.

1.2.2 Operational Modes

Feedback mode: The most commonly used SECM operating mode is the feedback mode, where the current from the oxidation or reduction of a mediator is measured at the tip. Using the SECM set up it is possible to record the current response at the tip as it descends to the substrate. The plot of current vs. tip distance forms the approach curve. There are two main types of approach curves that are commonly used in feedback modes of the SECM: positive and negative. If the substrate is an insulator such as a glass or a piece of inert membrane, the substrate will prevent the diffusion of mediator molecules to the tip of the electrode (Polcari et al., 2016). This trend is shown in the Figure 1.2.A and by decreasing the distance of the tip and substrate, the current reduces (negative feedback approach curve).

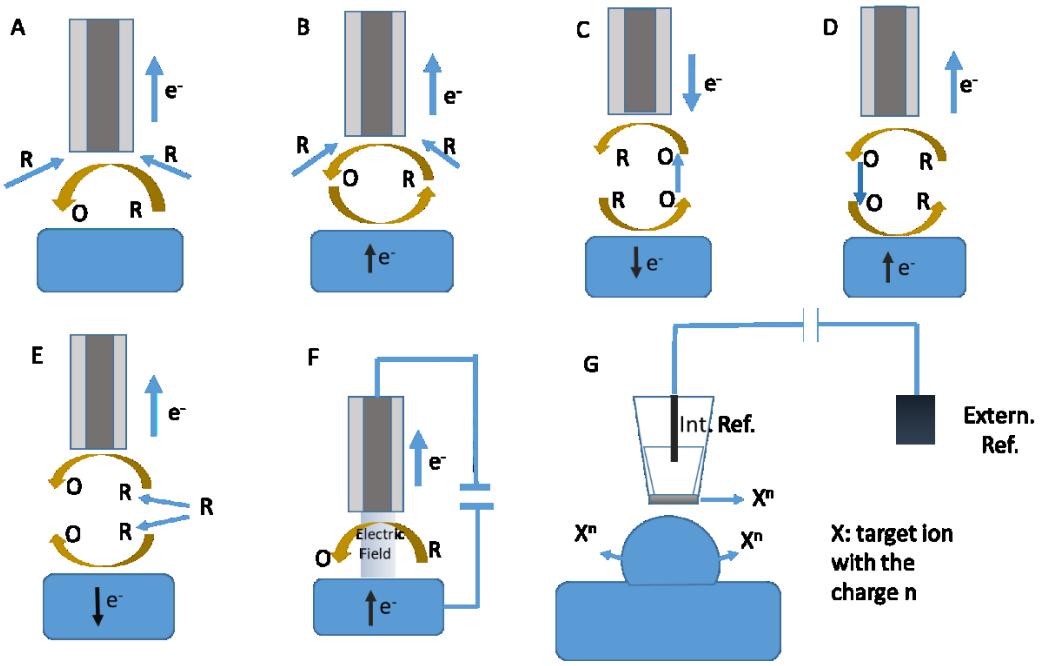

Figure 1.2 Scheme of SECM different modes: negative and positive feedback modes (A,B), SG/TC and TG/SC mode (C,D), RC mode (E), Direct mode (F) and potentiometric mode (G). Blue arrows indicate electron and mass transport, yellow arrows show the redox conversion of the electroactive species.

The surface of the substrate to which the tip approaches may also be conductive. In this case, although the diffusion of the mediator species to the tip is hindered due to the physical presence of the substrate, the conductive surface of the substrate regenerates the mediator, which leads to an increase in the flux of species and subsequently the current of the tip (positive feedback in Figure 1.2.B). In positive feedback mode, the charge neutrality of the surface after regeneration of the species is provided by the redox reaction of the mediators present in the solution. In other words, the regeneration of the mediator at the surface causes the charge neutrality of the surface to change, while other mediator molecules that have contact with the surface compensate for this charge with a redox reaction.

Figure 1.3 demonstrates the negative and positive approach curves where I is the normalized current of the tip (i.e. $\frac{i_T}{i_{T,\infty}}$) in which i_T is the current of tip at the distance of L and $i_{T,\infty}$is the tip current at the infinite distance from the sample. The normalized distance in the approach curve, $L=\frac{d}{a}$ (d is the tip-surface distance and a is the radius of the electrode). So, in the negative approach curve the current of tip decreases below unity when approaching the substrate surface (Zoski, 2015). Conversely, in the positive approach curve I rises above unity ($i_T > i_{T,\infty}$) (Figure 1.3.B). The current of the tip in this mode of operation depends on the electrochemical activity of the surface and the topography. Because the approach curves are plotted using dimensionless variables, they can be used to determine the tip to substrate distance once a is known, independent of the mediator concentration. In addition, the negative approach curve may be used to determine the *RG* of the UME. *RG* is defined as the diameter of the insulating sheath of the electrode divided by the diameter of the electrode (Polcari et al., 2016; Zoski, 2015).

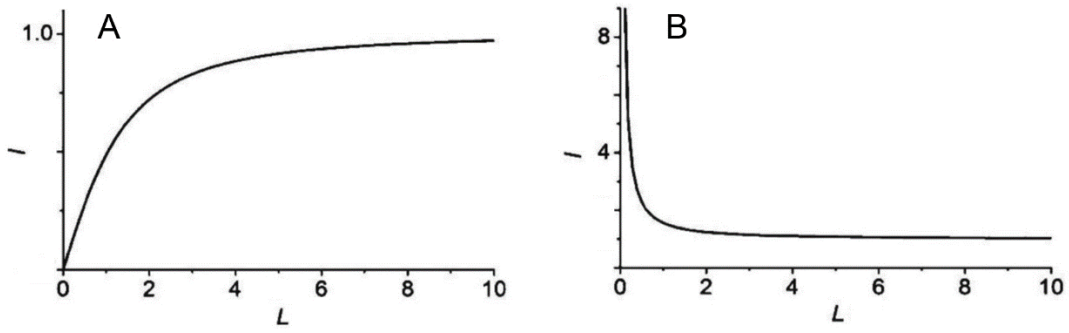

Figure 1.3 Negative and positive approach curve (A,B) (Zoski, 2015)

Collection/ Generation Mode: CG mode is another useful and important operating mode of SECM that is widely used for concentration detection and determining the chemical flux at the substrate. GC mode can be implemented in two ways:

Substrate Generation/Tip Collection (SG/TC): Converted electrochemically active species are produced at the substrate and collected at the tip of the electrode. (Figure 1.2.C). Normally, the current is measured at both tip and substrate surface (Huang et al., 2018; Polcari et al., 2016). For example:

Reaction at the tip $\mathrm{O} + \mathrm{ne} \rightarrow \mathrm{R}$ (1.1)

Reaction of the O generation at substrate $\mathrm{R} - \mathrm{ne} \rightarrow \mathrm{O}$ (1.2)

Since SECM is very useful for detecting concentration profiles, it is possible to detect active spots at the surface where the electrochemical reaction occurs at a higher rate. (Zoski, 2015). As such, it is useful for studying the electrocatalysts used in water oxidation. Generally, dimensions of the substrate sample (a_s) and tip (a) are important in SG/TC and usually ${a_s}/{a} \gg 1$. As a result the diffusion layer of the substrate is much larger than the one for the tip and presumably there will be no recorded current at the tip before biasing the substrate. Therefore, there is no contribution of the current at the tip through the feedback mode. (Huang et al., 2018; Polcari et al., 2016).

Tip Generation/Substrate Collection (TG/SC): The reverse process is in the TG/SC when the electroactive species generated at the tip, are collected at the surface. Here again the current is measured at both the substrate and the electrode tip. If the objective is to study again the reaction of $R \rightarrow O$ at the substrate the reaction sequence is:

Reaction of the O generation at the tip $R - ne \rightarrow O$ (1.3)

Reaction at the substrate $O + ne \rightarrow R$ (1.4)

Immediately after biasing the potential of the tip and substrate, the current of the substrate (i_s) is low. Over time, the O species are produced at the tip and diffuse to the substrate and i_s increases and eventually when a steady state is achieved, i_t and i_s become equal. In this case, if the tip is close enough to the surface of the substrate ($L \leq 2$), then the R generated species mainly diffuse to the substrate, and subsequently the current of the tip and substrate become equal (Zhou et al., 1992). Figure 1.2.D demonstrates the process of TG/SC. This mode is usually chosen to study the kinetic of a reaction or to make modification on the substrate (Polcari et al., 2016).

Redox competition mode (RC-SECM): The RC operation mode of SECM is not as old and conventional as the other modes such as feedback or CG. It was first introduced by Schuhmann (Eckhard et al., 2006). In this operation mode, both the tip and the substrate are competing to react with the same redox active species and are located in close proximity together in the experimental setup. A potential is applied to both probe tip and substrate, but the current is measured only for the probe tip. As a result, the sensitivity and lateral resolutions rise due to reducing the contribution of background current. In fact, the method is mainly used for studies in which a high sensitivity is necessary for detecting the signal. For instance, it was used for detecting the localized activity of the bilirubin oxidase/Os-complex modified electrodeposition polymer spots for the biocatalytic activity (Huang et al., 2018).

In the irreversible reactions such as oxygen reduction reaction (ORR), this method has very attractive performance in comparison to CG mode. For instance, it is possible to apply a constant reduction potential to the substrate and a reductive potential pulse to the tip. By scanning over the sample, if the area is electrocatalytically active, some

oxygen is consumed by the active spots of the sample and the current will drop at the tip, and conversely, when scanning over an inactive area, the UME tip current remains constant. Therefore, this decrease in the current of the tip can be correlated to the catalytic activity of the surface and an image can be formed (Eckhard et al., 2006). Figure 1.2.E visualizes the process of RC-SECM in a simple scheme.

Direct Mode: This mode is mostly used for surface modification. For instance, the surface changes during scanning force or tunneling (Pust et al., 2008). As Figure 1.2.F demonstrates, there is an electric field between the tip of the UME and the substrate. In the cell set up, the tip is used as the counter electrode and the substrate is the working electrode. By applying the potential, the electrochemical reactions start at the tip and substrate and by choosing a small tip/substrate distance, the localized modification or analysis is feasible. The result of this cell assembly and imposing potential can be a metal etching reaction or a direct deposition. In addition to surface modification, this mode has various applications in biological studies such as enzyme deposition (Fan et al., 2007; Polcari et al., 2016).

For instance, this mode is utilized by Schwamborn et al. for catalytic deposition of Fe on the surface of glassy carbon (GC) (Schwamborn et al., 2010). In this experiment, a pulled micropipette contained counter electrode (iron) moves across the surface of the GC in close proximity to the surface. By biasing the potential of Fe deposition, it is deposited to the surface of the GC directly from the counter electrode. The key feature of the direct mode is that iron deposits in the target area of the surface from the miniaturized counter electrode and it is not deposited beneath the desired area.

Potentiometric Mode: The different modes described above were amperometric measurements in which the quantity of the tip current and substrate were detected. Unfortunately, there are many chemical systems that involves species with reduction potential outside of the solvent window. In such systems it is impossible to detect these

species using the above described methods. In live cells, for instance, having information about the quantity of the metal ions provides very important information, however, their detection is impossible by redox based techniques due to the aqueous media in the cells (Horrocks et al., 1993; Wei et al., 1995).The potentiometric mode of the SECM introduces ion-selective probes with the high resolution. In this mode, there is no faradaic current to detect, as the measured signal is the potential between an ion-selective electrode (ISE) and an internal reference electrode. Here, the fundamental mechanism of the detection is based on the differences in the chemical activity of the internal solution of the ISE and the external solution, which creates a junction potential in the ion-selective membrane of the ISE. An ISE is composed of a glass capillary filled with the solution of the target ions, an internal reference electrode and also an ion-selective membrane (Polcari et al., 2016; Serrapede et al., 2013). Figure 1.2.G shows a scheme of ISE in a SECM set up. The measured potential difference has a linear dependence on the activity of the target ion in the sample solution. This technique is very useful for pH sensing in systems such as enzyme reactions in cells or corrosion processes (Horrocks et al., 1993).

1.2.3 SECM Mediators

In SECM experiments, there is a redox mediator in solution with the electrodes, and during the electrochemical experiment, this mediator is reduced (or oxidized) at the tip of the electrode (Creighton & Withnall, 2000). The selection of an appropriate mediator depends on the nature of the sample and the mode of the SECM experiment. An important selection consideration is the electrochemical stability in the potential window of the experiment. In the feedback mode, the mediator should be able to reversibly oxidize (or reduce) by changing the potential and should have fast heterogeneous kinetic at the tip (the substrate reaction kinetic should be the rate-

determining step). Of the 133 species of mediators used in SECM experiments, 102 species are suitable for use in feedback mode (Polcari et al., 2016) 45 mediators for GC modes and 7 mediators in RC mode.

Although various redox mediators are used in SECM operational modes, there are some general considerations for mediator molecules. For instance, it should be inert in the presence of working reference and counter electrodes that are in the same solution and needs to be chemically and thermally stable in the experimental environment. In addition, since various properties of the mediator such as pH dependence, lipophilicity, or diffusion coefficient in different solutions may affect the experimental result, these factors need to be carefully considered during SECM experiment (Cai et al., 2002; Longobardi et al., 2006; Polcari et al., 2016).

In spite of the fact that a big number of mediator molecules are reported for use in SECM experiments, in some special cases it is impossible or very hard to find a proper mediator to use in the feedback mode and it is necessary to find an alternative to adding a mediator to the solution. For instance, in a highly negative potential domain, most of the mediator molecules will decompose. In this thesis, for local detection of Li^+ ion current using ASV technique, a highly negative potential for Li^+ reduction (0.0 V vs. Li/Li^+) is needed. The choice of mediators is therefore very limited as decomposition and Li^+ ion reduction is simultaneously happening at the electrode.

1.2.4 Electrochemical Instrumentation

As mentioned in the previous sections, the bipotentiostat is an important part of SECM. Normally it should have at least one port with low current capability in the pico to femto-ampere range. In a potentiostatic experiment, the current of the electrochemical

cell is measured and the potential is controlled, i.e. the potentiostat controls the potential of working electrode in the electrochemical cell. Normally the external cables are connected to the working, counter and reference electrodes. In comparison there are many internal connections inside the potentiostat that forms circuits to generate and measures the potential and current. During operation the potential of the working electrode is set with respect to the reference electrode of the cell, this may cause current to flow between the working and the counter electrode. Note that there is no flow of current between reference and working electrode (Reducks, 2020). Almost no current flows though the reference electrode so that the chemical composition and the potential of this electrode should remain constant during the experiment.

In this thesis by applying the chosen potential (or a specific potential range) the response of the system in form of current is registered by the potentiostat/bipotentiostat. The main components of a potentiostat are depicted in Figure 1.4. Voltmeters and amperemeter record the voltage and current between reference and working and counter and working electrode respectively. Also, as explained above, during operation, the potential difference between working and reference electrodes of the electrochemical cell is controlled by applying a current between the auxiliary/counter electrode and the working electrode.

1.2.4.1 Electrodes

In the three-electrode cell there is a working electrode, a counter and a reference electrode. Generally, as the potential relative to the reference electrode is scanned/controlled at the working electrode, current is injected or sunk through the counter electrode. Figure 1.4 shows the scheme of a potentiostat. Based on the electronic design, there is a large impedance between reference and working electrode,

and therefore, the current passing between reference and working electrode is negligible. In contrast, current can easily pass through the counter electrode, The counter electrode in general is an inert material such as Pt, Au, graphite or glassy carbon with a large surface area (about ten times larger than the working electrode). (EC08, 2011).

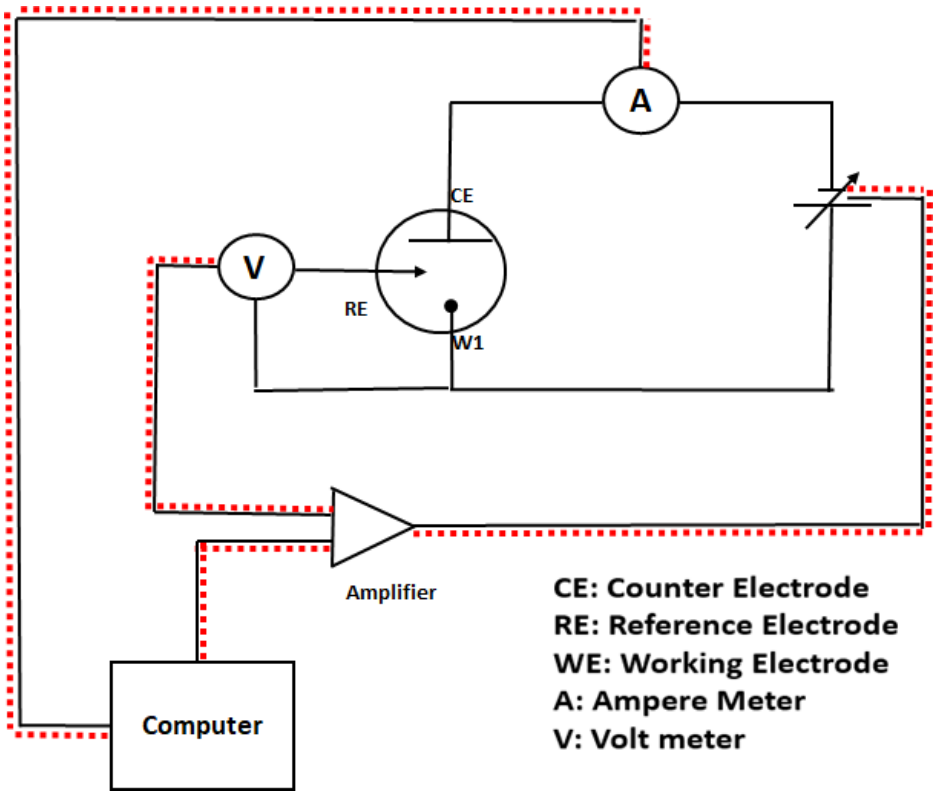

Figure 1.4 Scheme of potentiostatic mode of potentiostat. The red lines in the figure are representative of the signal path.

An electrode with stable and well-defined potential is utilized as the reference point in the electrochemical cell. Usually saturated calomel electrode or silver/silver chloride is used as reference electrodes in aqueous solutions. However, in non-aqueous solutions there is a possibility of electrolyte leakage into the analyte solution which can

affect the electrochemical reactions. Thus, *pseudo-reference electrode* (literally “false” reference) or *quasi reference electrodes* (i.e. “essentially” or “almost” reference) are used. (Inzelt, 2013) These include a piece of silver wire with a freshly polished surface as reference electrode. In this case, the oxide layer that naturally covers the surface produces the Ag_xO/Ag quasi reference electrode. Ideally, the silver wire is kept in a wet oxygen filled environment before use as a reference to be sure that the surface is covered with a layer of oxide. In many electrochemical experiments with low current, such as nanoampere, using quasi reference electrodes has significant advantages. For instance, using an Ag QRCE (Ag quasi reference counter electrode) in a two-electrode system has advantage over utilizing an Ag/AgCl reference electrode isolated from the solution with a frit. (Presence of a thick frit can increase the resistivity and decrease the rate of mass transport to the QRCE and possibility a decrease in detected current.).

1.2.4.2 Control Amplifier

The control amplifier in the potentiostat assembly, (Figure 1.4) is a servo type electronic amplifier. During the operation, the potential difference between reference and working electrode is measured and compare to the desired potential. Based on this difference, the control amplifier will increase or decrease the potential between the working electrode and the counter electrode thereby increasing or decreasing the current that flows in the cell (Gamry Instrument, 2015)

1.2.4.3 An Overview on Operation of Potentiostat and Bipotentiostat

In the electrochemical cell of Figure 1.4, electrons transport the charge through the external circuit, whereas ions are the charge carriers between the working and counter electrodes. At the interface of electrode/ electrolyte, there must therefore be conversion between the two charge carriers. This is known as charge transfer or the redox process. Combined charge transport and charge transfer form a closed loop, so

Kirchhoff's law, permits the current to be measured anywhere in this loop. An amp meter is therefore conveniently included in the external circuit.

The electrochemical cell can be considered as a series of impedances, including the impedance of the working electrode and electrolyte, as well as the impedance of the counter electrode and electrolyte solution, and also the resistivity of solution itself (Bard & Faulkner, 1983). Consequently, there is a voltage drop across the electrochemical cell. This voltage drop is given to one of the amplifier inputs. The second input is the desired potential given by the computer. The amplifier checks both of these inputs and if the measured voltage by voltmeter is higher than desired voltage (given on the computer), the amplifier regulates the source in such a way to reduce the current. If it is a lower value, the amplifier increases the source current

In some electrochemical experiments such as SECM, it is important to be able to control two working electrodes simultaneously and a bipotentiostat is required for this purpose (Figure 1.5). The principle of operation is similar to a simple potentiostat, however, here, there are two working electrodes (W1, W2) and the potential of these electrodes are controlled independently by two control amplifiers. Generally, one working electrode (W2 in the SECM of chapter 4) is selected to produce the desired reaction while the W1 (or tip) is responsible for monitoring the current. In the experimental section of chapter 4 of this dissertation, which focuses detection of lithium-ion diffusion from a $LiFePO_4$ film, the bipotentiostat is used to control two working electrodes: W1) the SECM probe and W2) the $LiFePO_4$ film. Figure 1.5 is a scheme of a bipotentiostat.

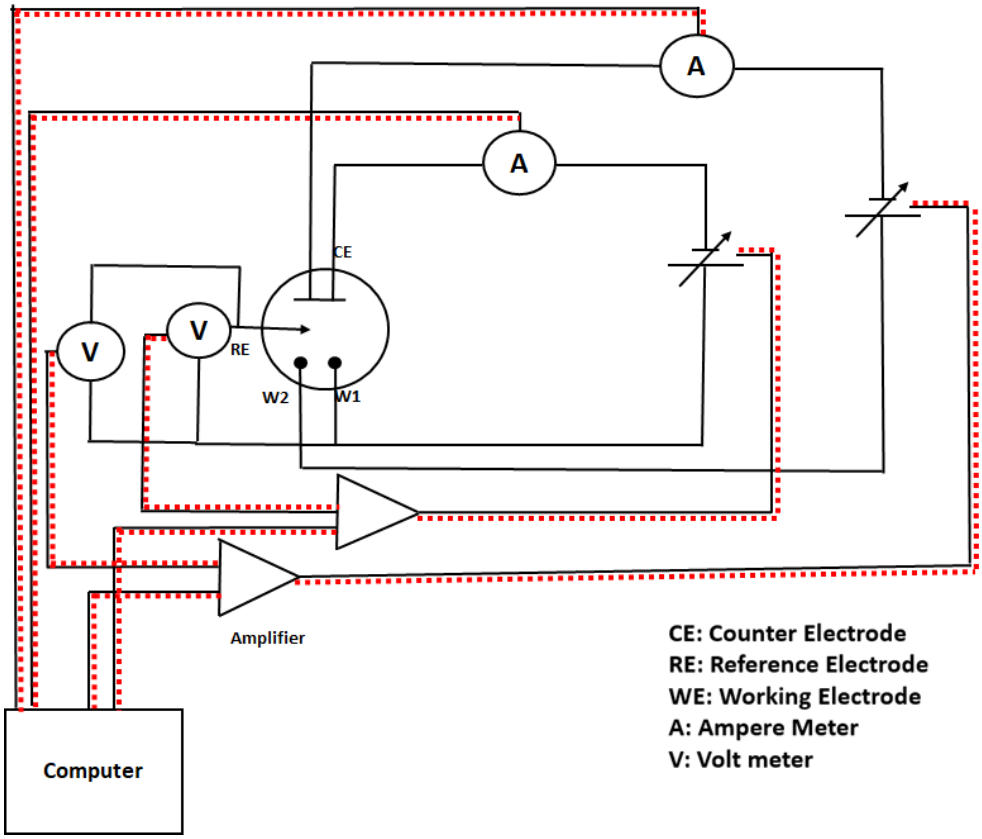

Figure 1.5 Scheme of a bipotentiostat. The red lines are representative of signal path.

1.3 Steady State Current of Microelectrodes

The electrochemical behavior of a microelectrode with a small diameter is different from what is observed from a macroelectrode. Solid electrodes used for voltammetry are usually prepared by encapsulation of the electroactive material in a nonconductive sheath such as a polymer. The most common sheath is Teflon, poly-chlorotrifluoroethylene or Kel-F and the commercial size is usually 1, 2 or 10 mm in diameter of the conductor. The current produced from these electrodes in a 1.0 mM analyte solution is typically from mA to μA. In comparison, the diameter of the

microelectrodes is 25 μm or less and the current range is nanoampere or less. To explain the difference in the current response from these electrodes, we will first consider a mm size electrode. The working electrode is in the solution, which contains redox active material, reference and counter electrodes. By sweeping the electrode potential in this solution from the potential where no redox reaction toward ones that the redox reaction starts, electron transfer of the species will occur at the interface of the electrode and electrolyte. Thus, the concentration of the redox active species in solution decreases and a concentration gradient is created.

An important factor in the current of microelectrodes is their diffusion layer. Generally, the diffusion layer is defined as an volume close to the electrode surface where the concentration of the redox materials is different from the bulk of the solution (McNaught & Wilkinson, 1997; Wikipedia, 2021). In voltammetry experiments, the thickness of the diffusion layer depends on the scan rate. At a sufficiently short time (high scan rate), the diffusion layer is immediately depleted from the redox species and its thickness is much smaller than the electrode radius. In this case, all electrodes, UME or macro acts as a large planner electrode.

Alternatively, no matter how large is the dimension of the electrode, over a sufficiently long period of time, hemispherical diffusion is dominant rather than the planner one. In this case, the current reaches a steady state. Generally hemispherical diffusion yield a sigmoidal shaped CV (Forster & Keyes, 2007; Stulík et al., 2000).

Figure 1.6 demonstrates the spherical and linear diffusion observed at long and short time intervals. As it can be seen in Figure 1.6.A, the direction of the diffusion is perpendicular to the electrode surface in linear diffusion. In Figure 1.6.B the flux of the redox species to the surface of the electrode is hemispherical.

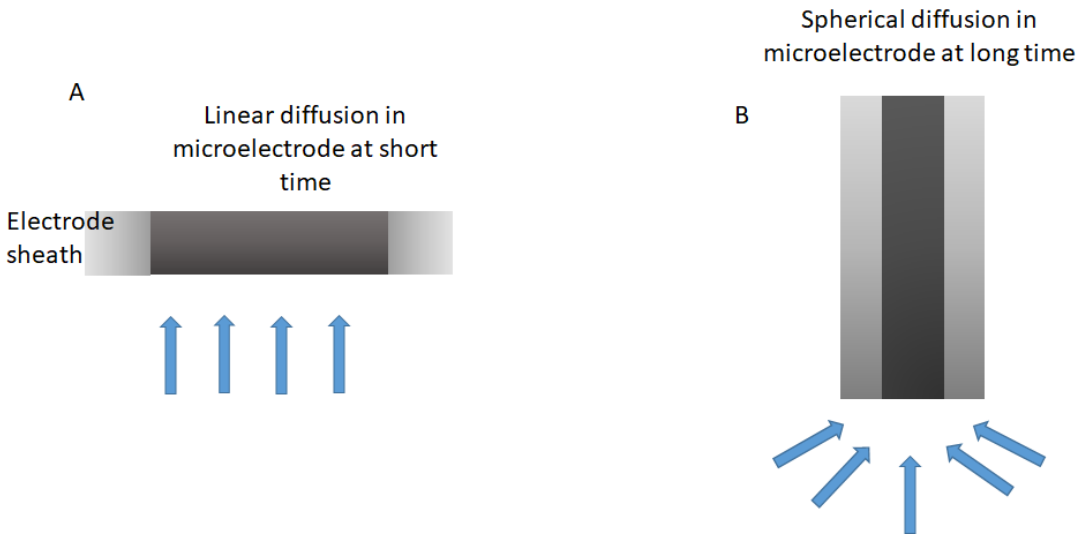

Figure 1.6 Illustration of linear diffusion observed in short time (A), and spherical diffusion observed at long time (B). Blue arrows indicate the direction of the flux. The steady state current of the redox material at the electrode surface is proportional to the concentration of the mediator and governed by the equation 1.5 (Danis, Polcari, et al., 2015).

The steady state current at the electrode surface is proportional to the concentration of the redox material and governed by the equation 1.5 (Danis, Polcari, et al., 2015).

$$i_{ss} = 4nDFCa\beta(RG) \qquad (1.5)$$

Here, F and n are the Faraday constant and number of transferred electrons and a is the radius of the electroactive area. D, C are the diffusion coefficient and concentration. Here β is the geometrical factor related to $RG.RG$ calculated from (Bergner et al., 2013):

$$\beta(RG) = 1 + \frac{0.23}{(RG^3 - 0.81)^{0.36}} \qquad (1.6)$$

The timescale in which the dominant behavior is a steady state and the current is sigmoidal rather than duck shaped can be gauged based on the dimensionless parameter X:

$$X = \frac{(\pi Dt)^{\frac{1}{2}}}{r} \qquad (1.7)$$

Where X is representative of a higher contribution of steady-state response, *D* is the diffusion coefficient, *r* is the radius of the electrode and *t* is the time. It is thus possible to calculate the minimum time scale of the experiment in which the steady-state current is dominant, and the obtained CV has a sigmoidal shape. For instance, for a 5µm Au microelectrode, in a solution of ferrocene, the contribution of the steady-state current is 10 times bigger than the non-steady-state one (*X*=10), when the scan rate of the experiment is 100 times slower. This effect is portrayed in the Figure 1.7.

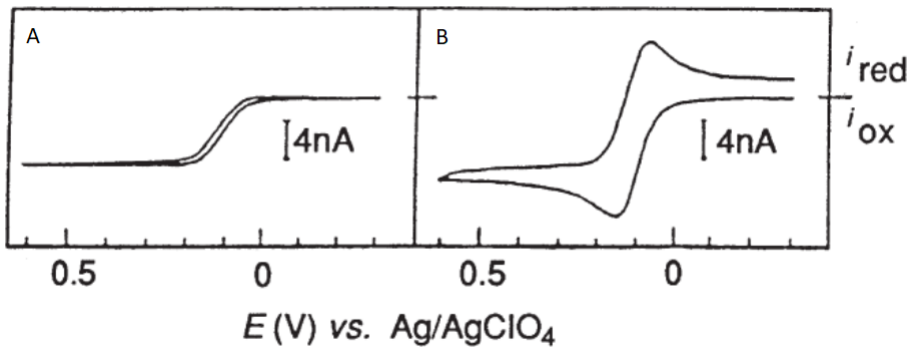

Figure 1.7 Effect of scan rate on the shape of the voltammogram at the 5µm Au microelectrode (solution: 1.0 mM ferrocene in acetonitrile and 0.1 M tetrabutyl ammonium perchlorate as support electrolyte). Scan rate: 0.1 V s^{-1} (A). Scan rate 10 V s^{-1} (B) (Forster & Keyes, 2007; Howell & Wightman, 1984).

1.4 SECM Probes

An important consideration of the SECM experiments is the selection and design of the probe. The resolution of SECM measurement is strongly affected by the size of the

probe. Probes with the tip in micrometer to nanometer scale are commonly used. There are two main categories of SECM probes: amperometric and potentiometric. In most of the cases, however, amperometric probes are more practical for use as probe than the potentiometric one.

Generally, the use of potentiometric sensors is more limited than that of amperometric types. Yet, the high selectivity for specific analyte makes them a choice for detecting localized pH change. These types of probes are used in the study of corrosion (Klusmann & Schultze, 1997; Nazarov et al., 2013) and kinetic of the reactions (Csoka & Mekhalif, 2009). For instance, antimony based pH sensor was utilized to study the possible change in pH during the corrosion process by Bard et al. (Horrocks et al., 1993).

Amperometric probes detect the current in the SECM experiments, i.e. the faradaic current from the electrochemical reaction of species at the interface of the working electrode and liquid electrolyte. They enjoy advantages such as fast preparation and long lifespan (they can be functional for several months or years) (Fan et al., 2007).

As a result of these benefits, amperometic-based measurements are more prevalent and they are widely used for detection of heavy metals (Chen, L. et al., 2010; Jothimuthu et al., 2013; Pei et al., 2014; Xu, Y. et al., 2016), drugs (Hassan et al., 2020; She & Allen, 2019; Shukla et al., 2020), oxygen (She & Allen, 2019) and biomolecules (Brownlee et al., 2020; Gherab et al., 2020).

While the dimensions of amperometric probes have changed, compare to conventional electrochemistry, the nature of the electrochemical process, has not. As a result, it is possible to keep the high sensitivity and low limit of detection (LOD) in these experiments and reduce the volume of evaluated solution by order of 1000 (considering

the volume of µL instead of mL) without changing in fundamental elements of detecting such as reproducibility (Baracu & Gugoasa, 2021).

1.4.1 Geometry of Probes

The most conventional type of amperometric probe is fabricated in the form of a disc, with an electroactive area of a metal such as platinum or gold surrounded by an insulating sheath (e.g., glass or quartz or plastic).

SECM probes are also available in geometries other than discs such as hemispherical (Pt/Hg microelectrode), conical (Pt/Ga microelectrode), ring (Au ring microelectrode) and different sizes from 25µm to several nanometers. In the SECM scans, the small *RG*s provide minimum tip to substrate distance, which increases sensitivity. In probes with smaller *RG*s (i.e. *RG*s less than 5) the current is greater because there is a high contribution of the back diffusion from the redox molecules of the solution (Lefrou & Cornut, 2010). In these probes the chance of probe misalignment in contact with the substrate is reduced (Danis, Polcari, et al., 2015). Although many SECM experiments have previously been performed using *RG* =10, recent reports indicate that small *RG*s (less than 3) are good choice for SECM scans based on above explanations (Polcari et al., 2016).

Despite their general shape, SECM probes can be divided into two main groups: solid probes (e.g. Pt or Au micro disk) and liquid probes (e.g. Pt/Hg microelectrode). Choosing the proper probe depends on the voltammetry experiment. In negative potential regions where the reduction of hydrogen at the surface of the Pt obscures the reduction of the redox molecule in the solution, a Pt/Hg electrode can be substituted

(Mauzeroll, 2007a). In particular, utilizing a Pt/Hg liquid electrode allows for the detection of species with very negative reduction potential such as Mn^{2+} (-1.18V vs. SHE). For instance, in a solution containing the cations of zinc, manganese, or copper ions using a Pt/Hg microelectrode, the cations reduced to their metallic state and dissolved in the mercury to form an amalgam. Sweeping the potential in the positive direction, will oxidize the metal ions and return them to the electrolyte. The charge of this oxidation is therefore a measure of the amount of material dissolved in the mercury. Apart from mercury, there are other examples of metal-film based probes in SECM experiments. For instance, Pt/Bi or C/Bi microelectrodes (Baldo et al., 2003), Ga UME (Wei et al., 1996) have been fabricated and used as probes. Generally, these probes are used for detection of metal cations with low limits of detection, and without the problem of dendrite formation on the electrode surface. The last feature of these probes is that since the metals are absorbed and alloyed with liquid their stripping step originate from a liquid media such as Hg or Ga. However, a stripping step from a solid electrode, where it is more likely that the deposited metal has formed dendrites, are generally uniform.

1.4.1.1 Phase Diagram of Metal and Liquid Electrode

In general, information about solubility of absorbed metal in Hg liquid electrodes and the distinct phases, is given in phase diagrams. In this thesis the relevant ones are Mn-Hg, Li-Hg, and Ga-Li.

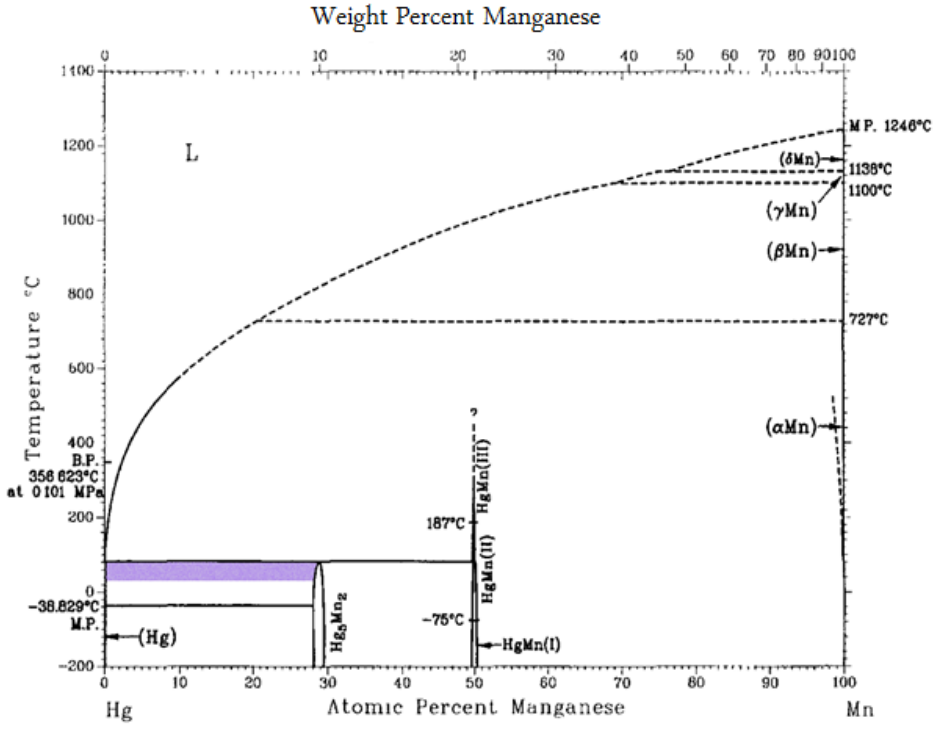

Figure 1.8 Phase diagram of Mn-Hg system (Moser & Guminski, 1993)

In second chapter, a Pt/Hg microelectrode is utilized for manganese ion detection. Since the Mn detection experiments take place at the room temperature, the purple zone of the phase diagram (Figure 1.8) is relevant. Up until 30% atomic percentage of Mn a mixture of the solid intermetallic compound (Hg_5Mn_2) in liquid Hg is formed. Above

30% of Mn a solid phase is formed that contains intermetallic compounds (Moser & Guminski, 1993). As a result, the detection of Mn^{2+} ions for the first 30% is from liquid mercury resulting in a smooth stripping peak. Absorbing Mn for more than 30 percent in mercury electrodes raises the possibility of formation a solid phase at the surface of Hg. Subsequently, the Hg microelectrode will be blocked and it is a serious problem for further stripping of the absorbed manganese amalgam. For the lower percentages of Mn where detection of metal cation is feasible, there is a liquid/solid mixture and it seems that the diffusion of solid intermetallic compound into the mercury core from the surface is faster than the deposition of metal, so the solubility limit is never reached in our experiment of detection. This means that there is no solid formation at the surface of the mercury. The other possible explanation is that the rate of nucleation of Hg_5Mn_2 on Hg is insufficient to cause crystallization at the Hg electrode. As a result, the detection of Mn using Hg in the concentration range that is reported here in this thesis is feasible.

The other case of study in this dissertation is the detection of Li^+ using Pt/Ga microelectrode in the third and fourth chapters. The phase diagram of Li and Ga is shown in Figure 1.9.A Gallium is a metal that is liquid at 29°C, so in this thesis it is used as a liquid electrode. Phase diagram shows that the Ga/Li mixture is liquid up until addition of 1.7% atomic percentage. As a result, the Li ions stripping from a liquid alloy is feasible and there is no blocking of microelectrode if plating concentrations are kept below this threshold. Compared to Ga, by selecting Hg as a probe for Li^+ ion detection, the amount of lithium that can be added to the mercury before appearance of solid phase is relatively low. Considering the tendency of Li^+ to form dendrites, the stripping step from the Hg electrode is unreliable. As a result, liquid Ga is more favorable to probe for Li^+ ion detection than the mercury one. Figure 1.9.B shows the binary phase diagram of the Hg and Li.

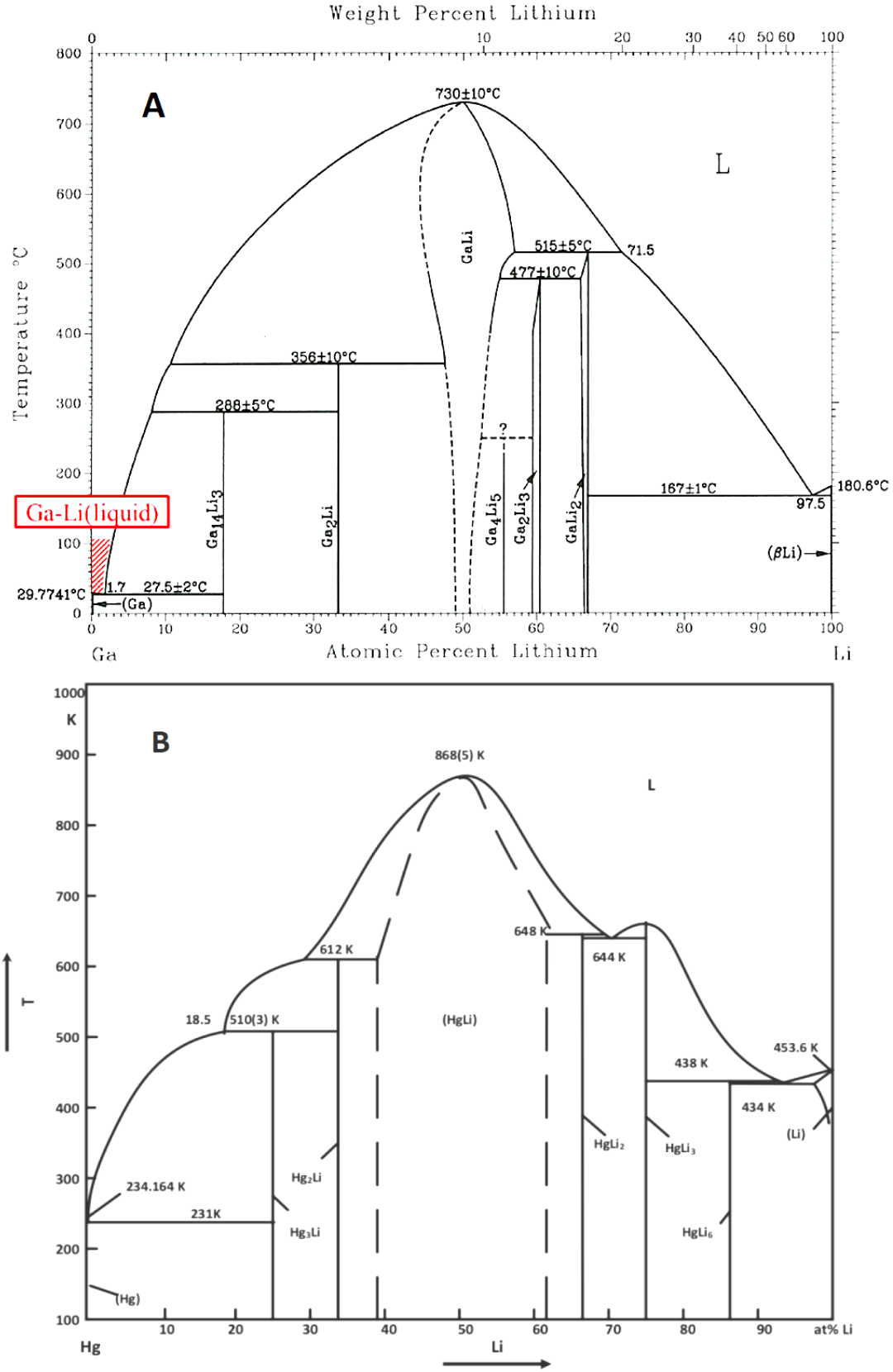

Figure 1.9 Phase diagram of Ga-Li (A), Hg-Li systems (B) (He, G. et al., 2019; Suzuki et al., 2019)

1.5 Stripping Voltammetry

In the field of electroanalytical chemistry, stripping voltammetry (SV) has been extensively used due to its high sensitivity and extremely low limit of detection (10^{-10} mol L^{-1}). It is based on two individual steps:

1) Preconcentration step, in which the analyte is accumulated into the working electrode.
2) Stripping steps, in which the absorbed analyte on the working electrode strips back to the solution from the working electrode.

The analyte stripping step creates a peak in the voltammogram where the height or area (under the current) is proportional to the concentration of the target analyte in the solution (see section 1.5.3). Stripping voltammetry depends on the nature and characteristic of the preconcentrated analyte and the direction of the potential sweeping and has three major versions. The first one is ASV where cathodic preconcentration of metal in Hg, followed by the stripping as the potential is scanned in the positive direction. In ASV, the stripping peak is an oxidative (anodic) current.

The other one is the cathodic stripping voltammetry (CSV), which is less common. This one is very similar to the ASV, however, here an oxidizing potential accumulate the analyte on the electrode and subsequently a reduction potential causes to strip the oxidized species. This technique is mainly for anions accumulation in the form of insoluble salt on the working electrode. Subsequently cathodic stripping step takes place by scanning to more negative potentials.

The last form of SV is the adsorptive stripping voltammetry (AdSV), in which the analyte is accumulated onto the working electrode by adsorption and then followed by a potential scan toward positive potentials at the stripping step (similar to ASV). The

analyte can be organic or metallic molecules. The key difference between AdSV and ASV is the accumulation step. In AdSV, accumulation step is based on the spontaneous adsorption of the analyte to the surface of the electrode, however, in ASV, the analyte accumulation at the electrode surface is due to the application of the reduction potential (Wikipedia, 2020).

As it is mentioned in previous paragraph, the ASV is the most popular technique due to important features such as low cost and high accuracy in detection in addition to low detection limit. Because it is applicable for elemental analysis, it is used extensively for detection of metal cations in the water or soil as well as different pharmaceutical, clinical, industrial and food samples (Abollino, O. et al., 2019; Daniele, S., 2005). In this thesis, the ASV will be utilized as a technique for metal cation detection in non-aqueous solution of LIBs.

1.5.1 Anodic Stripping Voltammetry

In classic ASV, metal cations from the solution sample are absorbed into the electrode, as they are reduced into their elemental form during the cathodic potential scan (Daniele, S., 2005). The two steps of ASV are:

$$M^{n+} + ne^- + L \rightarrow M(L) \qquad (1.8)$$

$$M(L) \rightarrow M^{n+} + L + ne^- \qquad (1.9)$$

Where L is the liquid or substrate electrode. ASV can be utilized for detection of more than 20 metal cations such as lead, cadmium, zinc, copper, antimony, etc. (Daniele, S., 2005). In most cases, ASV uses mercury electrode so that an amalgam is formed:

$$M^{n+} + ne^- + Hg \rightleftharpoons M(Hg) \qquad (1.10)$$

Figure 1.10 illustrates the potential profile of ASV of a metal cation, where the first steps is the absorption of metal cation into the mercury and the second step is stripping of the metal cation.

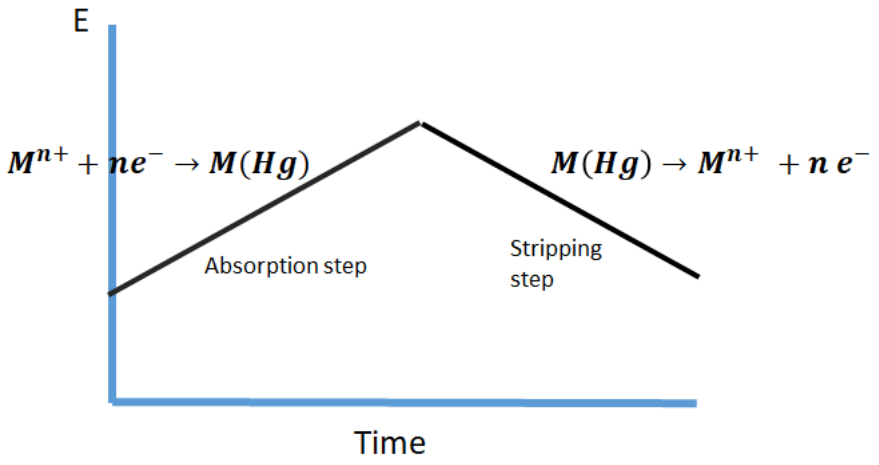

Figure 1.10 Diagram of absorption and stripping of analyte in ASV

The voltammetry analysis of metal cation detection using ASV takes place under conditions of minimum resistance and migration in which the transportation of the species are diffusion controlled. In order to establish this state, a supporting electrolyte (usually a salt or acid) in the concentration range of 0.2-0.5 M is added to the solution (Abollino, O. et al., 2019). Typically during the ASV experiments only a small fraction of the metal cations accumulate on the working electrode (Abollino, O. et al., 2019).

1.5.2 ASV Using Mercury Working Electrode

Since the advent of SV, there have been two types of mercury working electrodes. First, hanging mercury drop electrode (HMDE) consists of a small droplet of mercury hanging from the tip of a glass capillary, and second, thin mercury film electrode (TMF) produced by coating a layer of mercury on the surface of a conducting substrate (Economou & Fielden, 2003; Illuminati et al., 2015). The mercury thin layer is deposited from a solution of Hg ions and can be prepared *in situ* or *ex situ* prior to analysis. Figure 1.11 exhibits both hanging drop and thin film types of mercury electrodes. Some other kind of metals such as Pt, Ag, Au and Ir have been used as the substrate for mercury film deposition in the TMF fabrication, but the most common substrate used for this purpose is glassy carbon as it appears to produce the best result (Abollino, O. et al., 2019).

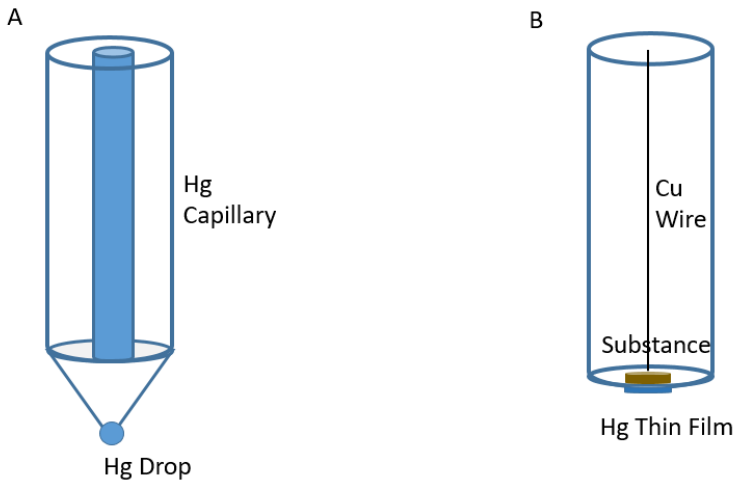

Figure 1.11 Scheme of a HMDE (A), TFM (B) (Abollino, O. et al., 2019)

HMDE and TMF both provide wide cathodic potential range and high overpotential for hydrogen generation, important for metal cation detection. However, the anodic

range of the potential sweeping in ASV is limited by the Hg oxidation. Importantly for this thesis, Hg UMEs can be used as a SECM probe for local cation detection.

1.5.3 Stripping Step in ASV

The measurement step is carried out in a solution (without stirring) by applying a proper stripping potential. Typically, the potential is swept in the reverse direction of the metal absorption, and the accumulated metal cations are reoxidized to give a peak in the voltammorgam. The recorded voltammogram shows the potential of the stripping peak, which provides qualitative identification information. The height or area below the peak provides quantitative information about the concentration of the metal cations in the solution. For instance, by extracting the peak heights for a series of metal cation solutions with different concentrations and preparing the current/concentration diagram, a calibration curve of metal cations in the experimental conditions will be obtained (Daniele, S., 2005). For the stripping step of the ASV, various voltammetry techniques such as linear sweep voltammetry (LSV), differential pulse voltammetry (DPV) and SWV can be applied (Abollino, Ornella et al., 2008). LSV is the basic one, as the potential of the working electrode is swept linearly. DPV and the SWV are more sensitive and SWV is the best choice in many cases (Abollino, O. et al., 2019) which was confirmed in this thesis works. ASV gave unreliable results using LSV. Where SWV was found to be very reliable.

1.6 Different Pulse Voltammetry and Square Wave Voltammetry

The potential profile in DPV consists of the superposition of short pulses on a linear potential ramp LSV, and the potential increase equally between the two pulses. In this

case, the current is measured two times: first before applying the current, and the second time is at the end of pulse application, and the final current is the difference of the first and second one. The most important feature of this voltammetry is recording a faradaic current with a minimum contribution of charging current or non-faradaic current (Simões & Xavier, 2017; Venton & DiScenza, 2020). That principle of DPV is similar to SWV.

SWV is one of the most sensitive pulse techniques (Batista Deroco et al., 2020) and can be used to perform experiments much faster than the conventional voltammetry. If we consider that pulse techniques have a scan rate between 1 to 10 mV/s, the SWV can utilize a scan rate of 1V/s, which leads to faster determination. For instance, recording a voltammogram using LSV or DPV which takes several minutes, could be performed in few seconds using SWV (Princeton, 2010).

The potential waveform of the SWV is shown in the Figure 1.12 is a superposition of a square wave onto a staircase. The timing of the SWV (Figure 1.12) is characterized by τ, the duration of the time for one square wave cycle. The frequency of the SWV is $1/\tau$ in Hz. E_{step} is the step size in mV which is the base increment during the potential sweeping. E_{sw} is the height of the square wave pulse or plus amplitude (Wikipedia, 2021b). In a SWV experiment, the scan rate is given by:

$$S = \frac{E_{Step}}{\tau} \qquad (1.11)$$

so by imposing a high frequency, τ become smaller and subsequently the scan rate of technique is high. In SWV, the current is sampled twice for each square wave cycle, once at the end of the direct pulse (I_1) and once at the end of reverse pulse (I_2) (Figure 1.12). The key signal is as the differential current ($\Delta I = I_2 - I_1$). By delaying the current sampling to the end of the pulses and plotting ΔI against the staircase potential, the

currents obtained relates primarily to the faradic current and the contribution of non-faradic current is diminished.

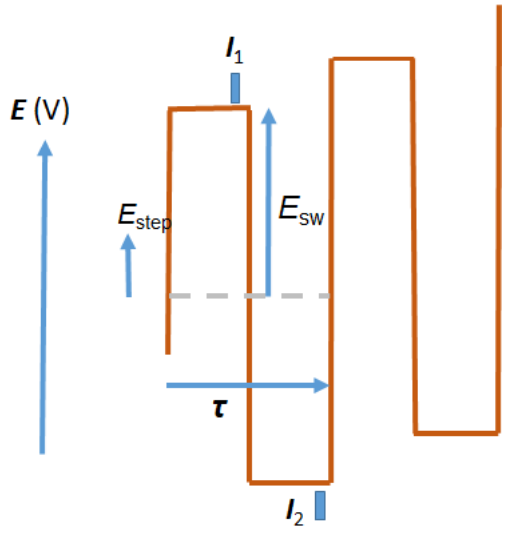

Figure 1.12 Potential waveform in a SWV

As it was mentioned earlier, the current of the voltammogram of SWV is the subtraction of the forward sampled current from the reverse ones (Bard & Faulkner, 1983). Figure 1.13 demonstrates the direct, reverse and the subtraction result voltammogram for a reversible O/R redox reaction. The subtraction result shows a larger peak because the individual peaks have the opposite signs. In other words, the forward-square wave step produces R registered as a cathodic current, and the reverse reaction produces O with showing an anodic current, and as the currents have different signs, the resulting current ($\Delta I = I_f - I_r$) has a higher peak. Also, it should be mentioned that the potential of the SWV peak is almost equal to the half-wave potential or $E_{1/2}$ LSV.

Figure 1.13 shows that the peaks of forward, reverse and result in the voltammogram have the same potential (Bard & Faulkner, 1983, 2001; Westbroek, 2005).

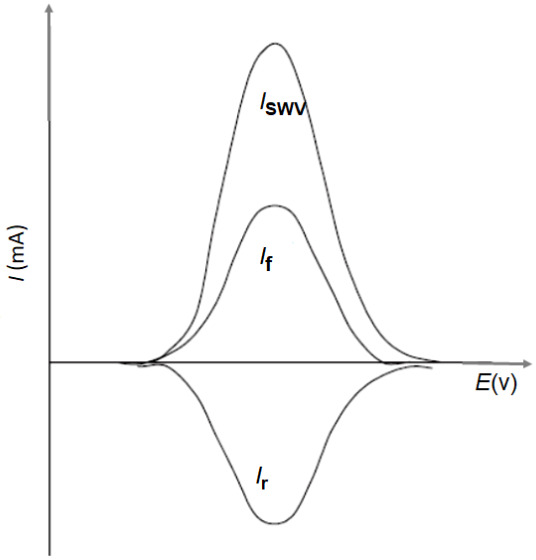

Figure 1.13 A voltammogram of SWV with the peak shape result obtained by $I = I_f - I_r$ (Westbroek, 2005).

1.7 SECM Probe Fabrication

1.7.1 Pt Microelectrode Fabrication

In this section, the preparation process used in this thesis for the Pt microelectrode and ultramicroelectrode used as the backbone of the Pt/alloy probe is detailed. Two different processes are employed for fabricating the microelectrodes and ultramicroelectrodes.

1.7.1.1 Instrument and Chemical

Soda-lime glass capillaries (75 ± 0.5 mm; o.d.,1.0 ± 0.05 mm; i.d.) and borosilicate capillaries (75 mm; o.d., 2.0 mm; i.d., 1.16 mm) were purchased from Hilgenberg GmbH (Malsfeld, Germany) and Pt wire (25 μm diameter, 99.99% purity) was purchased from Goodfellow (Huntingdon, England). Silver epoxy from EPO-TEK, Epoxy Technology (Billerica, USA). Copper wire (0.50 mm diameter), and gold connector pins were purchased from HEKA Electronic. Polishing discs (4000 grit) were obtained from Struers (Cleveland, USA).

Preparation of the micropipette was performed using P-2000 micropipette puller (Sutter Instrument of USA). For sealing Pt to the capillary the PC-10-CA vertical pipette puller was used (Narishige of Japan). Electrochemical measurements were performed using an Electrochemical Probe Scanner 3 (Heka Elektronik, Lambrecht, Germany) inside an argon-filled glovebox (O_2 < 1ppm, H_2O < 1.5 ppm; MBraun, Stratham, USA).

Lithium perchlorate, mercury (II) chloride, methylviologen dichloride (MV), was purchased from Sigma-Aldrich (Oakville, Canada) and Propylene Carbonate (PC), hexaminеruthenium (III) chloride was ordered from Strem Chem. (Newburyport, USA), and mercury (I) nitrate from Acros Organics (New Jersey, USA). Metallic Ga was acquired from Fisher scientific (Toronto, Canada). Silver wire for the Ag_xO quasi-reference counter electrode (QRCE; 1 mm diameter, 99.99% purity) was obtained from Goodfellow, (Huntingdon, England).

1.7.1.2 Fabrication Steps

Pt disk microelectrodes were prepared using a previously reported protocol (Danis, Polcari, et al., 2015). A soda-lime glass capillary was first rinsed with nanopure water and dried. It was then pulled using the P2000 to create two symmetric tips using a

single line heating and pulling program (Heat: 240; Fil: 5; Vel: 60; Del: 140; Pul: 70). A 2 cm piece of 25 μm diameter Pt wire was inserted to the tip of each micropipette. The wire was sealed under vacuum to minimize the chance of a trapped air bubble by reducing the inner pressure during a 10 second heating step. The Pt sealed wire was electrically connected to a copper wire using conductive silver epoxy. This was cured for half an hour in an oven at 120 °C. A larger borosilicate glass capillary was used to support the Cu wire extending from the smaller pulled pipette and an Au coated pin was soldered to the end of the microelectrode.

Without a uniform electroactive area, the current response of the microelectrode does not demonstrate the theoretical sigmoidal current. To ensure the desired geometry, the tip was exposed to a variable speed grinder/polisher. Figure 1.14.A shows a schematic of the disk polishing machine with a rotating motor. Figure 1.14.B demonstrates the polishing set up with two different types of polishing paper. For polishing the soda-lime glass sheath, alumina polishing paper (4000 grit) was used, and for the quartz pipettes diamond or alumina coated papers (800 and 1200 grit). At the end of polishing, the glass sheath should be uniformly sealed surround the Pt wire and the electroactive area should contain minimal roughness. If the force of the polishing was too excessive cracking would appear at the tip. To clean and remove all excess polishing material from the electrode tip after polishing, the electrodes were rinsed with deionized (DI) water (18.2 MΩ cm) and 70% ethanol before use.

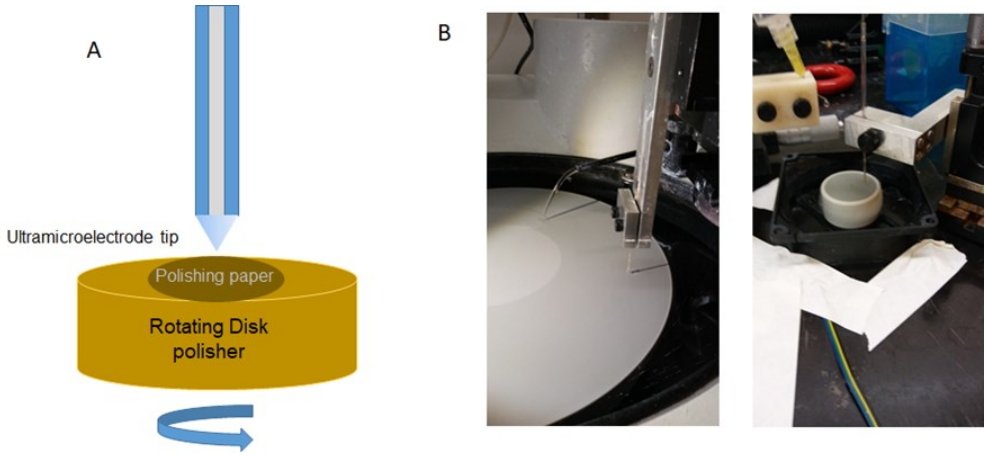

Figure 1.14 Scheme of microelectrode tip polishing using rotating disk polisher. B) ultramicroelectrode tip polishing using diamond coated polishing paper (left) and alumina coated paper (right) (photos were taken in the "laboratory for electrochemical reactive imaging and detection of biological systems" of Professor Mauzeroll at McGill university).

Pt ultramicroelectrodes were fabricated using an established procedure (Mezour et al., 2011). In this protocol the pulling and sealing steps of the micropipettes were performed simultaneously. Instead of pulling a soda-lime glass capillary into two symmetric pipettes in the first step, a 2 cm long section of Pt wire (25 µm diameter) was connected to a copper wire using conductive silver epoxy and subsequently cured. The attached wire was then inserted into the middle of quartz capillaries and similar to the previous protocol vacuum connections were made on both ends of the capillary. In the pulling step for preparing a smaller *RG* UME, an extra-thinning procedure was applied to the capillary with Pt wire, which heats, stretches, and cools the pipette using the single-line program (Heat: 540, Filament: 5, Velocity: 60, Delay: 140, Pull: 0). Two stoppers restrict the range of the puller bars so that the Pt is effectively sealed inside the capillary as the capillary is pulled longitudinally in the opposing directions. The heating from the laser beam with the pulling program together creates a tensile stress on the capillary for 40 seconds and was followed by 20 seconds of cooling, which was repeated five times. Over the duration of the cycles, the capillaries gradually elongate.

Subsequently the stoppers are removed and using a program in puller (Heat: 780, Filament: 12, Velocity: 160, Delay: 100, Pull: 200) breaks into two thin tips. Figure 1.15 shows the optical micrograph of the Pt UME at 20X magnification.

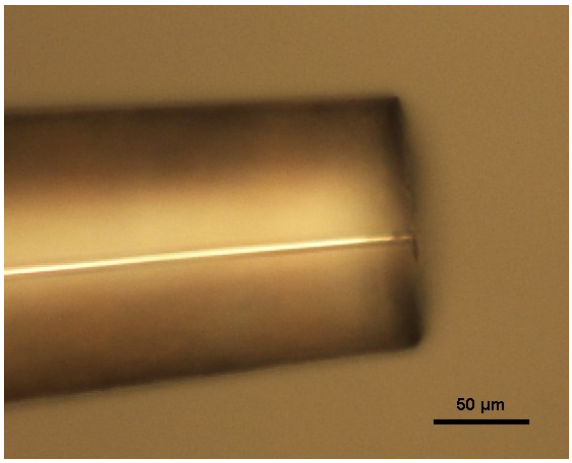

Figure 1.15 Optical micrograph of a Pt UME

1.1.2 A Brief Discussion on Capillary Thinning During Pulling Procedure

A state of the art account of this subject is given in the literature (Mezour et al., 2011). Briefly, during the heating and pulling steps of the outer layer of the capillary a temperature gradient is created within the capillary that causes viscosity to vary between inner and outer quartz layers. Eventually the temperature of the outer layer reaches approximately 1700°C, which is the softening temperature of the quartz and the tensile force remaining in the inner layer generates the elongated capillary (Mezour et al., 2011). Because the temperature of the quartz deformation is high, the capillary is not broken during the different steps of the pulling protocol. This makes the choice

of quartz capillaries critical to tolerating the sequential heating and pulling programs in this fabrication protocol.

1.7.2 Pt/Hg Microelectrode Fabrication (Outside Glovebox)

The potential of -500 mV vs. Hg/Hg_2SO_4 (Sat. K_2SO_4) was applied for 300 s to the Pt microelectrode in the aqueous solution of $Hg_2(NO_3)$ that was 0.5% acidified with HNO_3 (Danis, Gateman, et al., 2015; Mauzeroll, 2007a). Figure 1.16.A shows the recorded chronoamperogram for the Hg cap formation. Three main steps are indicated in the chronoamp. To further prove Hg hemisphere formation, CVs of the microelectrode of Pt and Pt/Hg were recorded in aqueous solutions of 1 mM of $[Ru\ (NH_3)_6]^{+3}$. The current changes between the Pt/Hg (purple trace) and Pt (green trace) clearly shows the increasing electroactive area resulting from the formation of the Hg droplet (Figure 1.16.B) (Danis, Gateman, et al., 2015).

Once the Pt/Hg microelectrode was formed, and the droplet of Hg was firmly attached to the Pt surface, the Hg cap can withstand washing. However, it should be stored in a degassed KNO_3 solution. Storage in the air can risk altering the surface area of the mercury as it potentially exposes Pt to air which changes the surface tension (Mauzeroll, 2007a).

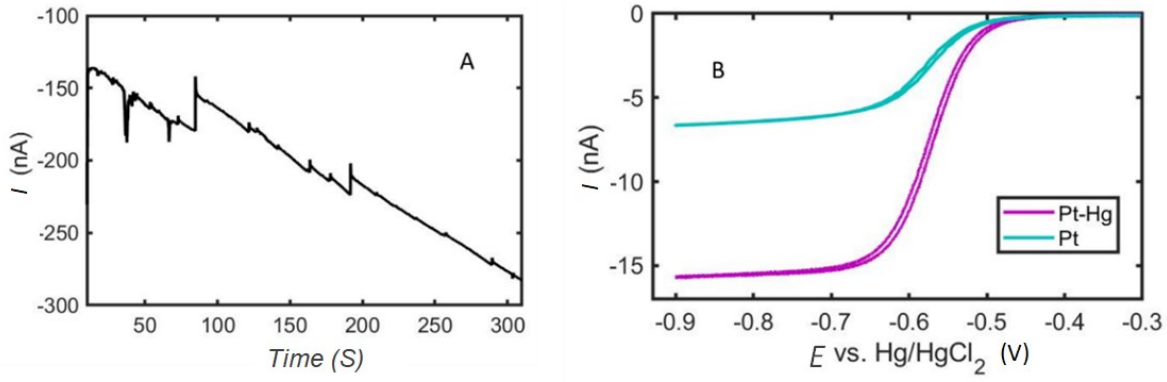

Figure 1.16 A) Current response of the Hg deposition on the tip of Pt microelectrode. A potential of -500 mV vs. Hg/Hg_2SO_4 was applied for 300 s to the Pt microelectrode immersed in aqua solution of $Hg_2(NO_3)$ in 0.1 M KNO_3. Counter electrode was Pt wire. The first few seconds (around 5 s) is the formation of Hg layer on the Pt surface. The fluctuations in the curve in the first 80 seconds is the spontaneous nucleation of Hg. The current diminishing around 80 seconds is because of the decreasing in the surface of the Hg nuclease as a result of nuclei coalescence, finally, the last part of the curve (from 180 s) the smooth part of the curve representative of the complete formation of the hemisphere) CV before (green line) and after Hg deposition (purple line) (solution: 1 mM $Ru(NH_3)_6Cl_3$ in 0.1 M 0.1 KNO_3, RE: $Hg/HgCl_2$, CE: Pt wire. Scan rage: -0.3 to -0.9 and scan rate: 0.025 V s^{-1}).

Once the Pt/Hg microelectrode is fabricated, it can be used for several experiments. However, the surface should be clean of trace contaminants from previous detection experiments. In the manganese ion detection experiment (see chapter 2), it was possible to perform more than 60 CVs without changes to the Hg hemisphere properties. If the Hg droplet is removed from the Pt and exposes Pt surface, electrochemical deposition of Hg is necessary to form a new Hg hemisphere.

Further attempts at Pt/Hg fabrication revealed that since all the experiments on battery materials were performed inside the glovebox, it is more reliable to produce and store these microelectrodes inside the glovebox. The Pt/Hg microelectrode fabrication and all experiments related to battery materials were performed inside a glovebox which will be fully detailed in chapter 2.

CHAPITRE II

SQUARE WAVE ANODIC STRIPPING VOLTAMMETRY FOR LOCALIZED DETECTION OF Mn^{2+} IN LI-ION BATTERY ENVIRONMENTS

In recent years, the use of manganese in positive LIB electrode materials, like manganese oxides (LMO or spinel-$Li_xMn_2O_4$), has seen increased interest. Manganese containing batteries provide some fundamental advantages like lower cost and less toxicity in comparison with e.g. $LiCoO_2$. In comparison to other battery compounds, cobalt containing cathode materials are the most expensive ones. As Mn is approximately ten times cheaper than Co, this feature makes it one of the important candidates for use in the battery of electric vehicles (EV) in which cost is one of the vital factors for consideration (Ahmed et al., 2017; Nitta et al., 2015). Despite all of these fundamental advantages, batteries containing *spinel*-$LiMn_2O_4$ cathode materials (LMO), experience severe capacity fading on charge–discharge cycling, and one possible explanation for this poor capacity retention is the dissolution of manganese into the electrolyte. This chapter explains preparation of a micro probe that can detect the concentration of the manganese ions locally with high resolution that would be a strong tool to resolve the dissolution problem. Therefore, the main goal of this chapter is *proposing* a technique for a local detection of Mn^{2+} at the interface of solid/ solution in lithium-ion battery materials.

This chapter has been published as a research article in *J. Electrochem. Soc.* 2022, **169,** 040526.

Mojgan Hatami, David Polcari, Md Sazzad Hossain, Mohammadreza Z. Ghavidel, Prof. Janine Mauzeroll, and Prof. Steen Schougaard are co-authors of this article. The supporting information for this article can be found in Appendix A.

The contributions of the authors of the article are as listed below:

• Mojgan Hatami: Design of experiments, experimentation, data analysis, figures.

• David Polcari: Experimentation, design of experiments.

• Md Sazzad Hossain: Figures.

• Mohammadreza Z. Ghavidel: Discussion, experimental set up design.

• Prof. Janine Mauzeroll: Discussion, manuscript editing.

• Prof. Steen Schougaard: Supervision, manuscript editing.

2.1 Abstract

Li ion batteries that incorporate manganese present several advantages, including low cost and low toxicity. However, these batteries often suffer from dissolution of manganese into the electrolyte solution, severely impeding battery performance. This work describes the quantitative detection of Mn^{2+} ions in battery relevant environment i.e. non-aqueous electrolyte within an inert atmosphere. To this end, an electrochemical probe was fabricated using electrochemical deposition of a Hg cap onto a 25 µm Pt disk microelectrode. The Pt/Hg microelectrode was fully characterized by optical microscopy, cyclic voltammetry, scanning electrochemical microscopy. Using square wave anodic absorption voltammetry to overcome reproducibility issues with classical linear sweep anodic stripping voltammetry, Mn^{2+} was quantified in non-aqueous solution with a limit of detection of 14 µM. Finally, using this detection scheme, the trapping ability of aza-15-crown-5 ether and dilithium iminodiacetate was invested.

2.2 Introduction

Li-ion batteries are one of the most impressive industrial success stories of the last few decades. After an extensive research effort, Li-ion batteries have found widespread use in commercial products, including portable electronic devices and electric vehicles (Etacheri et al., 2011; Chen et al., 2022; Li et al., 2021; Chen & Zhao, 2020). Arguably, their success can be attributed to their high energy density and long lifespan (Diouf & Pode, 2015, Shi et al., 2021).

A newer generation of batteries has been developed based on the positive electrode that employs manganese rather than cobalt. These electrodes provide a wide range of advantages, incl. lower cost, toxicity and improved safety (Danis, Gateman, et al., 2015;

Nitta et al., 2015; Schmuch et al., 2018). However, batteries based on the *spinel*-$LiMn_2O_4$ (LMO) or $LiM_{0.5}Mn_{1.5}O_4$ (M can be a transition metal such as Ni) have not found widespread use (Liang, R. f. et al., 2008; Liu et al., 2013; Saulnier et al., 2016; Yang, S. et al., 2003) in part due to manganese dissolution into the electrolyte that causes active materials degradation. One possible explanation for the manganese leaching from the spinel cathode materials is the disproportionation reaction of Mn^{3+} ions for producing Mn^{2+} and Mn^{4+} due to the Jahn-Teller lattice distortion effect (Thackeray et al., 1983) In addition, the dissolved manganese may deposit on the anode electrode and result in decreasing power capacity, and overall battery life (Banerjee et al., 2017; Danis, Gateman, et al., 2015). A strong tool to study this problem in detail would be a local probe with low detection limit for quantitative measurement.

In this report, Anodic stripping voltammetry (ASV) with two different method of potential sweeping, linear sweep (LS) and square wave form sweep (SW), were utilized for Mn^{2+} detection and compared in result and discussion section. These two methods are demonstrated as LS-ASV (linear sweep anodic stripping voltammetry) and SW-ASV (square wave anodic stripping voltammetry) in this article.

Anodic stripping voltammetry (ASV) is a well-established technique for the electrochemical detection of metals in aqueous solution (Daniele, Salvatore et al., 1989; Daniele, Salvatore et al., 2008). This technique involves detection of metals using a mercury electrode. Recently, mercury-capped microelectrodes have been used in combination with scanning electrochemical microscopy (SECM) to provide localized metal ion detection (Barton & Rodríguez-López, 2014; Brendel & Luther, 1995; Daniele, Salvatore et al., 2003; Panascikaite & Armalis, 2011; Rudolph et al., 2004; Souto et al., 2012; Xu, K. M. & Si, 2007). In order to be relevant for battery materials, the electrochemical detection of manganese must be performed in an organic solution within inert atmosphere.

Herein, the fabrication and characterization of a Pt/Hg microelectrode in an inert atmosphere (i.e. glovebox) is demonstrated. Using this probe in combination with pulse voltammetry techniques, the concentration of Mn^{2+} ions in battery-relevant solvent (propylene carbonate or PC) was quantified. Finally, using this detection scheme, the Mn^{2+} trapping ability of aza-15-crown-5 ether (A15C5) and dilithium iminodiacetate (Li_2IDA) was investigated.

2.3 Experimental

2.3.1 Chemicals and Instruments

Lithium perchlorate, mercury (II) chloride, methylviologen dichloride (MV), and manganese (II) chloride were purchased from Sigma-Aldrich (Oakville, Canada). Propylene carbonate (PC) was purchased from Gotion (Fremont, USA). Polymeric Aza-15-crown-5 ether (3% cross-linked divinylbenzene vinylbenzyl-aza-15-crown-5) (A15C5) and dilithium iminidiacetate (Li_2IDA) were graciously donated by General Motors Company.

Electrochemical measurements were performed using an Electrochemical Probe Scanner 3 (Heka Elektronik, Lambrecht, Germany) inside an argon-filled glovebox (O_2 < 1ppm, H_2O < 1.5 ppm; MBraun, Stratham, USA). Unless mentioned otherwise, all measurements were performed in PC solvent containing 0.2 M $LiClO_4$ as supporting electrolyte and an Ag_xO quasi-reference counter electrode (QRCE; 1 mm diameter, 99.99% purity; Goodfellow, Huntingdon, England).

2.3.2 Fabrication and Characterization of Pt/Hg Microelectrodes

Pt disk microelectrodes were prepared using a previously reported protocol (Danis, Polcari, et al., 2015). Briefly, a soda-lime glass capillary was pulled using a P-2000 micropipette puller (Sutter Instrument Company, Novato, USA) and a Pt wire (25 μm diameter, 99.99% purity; Good fellow) was inserted. The tip of the capillary was sealed under vacuum inside a heating coil, and electrically connected to a copper wire using silver epoxy. A larger borosilicate glass capillary and Au coated pin were added to complete the assembly. Microelectrodes were mechanically polished and rinsed with deionized (DI) water (18.2 MΩ cm) and 70% ethanol before use.

The electrochemical performance of Pt microelectrodes was characterized using cyclic voltammetry (CV), where a microelectrode was immersed in an aqueous solution of 1 mM FcMeOH and the potential was cycled from -100 to 400 mV vs. Ag/AgCl. Furthermore, SECM approach curves were used to determine the RG of the microelectrodes, defined as the ratio of the insulating glass sheath to the Pt core. Microelectrodes were approached towards an insulating poly-chlorotrifluoroethylene (CTFE) surface at a speed of 0.5 μm s^{-1} and the RG value was extracted using analytical expressions from literature (Lefrou & Cornut, 2010).

The deposition of a Hg hemisphere onto the Pt disk microelectrode was performed electrochemically inside the argon-filled glovebox. The microelectrode was immersed in a solution of 10 mM $HgCl_2$ in PC. A potential of -800 mV vs. Ag QRE was applied for 300 s, resulting in the formation of a Hg hemisphere on the tip of the Pt microelectrode. The performance of the Pt/Hg microelectrode was also characterized using CV of 1 mM MV^{2+} in PC.

2.3.3 Manganese Detection

Detection of Mn^{2+} was performed inside a glovebox with a Pt/Hg microelectrode using LS-ASV or SW-ASV. Standard solutions of Mn^{2+} with different concentrations (0.1 to 1 mM) were prepared from $MnCl_2$, and 0.2 M $LiClO_4$ in PC supporting electrolyte. For SWV experiments, the square wave amplitude was 10 mV, the scan frequency was 25 Hz, and the base increment was 2 mV. For the LS-ASV experiment two different protocols were used: For LS-ASV experiments using a Li/Li^+ QRCE. The potential was swept in the 2.5-1.5 V range with a scan rate of 250 mV s^{-1}. The deposition of manganese started around the 1.9 V, whereas stripping occurred around 1.75 to 2.3V vs. Li/Li^+., while for LS-ASV using an Ag QRCE, the potential range was –1.6 to –0.6 V with a scan rate of 50 mV s^{-1}. There was not extra time interval for metal absorption in this method.

In the SW-ASV experiment, was the potential swept from -1.6 to -0.8 V and the manganese absorption started from -1.6 V as soon as applying negative potential. The metal absorption continued close to the -1.28 V with demonstrating a cathodic current in the microelectrode (Figure 2.1.A) and the manganese stripping step was in the potential range approximately between -1.28 to -1.15 with a anodic current of microelectrode

2.3.4 Manganese Trapping

The Mn^{2+} trapping ability of two different agents, A15C5 and Li_2IDA, was evaluated using 1 mM Mn^{2+} solution. In each case, a quantified amount of the agent was added to the Mn^{2+} solution to make a suspension. After each addition, the solution was stirred for 2 min before recording the SWV response. After recording the voltammogram of Mn^{2+}, the microelectrodes were tested using 1 mM fresh solution of Mn^{2+}. The

observed current corresponded consistently to the calibration curve (Figure 2.2.B), confirming a clean surface without fouling from the trapping materials.

2.3.5 Statistical Analysis

Peak heights were used to preparation of the calibration curve and for each concentration the background current was extrapolated from -0.9 to -1.1 V range and subtracted from the height of the peak. Confidence intervals were obtained from Student-t statics at the 95% confidence level by using three observations for each reported value. The limit of detection (LOD) was calculated according to the formula, LOD = 3* (Sy)/S = 3* (Standard deviation of the responses)/ slope of the calibration curve (Long & Winefordner, 1983).

2.4 Result and Discussion

2.4.1 Microelectrode Characterization

Previous reports have demonstrated the deposition of a Hg hemisphere onto a Pt microelectrode using chronoamperometry in aqueous solution (Danis, Gateman, et al., 2015; Danis, Polcari, et al., 2015; Mauzeroll et al., 2003). However, considering the need to perform measurements in an inert atmosphere and to minimize possible microelectrode tip damage, the chronoamperometric deposition was performed directly inside a glovebox from $HgCl_2$ in PC (Figure A.2). The current spikes in Figure A.2 were caused by the nucleation of Hg droplets on the Pt electrode. To confirm the presence of a Hg hemisphere, CVs were recorded before and after deposition. For this

purpose, methylviologen (MV^{2+}) was used due to the stability potential window of Pt/Hg electrode. As shown in Figure 2.1.A, the diffusion-limited current significantly increased after deposition, demonstrating that the Hg hemisphere had been successfully deposited, thereby increasing the electroactive surface area and geometry of the microelectrode. Furthermore, during initial testing, the glovebox deposition protocol was verified using optical microscopy, i.e. the microelectrode was removed from the glovebox and imaged using an inverted microscope at 40X magnification. A Hg hemisphere is clearly visible following the deposition process (Figure 2.1.B).

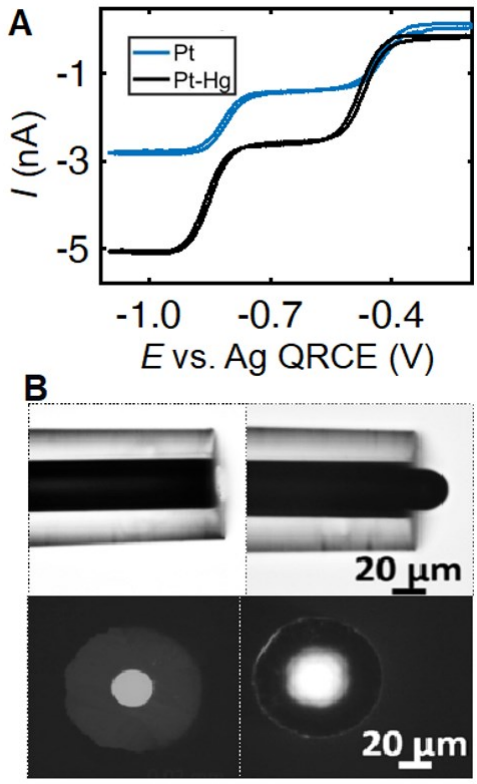

Figure 2.1 Characterization of Pt and Pt/Hg microelectrodes. CV before and after Hg deposition (solution: 1 mM MV^{2+} in 0.2 M $LiClO_4$ in PC, scan range: -1.1 to -0.2 V, scan rate: 25 mV s^{-1}) (A). Side and top view optical micrographs of the microelectrode before (left panel) and after (right panel) Hg deposition (B).

2.4.2 Detection of Mn^{2+}

The response of the Pt/Hg microelectrode towards Mn^{2+} was obtained using SWV (Figure 2.2.A). The anodic current response (e.g. peak height) increased linearly with the concentration of Mn^{2+}, producing a regression coefficient (R^2) of 0.996 (Figure 2.2.B. The sensitivity (i.e. the slope of the regression line), was 6.17 nA mM^{-1} (with the estimated standard deviation (e.s.d.) 0.03) and the limit of detection (LOD) was 14 µM.

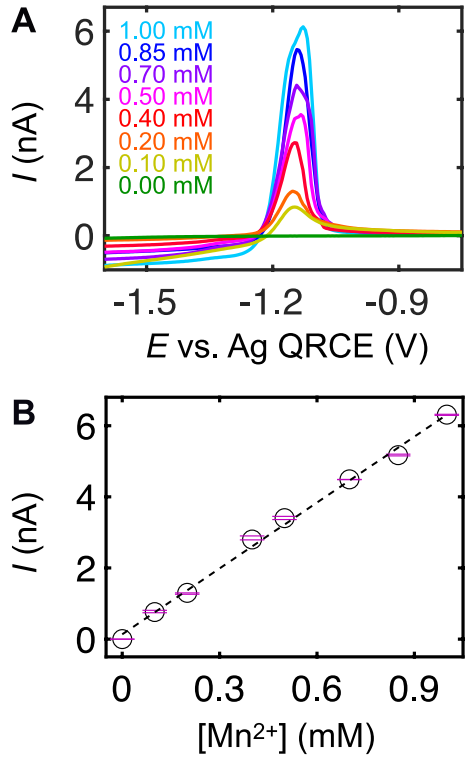

Figure 2.2 Detection of Mn^{2+} using Pt/Hg microelectrode. SWV response towards standard solutions of Mn^{2+} (0.1–1 mM) (A). Calibration curve extracted from peak heights in A (I (nA) = 6.17 [Mn^{2+}] + 0.132) (B).

2.4.3 Mn^{2+} Detection: LS-ASV vs. SW-ASV

As mentioned in the introduction, both ASV and SWV have found widespread use for the electrochemical detection of metals in aqueous solution. However, literature pertaining to the electrochemical detection of manganese is extremely scarce, with only a handful of reports available. (Daniele, Salvatore et al., 2008; Panascikaite & Armalis, 2011) Moreover, these techniques appear to not previously have been used to detect manganese in non-aqueous media. Using a similar approach as previous section for Mn^{2+} detection using SW-ASV, the LS-ASV response of a Pt/Hg microelectrode in standard solutions of Mn^{2+} were measured.

Using a similar approach as section 2.3.3, the ASV response of a Pt/Hg microelectrode in standard solutions of Mn^{2+} was measured (Figure 2.3). In this case, two different reference electrodes were used, namely Li/Li^{+} (Figure 2.3) and Ag QRE (Figure A.3). The limit of detection achievable using ASV, 330 μM, was inferior to that of SW-ASV. Furthermore, the electrochemical response was less reproducible, as the peak position shifts with each subsequent CV, regardless of the reference electrode used (Ag QRE or Li/Li^{+}). While less severe compared to nickel and cobalt, previous reports suggest that ASV detection of Mn^{2+} is difficult due to the sluggish kinetics electron transfer and the manganese low solubility in mercury (Coetzee & Ecoff, 1991). Because of the above-mentioned problems, SWV-ASV was used as the method of choice for electrochemical detection of Mn^{2+} using a Pt/Hg microelectrode. It is important to note that the based on the illustration about the SWV in the first chapter of this thesis (1.6) the potential is swept direct and reverse, and the current sampling is at the end of each potential pulse. It means that, the current of oxidation and reduction of species are recorded and the final current which is the subtraction of mentioned currents, has minimum portion of charging current. As a result of eliminating charging current technique is more sensitive and provides the lower limit of detection.

It should be mentioned that in principle it would be possible to add a preconcentration step to the stripping voltammetry, or to decrease the sweep rate of the deposition scan. By extending the time of the absorption of the analyte, the concentration of the absorbed manganese onto the mercury will be higher, therefore, the height of the obtained peak will be enhanced. As a result, the slope of the calibration curve and the sensitivity will be increased.

One important feature of the investigation of the Mn^{2+} concentration in the this chapter is that the concentration range in the calibration curve is applicable in a real battery material. The released Mn^{2+} in a *spinel* battery material after 100 cycles is in the range of 0.5 to 1 mM for [Mn^{2+}] (Banerjee, et al., 2017). So, the proposed technique can be used to detect the local concentration of Mn^{2+} at the interface of the electrode/ electrolyte in lithium ion battery material.

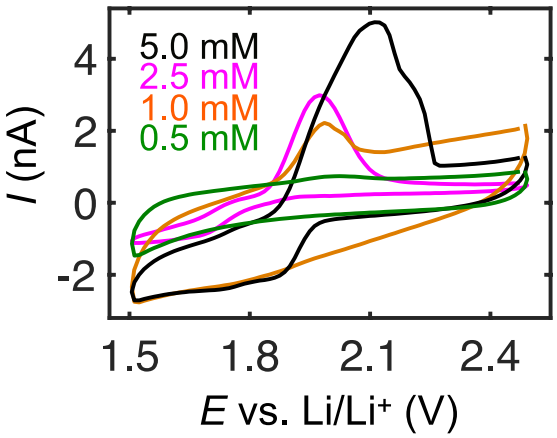

Figure 2.3 Detection of Mn^{2+} using ASV. Electrochemical response at a Pt/Hg microelectrode in standard solutions of $MnCl_2$ (0.5–5 mM) (Electrolyte: 0.2 M $LiClO_4$ in PC) RF: Li/Li^+ scan rate: 250 mV s^{-1}. Each of the consecutive points in these current profiles represents an average of five current values.

2.4.4 Manganese Trapping

In order to mitigate the negative effects of manganese dissolution during battery discharging/charging, one possible strategy is to use agents to trap free manganese ions in solution. As such, two agents known to efficiently trap Mn^{2+}, A15C5 (Blair et al., 2000; Inokuchi et al., 2012) and Li_2IDA (Asanuma & Toshima, 2000; Moyna et al., 2013; Razak et al., 2018), were investigated using a freshly characterized Pt/Hg microelectrode and SWV.

Using the previously obtained calibration (Figure 2.2.B), the amount of free Mn^{2+} present after addition of A15C5 to a 1 mM Mn^{2+} solution was examined (Figure 2.4.C). Up to an added A15C5 concentration of 1.6 g L^{-1} the amount of free Mn^{2+} decreased, hereafter no free Mn^{2+} could be detected by SWV confirming the A15C5 ability to effectively trap Mn^{2+}.

Similar to A15C5, the addition of Li_2IDA to a 1 mM Mn^{2+} solution decreased the amount of free Mn^{2+} (Figure 2.4.D) so that after addition of 1.8 g L^{-1} of Li_2IDA, the free amount decreases below the limit of detection.

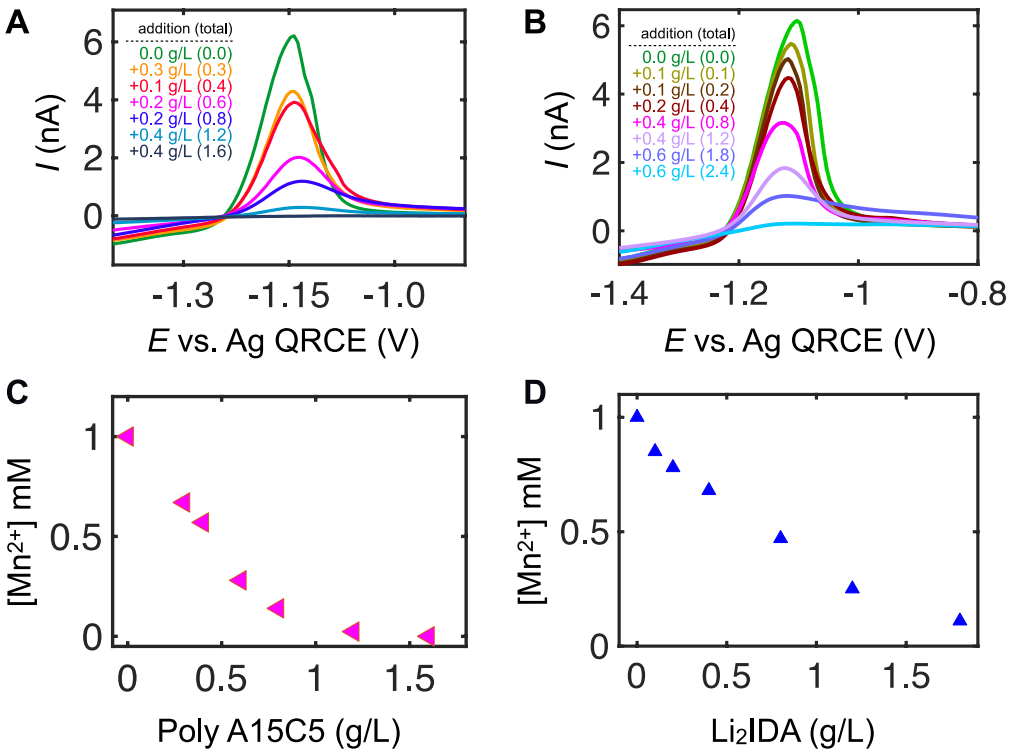

Figure 2.4 Mn^{2+} trapping by A15C5 (A,C) and Li_2IDA (B,D). SWV responses at the Pt/Hg microelectrode after successive addition of complexing agent (A,B) to the 1 mM $MnCl_2$ solution (peak amplitude: 10 mV, scan frequency: 25 Hz, base increment: 2 mV). Added amount between each curve, as well as the cumulative amount (in parentheses) is indicated. The concentration of free Mn^{2+} after complexing agent addition (C,D).

In addition to initial trapping of Mn^{2+}, the stability of the complex is important. The SWV Mn^{2+} response of a single concentration of A15C5 (1g L^{-1}) vs. time (Figure 2.5.A, Figure 2.5.C) remained stable within the experimental quantitative error, showing the stability of the complex as well at the rapid (<2min) equilibration of the system.

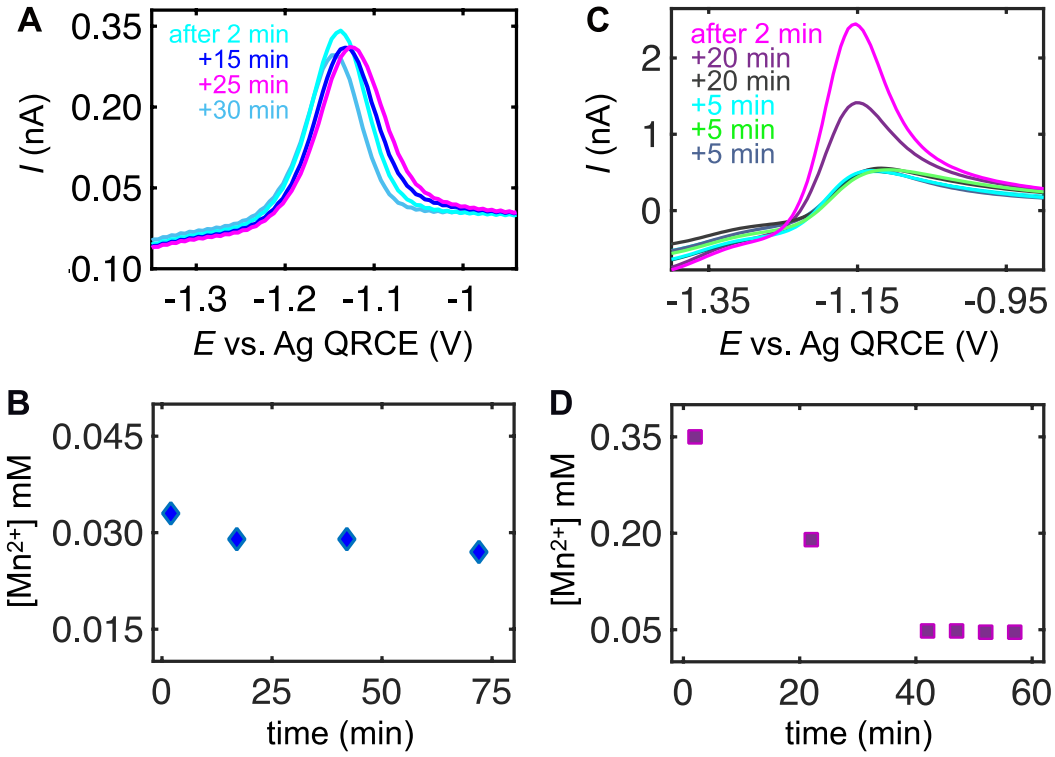

Figure 2.5 Effect of time on manganese trapping using A15C5 (A,B 1g L^{-1}) and Li_2IDA (C,D, 0.9 g L^{-1}). (A, C) SWV of 1 mM Mn^{2+} initial concentration recorded as a function of time (peak amplitude: 15 mV, scan frequency: 25 Hz, base increment: 2 mV). (B,D) Corresponding Mn^{2+} concentrations at each time point.

The kinetics of Mn^{2+} trapping was also determined for Li_2IDA. Examining the current originating from 1 mM of Mn^{2+} combined with 0.9 g. L^{-1} Li_2IDA, indicate that Li_2IDA trap more Mn^{2+} as the exposure time is extended (Figure 2.5.B, Figure 2.5.C). Eventually the concentration of Mn^{2+} in the solution decreases to 0.04 mM and remains constant.

2.5 Conclusion

To summarize, in this study Mn^{2+} species were quantitatively detected in an environment suited for battery study using a Pt/Hg microelectrode. Comparing LS-ASV and SW-ASV, the latter emerged as the more appropriate technique, primarily because of improved reproducibility with a 14μM limit of detection, i.e. more than 20 times lower than that of LS-ASV (330 μM). Hence, this study establishes SW-ASV as a powerful voltammetric method for electrochemical Mn^{+2} detection.

Using this technique, electrochemical responses due to the presence of Mn^{2+} in two different solutions each containing two different trapping agents (aza crown ether (A15C5) and Li_2IDA) were recorded. The results establish the suitability of Hg/Pt microelectrode as a probe for Mn^{2+} detection also in complexing media, having shown no fouling during SWV from the employed trapping materials in solution. The methodology presented herein could be used in combination with SECM, thereby providing spatial resolution in addition to quantitative detection. As such, manganese release from hot spots on the Li-ion battery electrodes should become identifiable, yielding an unprecedented analytical ability for the study of *spinel*-$LiMn_2O_4$ and of similar materials.

2.6 Acknowledgments

The authors are grateful for financial support of the work by General Motors and the Natural Sciences and Engineering Research Council of Canada (CRDPJ 494074-16) as well as the fruitful commentary and support of Dr. Ion Halalay.

CHAPITRE III

PT/GA MICROELECTRODE FOR LITHIUM ION STRIPPING VOLTAMMETRY

Since lithium-ion exchange in lithium-ion battery cycling, is a critical part of the battery operation, the quantification of Li^+ provides important information about electrolyte mass transport at the interface of the electrode and solution. In this chapter, the goal is to develop a technique for detecting the quantity of Li^+ in the electrolyte of the battery, which passes through the porous network of the cathode material. In this chapter the method will be introduced and used in the electrolyte of the battery and subsequently the mentioned method will be used in solid-state battery materials for local detection of Li^+. Scanning electrochemical microscopy (SECM) is a powerful technique for local detection and can be considered as a Li^+ quantification tool. Here in this chapter, an easy methodology for fabrication of a Pt/Ga microelectrode as a potential SECM probe is explained.

This chapter is prepared for submission in the Journal of the Electrochemical Society.

Mojgan Hatami, Md Sazzad Hossain, Prof. Janine Mauzeroll, and Prof. Steen Schougaard are co-authors of this article.

The contributions of the authors of the article are as listed below:

• Mojgan Hatami: Design of experiments, experimentation, data analysis, figures

• Md Sazzad Hossain: Figures.

• Prof. Janine Mauzeroll: Discussion, manuscript editing.

• Prof. Steen Schougaard: Supervision, manuscript editing.

3.1 Abstract

Li-ion batteries operation relies on lithium-ion exchange between the cathode and anode. Consequently, lithium-ion detection is critical for quantification of reaction rate heterogeneity and electrolyte transport properties in porous electrode films and ultimately the battery performance. However, selective Li^+ ion quantification using local probes has proven difficult. In this work, a Ga capped Pt (Pt/Ga) ultramicroelectrode was employed to detect lithium ions in a nonaqueous battery electrolyte. To this end, square wave (SW) and linear sweep anodic stripping voltammetry (LS-ASV) were employed. Whereas LS-ASV showed peak shifting and high limit of detection, SW-ASV performed reliably yielding a linear response from 0.3-5.0 mM and a limit of detection of 77μM. As such, this probe and perturbation profile combination should be ideal for future scanning and/or local electrochemical probe studies of lithium-ion battery systems.

3.2 Introduction

In recent decades, rechargeable batteries have been used as power sources for many applications including electric vehicles (EV). Moreover, the battery is a key part of developing an EV that can meet the full range of consumer expectations. The most common kind of rechargeable battery are lithium-ion based due to their extensive applications in portable electronics where they have outperformed other technologies due to their high energy and power density (Lu et al., 2013; Poizot et al., 2000). Understanding transport properties of the electrolyte part of LIB is crucial to further improving high-power performance. In electric vehicles for instance, lithium transport through the electrolyte in porous electrodes is often the rate-limiting step (Etacheri & al., 2011; Wakihara, 2001; Wang & Cao, 2008). Therefore, having an electrochemical

tool for locally detecting of the quantity of lithium ions in the bulk of electrolyte solution or at the interface of electrodes/electrolyte is highly desirable.

Scanning Electrochemical Microscopy (SECM) is extensively used for local probing and two-dimensional mapping of chemical species. However, since direct plating of lithium is not feasible due to organic/inorganic solid-liquid interface layer formation (or the interface of electrode/ electrolyte inside the lithium-ion battery) an alternative probe method is needed like Hg based ASV. Although the currently available electrodes show abundant potential for lithium detection on electrode surfaces (Barton & Rodríguez-López, 2014), these have been prone to fouling and other stability issues, limiting wide-spread use. To counter this situation herein we propose a Pt/Ga microelectrode system lithium detection in battery electrolytes. Importantly, Ga is liquid at room temperature (Creighton & Withnall, 2000), and produces a liquid alloy with up to 1.7 wt % Li before a solid Ga-Li solution begins to form (Saint et al., 2005; Xiang et al., 2017). This is in stark contrast to the Hg-Li amalgam, where according to the phase diagram (He et al., 2019), the liquid-solid boundary is below room temperature at low lithium concentrations but fall above room temperature even at modest lithium concentrations (Hg_3Li). Once the solid is formed stripping kinetics become slow causing a loss of fidelity. Consequently, Ga should be a viable candidate for lithium detection in battery electrodes. In comparison with Hg, Ga acts differently when forming an alloy with Pt. Although the Ga source which was used in the experiment was liquid at room temperature, it does not spontaneously reflow to change its shape and it can be in a metastable form in different shapes (even nonspherical shape) such as cone or filament (Chiechi *et al.*, 2008).

Moreover, we employ square wave voltammetry (SWV) as it has previously been shown to improve sensitivity in other stripping voltammetry systems (Chen Legrand et al., 2017; Kounaves, 1997; Mirceski et al., 2018).

3.3 Experimental

3.3.1 Materials and Chemicals

Lithium hexafluorophosphate ($LiPF_6$), and tetraethylammonium tetrafluoroborate ($TEABF_4$) were purchased from Gotion (Fremont, USA), propylene carbonate (PC) and N-methyl-pyrrolidone (NMP) anhydrous 99.5% from Sigma-Aldrich (Oakville, Canada). Metallic Ga was acquired from Fisher scientific (Toronto, Canada). Acetic acid (CH_3COOH) and hydrogen peroxide (H_2O_2,30%) were purchased from Fisher brand (Ontario, Canada), carbon coated lithium iron phosphate C-$LiFePO_4$ from Phostech Lithium Inc. (Quebec City, Canada), poly (vinylidene fluoride) (PVDF) from Foster Chemistry (Putnam,USA) , carbon (CS65) form Timcal (Cambridge, UK), and Al foil from Uline (Milton, USA). Silver wire for use as an Ag_xO quasi-reference counter electrode in ASV experiments, from Goodfellow (Huntingdon, England). (1 mm diameter, 99.99% purity)

3.3.2 $Li_{(1-x)}FePO_4$ Reference Electrode Fabrication

A custom $Li_{(1-x)}FePO_4$ wire was prepared to use as a reference electrode in the experiments. First C-$Li_{(1-x)}FePO_4$ powder was prepared using 1 g of C-$LiFePO_4$ mixed with 0.17 ml of glacial acetic acid and 0.10 ml of hydrogen peroxide. Following 24 hours of stirring the mixture was filtered, washed (with 300 ml of nanopure water) and then air-dried for 24 hours. The resulting powder along with PVDF and carbon were mixed at a mass ratio of 8:1:1 with 2.5 ml of NMP per gram of solid. After 24 hours of mixing (roller milling) the slurry was cast onto Al foil and then vacuum-dried to obtain the final film. The details of film preparation has been discussed in previous work

(Lepage et al., 2011). The potential of the prepared reference electrode was 3.34 V vs. Li.

3.3.3 Pt/Ga Microelectrode Fabrication and Characterization

The protocol for the fabrication of Pt ultramicroelectrode has been reported previously (Mezour et al., 2011). Briefly, a Pt wire (25 μm diameter, 99.99% purity; Goodfellow) was first connected to a piece of copper wire using conductive silver epoxy. The wire was then inserted into a quartz capillary. While applying vacuum at both ends, the capillary was then simultaneously laser-heated (on Pt) and pulled longitudinally in the opposite direction using a micropipette puller (P2000, Sutter Instrument, Novato, USA). Two stoppers restrict the range of the puller bars so that the Pt is effectively sealed inside the capillary. The step of heating was followed by cooling, and this step was applied 5 times gradually elongate the glass/Pt combination, which eventually broke into two electrodes. The Cu wire at the open end of the electrode was soldered to a Au-coated connector pin (Mezour et al., 2011). After washing (with deionized water and 70% ethanol), the finished electrodes were characterized by cyclic voltammetry (CV) in 1 mM aqueous solution of ferrocene methanol (FcMeOH). Based on the steady state current, the final electrode diameter was determined to be 1.1 μm (Danis, Polcari, et al., 2015). It should be mentioned that the protocol of the Pt microelectrode fabrication had several thinning steps that was illustrated in abstract of this thesis (1.7) as a result the final diameter of the Pt microelectrode is smaller than 25 μm. To facilitate Ga deposition, the electrode RG was increased by polishing on 3200 Grit paper (Buehler). This increased RG improves adhesion of the gallium cone at the tip of the electrode stabilizing Pt/Ga microelectrode system physically. For Ga deposition, the gallium metal was first heated (50 °C) and then inserted into a borosilicate capillary (inner/outer diameter: 0.50/1.0 mm) to act as the source. The tip of the microelectrode was then

directly inserted into the source capillary (the diameter of capillary is larger than that of the electrode). When the electrode was removed gallium covered the tip in the shape of a cone (Figure 3.1.A). Finally, the geometry on the electrode tip was determined under an optical microscope (Nikon Eclipse, 50i). Using the capillary tube with a certain inner diameter as the source of Ga is very helpful to preparing cone shape microelectrode and prevents to have random geometry in Pt/Ga microelectrode fabrication.

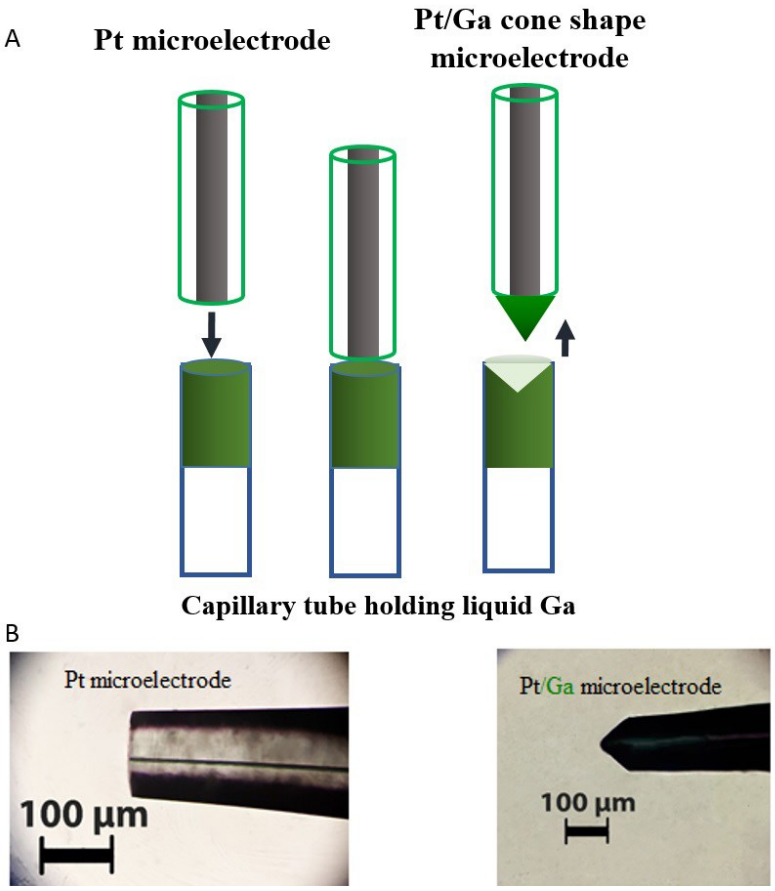

Figure 3.1 Scheme of Pt/Ga microelectrode fabrication (A). Optical micrograph of the Pt and Pt/Ga microelectrode (B).

3.3.4 Electrochemical Analysis

All solutions for electrochemical measurements were prepared inside an argon filled glovebox (O_2 <0.5 ppm H_2O <1.5 ppm; MBraun, Stratham, USA). Experiments were carried out using an Electrochemical Probe Scanner 3 (Heka Elektronik, Lambrecht, Germany). Voltammograms for the Pt/Ga microelectrode were recorded using SWV or ASV. In SWV using $Li_{(1-x)}FePO_4$ as reference and counter electrode, the square wave amplitude was 10 mV, scan frequency 25 Hz, and a base increment was 2 mV the potential swift from -2.8 to -2.1. In ASV experiments, using an Ag QRCE the potential range was -2.8 to -1.2V with the scan rate of 100 mVs^{-1}.

3.3.5 Statistical Analysis

The calibration curve was prepared using peak currents at each concentration, with the background current estimated by extrapolating the current in the -2.3 to -2.2 V range. Confidence intervals were obtained from Student-t statics at the 95% confidence level using three observations for each reported value. The limit of detection (LOD) was calculated according to the formula. LOD = 3* (Sy)/S = 3* (Standard deviation of the responses)/ slope of the calibration curve (Long & Winefordner, 1983).

3.4 Result and Discussion

3.4.1 Li^+ ion Detection Using LS-ASV

Initially CVs were performed to establish the extent of lithium insertion/desertion into the Ga cone. For LS-ASV, the potential was swept in the -0.4 V to -1.5 V range with a scan rate of 100 mV s^{-1}. The area of the ASV that has negative current shows the

deposition of the lithium and has the cathodic current, whereas, stripping of the lithium occurred around -2.4 to -1.6 V vs. Ag QRCE. These areas have the anodic current.

The overlapping current responses generated from nine successive cycles in 0.7 mM $LiPF_6$ solution (Figure 3.2.A) confirms lithium transport in and out of the Ga tip. In order to verify the electrode stability and current reproducibility for extended cycles, Li^+ concentration was detected in three different concentration solutions. Beginning with 1.0 mM the current responses were recorded three times, the concentration was raised to 3.0 mM, before returning to 1.0 mM, to evaluate the effect of the concentrated solution on electrode performance on recording the current response of 1.0 mM. Followed by reducing the concentration of the Li^+ solution to 0.8 mM and finally raising it back to 1.0 mM. Figure 3.2.B shows three sets of currents measured for solution of 1 mM after these concentration fluctuations. Following the up (3.0 mM) and downshifts (0.8 mM), the confidence interval for the recorded current was [44.7 49.3] at the 95% confidence level for 1 mM solution. It should be mentioned that there are cathodic current of lithium absorption for each ASV in Figure 3.2.B, even for the solution with 0.8 mM concentration, however, it is hard to see in one figure with the ASV of 3.0 mM solution. As such, the ASV of Figure 3.2.A shows the cathodic current of lithium absorption obviously.

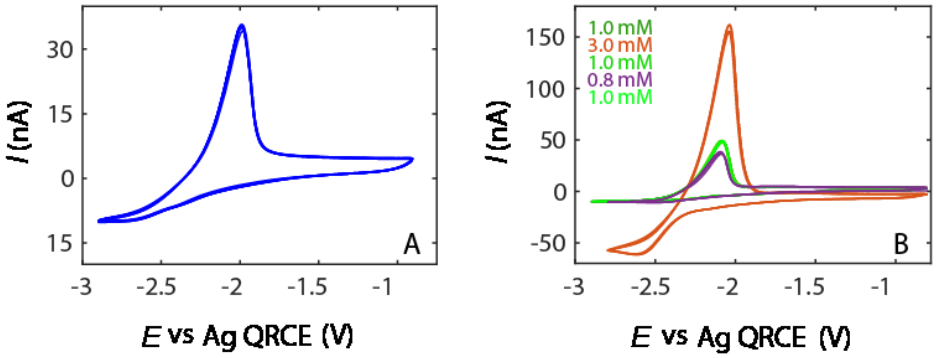

Figure 3.2 Stability of Li^+ detection via ASV at a Pt/Ga microelectrode in $LiPF_6$ solution (supporting electrolyte: 0.1 M $TEABF_4$, Ref: Ag QRCE, scan rate: 100 mV s^{-1}) (A). Nine overlapping CV cycles of 0.7 mM Li^+. Part (B) shows ASV responses for the same tip for the series indicated in the inset.

3.4.2 SWV Detection

Although consistent and stable at higher concentrations, ASV was found not to be reproducible below 0.7 mM lithium concentrations. Moreover, the potential of the peak appears to be shifting in a non-systematic way especially when low concentrations were employed. To overcome these issues, SWV, known for reducing contribution of the charging current (Chen Legrand et al., 2017; Kounaves, 1997; Mirceski et al., 2018) replaced linear sweep. Moreover, $Li_{(1-x)}FePO_4$ was used as a reference and counter electrode. Figure 3.3.A shows the anodic SWV responses for Li^+ concentrations ranging from 0 to 5 mM. Based on the peak current a calibration curve was generated, that show a linear response with concentration (Figure 3.3.B), with a regression coefficient (R^2) of 0.994, a sensitivity of 47.8 ± 2.8 nA mM^{-1} (slope of the calibration curve) and limit of detection (LOD) for the Li^+ ion detection experiment was 77 µM. The concentration range in the calibration curve is consistent with a real lithium-ion battery material (when subtracting the concentration of Li^+ electrolyte from the total

concentration). Although there are Li^+ containing battery electrolytes with high concentration (such as 1M), the calibration curve of this chapter provides information about the concentration of Li^+ that releases from the electrode material to the electrolyte and is applicable in a real lithium-ion battery.

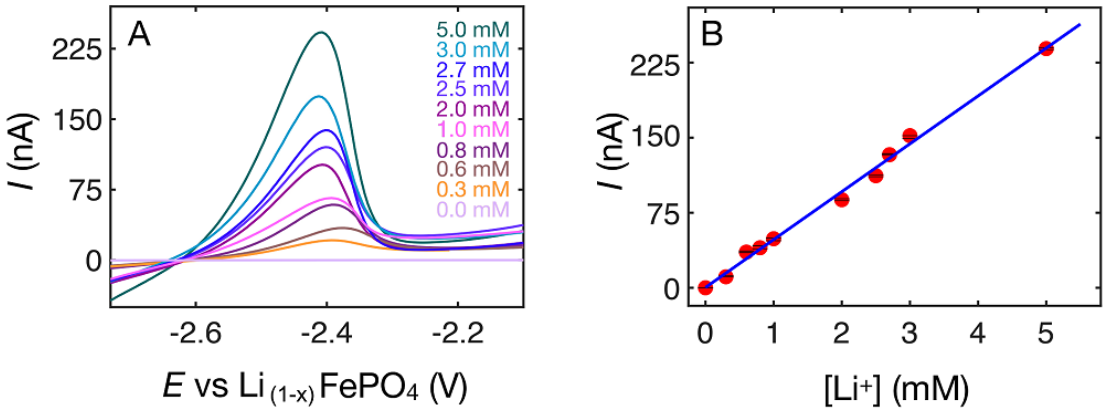

Figure 3.3 SWV for Li^+ detection. Electrochemical response from the standard solutions of $LiPF_6$ (0.30–5 mM) (A). Calibration curve based on the peak in A (I (nA) = 47.8 [Li^+] + 0.33) (B).

3.4.3 Formation of SEI Layer

Formation of the cone shaped Ga was examined at the tip of a 1.5 mm Pt electrode as well. The electrochemical response of prepared electrode (ASV) was examined in the solution of 1M LiPF6 in PC and the modification at the Ga surface electrode was studied using a camera (Dino-Lite digital microscope, model AM-411T) placed beneath the electrochemical cell (Figure 3.4.A).

Sweeping the potential from 2.5 V toward the negative direction, lithium-ions were reduced and Li metal was absorbed in the Ga electrode. Subsequently the formation of SEI layer at the Ga surface is noticeable. The SEI layer permanently covered the Ga surface and it was stable during 4 cycles of CV. This simple experiment is a proof of SEI layer formation during the LIB operation. Figure 3.4 demonstrates the formation of SEI layer at its different stages with sweeping the potential during ASV.

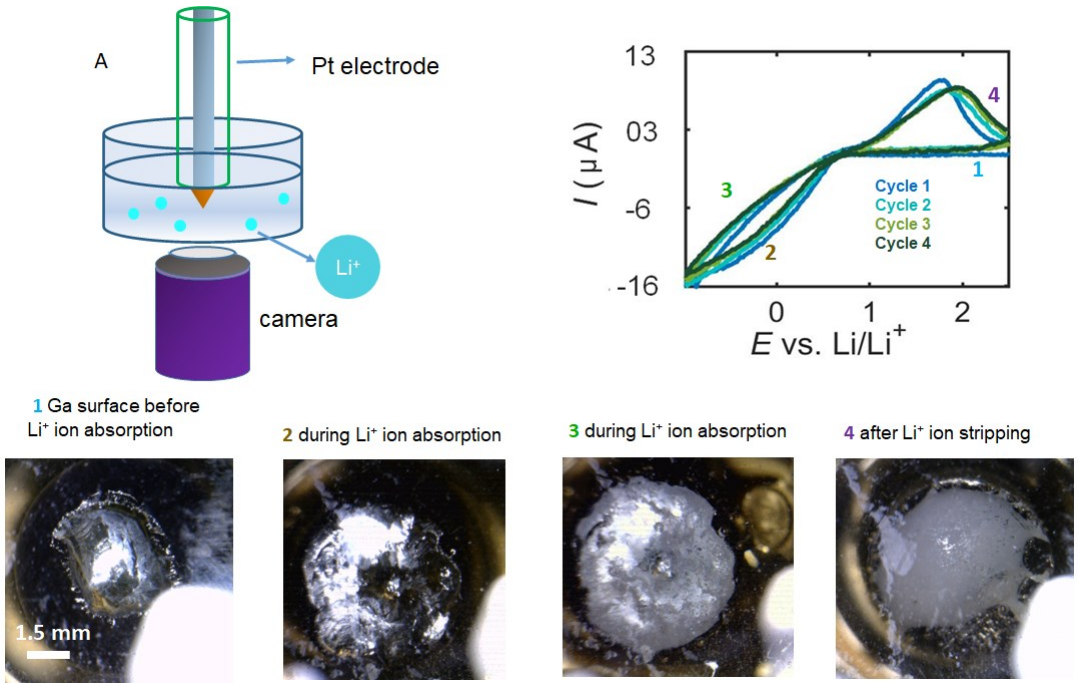

Figure 3.4 Scheme of surface detection using Pt/Ga electrode (A). Electrochemical response at the Pt/Ga macroelectrode surface (1M $LiPF_6$ in PC. RE, CE: Li/Li^+, 2.5 to -1 V at 0.1 V s^{-1}) (B), CV is divided to 4 zones in regard to Li^+ ion absorption and stripping and the micrograph related to each zone is represented below with the right numbers.

3.5 Conclusion

This work investigated the Pt/Ga ultramicroelectrode function for lithium-ion detection for different concentrations between 0.3-5 mM for the first time. The results of this work confirmed that with an easier preparation method, the Pt/Ga system is a good choice as an alternative probe to toxic metal/mercury electrodes. The CV analysis shows lithium can be deposited into gallium reversibly, however, peak shifting and high LOD makes this electrochemical technique less ideal. As such, SWV has was employed, yielding a linear calibration curve with a 77μM limit of detection in LIB relevant environments. This detection scheme opens an avenue spatially resolved lithium distribution measurements as well as time-dependent evolution of the electrolyte concentration at electrode-electrolyte interfaces.

3.6 Acknowledgment

The authors are grateful for financial support of the work by General Motors and the Natural Sciences and Engineering Research Council of Canada (CRDPJ 494074-16) and the financial support of Université du Québec à Montréal.

CHAPITRE IV

LOCAL DETECTION OF LITHIUM IONS IN LITHIUM ION BATTERY MATERIALS USING PT/GA MICROELECTRODE

Mass transport phenomena are important factors in battery operation. For instance, if the insertion/deintercalation of the Li^+ is slow during battery cycling, the battery will not be capable of providing enough power for high-power applications. Consequently, finding the local concentration of Li^+ released from the cathode material is one of the critical measures to be performed in LIBs. Here in this chapter, the local current of Li^+ from different locations of the active LFP material is measured and converted into a map of the local concentration of Li^+ released to the solution based on the calibration curve from the previous chapter.

This chapter is prepared for submission to The Journal of the Electrochemical Society.

Mojgan Hatami, Prof. Janine Mauzeroll, and Prof. Steen Brian Schougaard are co-authors of this article.

The contributions of the authors of the article are as listed below:

• Mojgan Hatami: Design of experiments, experimentation, data analysis, figures.

• Prof. Janine Mauzeroll: Discussion, manuscript editing.

• Prof. Steen Schougaard: Supervisor of the research and experimentation, manuscript editing.

4.1 Abstract

The exchange of Li^+ during charge/discharge is at the heart oflithium-ion battery (LIB) operation. However, information on the transport of these ions in the different components of the LIB materials is limited. In this report, the quantity of Li^+ deintercalated during charging cycle was determined using scanning electrochemical microscopy (SECM). This technique was selected based on its ability to record the local current responses at a microscale probe. By coupling SECM with anodic stripping voltammetry (ASV), a map of the concentration of Li^+ above the cathode surface was derived *during* charging. Due to the strongly reducing potential of Li deposition, no SECM redox mediator could be found. Instead, direct contact using the liquid probe was utilized to overcome the challenge of approaching the surface in absence of mediator. Finally, the method validation was performed based on recording distinct currents from a micropinhole and the covered areas in the proximity of the hole, which revealed the spatial resolution of the technique.

4.2 Introduction

LIBs with high energy density, long life span and no memory effect are an excellent choice for use as an energy source in electric vehicles (EV) and electronic devices (Mirzaeian et al., 2022; Qiao & Wei, 2012; Semeraro et al., 2022). Because of their practical importance, LIBs have experienced significant improvements in their performance over the past decades. In order to provide higher power a more detailed knowledge about the electrochemistry within the LIBs is required. For instance, lithium ion intercalation/deintercalation in electrode materials seems to be the rate-limiting step in the applications which needs high-power like hybrid or plug-in hybrid electric vehicles (PHEV), however, the characteristics of these phenomena is still mysterious

(Barton & Rodríguez-López, 2014; Hossain et al., 2019; Stephenson et al., 2007). Moreover, the Li^+ transport in LIBs that involves the mass transport in the electrolyte solution inside the porous composit electroderequires further detailed studies.

In recent years, in addition to SECM, more scanning probe microscopy (SPM), such as scanning ion conductance microscopy (SICM) and scanning micropipette contact method (SMCM) have been employed by different research groups to detect the interfacial flux of alkali metal cations (Dayeh et al., 2019; Kempaiah et al., 2019; Payne et al., 2019; Snowden et al., 2016; Takahashi et al., 2010). For instance, Hersam et al. reported surface topography of battery cathode materials and organic photovoltaic cell (OPC) materials (Lipson, Albert L. & Hersam, 2013). Also Rodríguez-López et al. determined the current of alkali metal at an electrified surface inside an organic battery solution (Barton & Rodríguez-López, 2014; Lipson, Albert L et al., 2011; Lipson, Albert L. & Hersam, 2013). Continuing challenges include lowering of the limit of detection (LOD) and increasing the sensitivity of these methods. With these considerations in mind, here we present local detection and quantification of Li^+ using SG/TC mode of SECM in organic electrolyte solution. Using ASV to measure the local current, the Li^+ absorption and stripping peaks are detected at various locations over the cathode. In order to avoid the interference of mediator molecules in Li^+ ion detection, we arrange to use a simple technique to approach the surface in a mediator-free environment. Thus, in this study the local quantity of the Li^+ from different points of $LiFePO_4$ electrode is mapped. In addition, the experimental work provides spatially resolved detection with a resolution of 10 μm.

4.3 Experimental

4.3.1 Chemicals and Instruments

Lithium hexafluorophosphate ($LiPF_6$), and Tetraethylammonium tetrafluoroborate ($TEABF_4$) were purchased from Gotion (Fremont, USA), N-methyl-pyrrolidone (NMP), anhydrous 99.5% and propylene carbonate (PC), also Methyl viologen dichloride hydrate *p*-benzoquinone were purchased from Sigma-Aldrich (Oakville, Canada). Metallic Ga was acquired from Fisher scientific (Toronto, Canada). Acetic acid (CH_3COOH) and hydrogen peroxide (H_2O_2,30%) were purchased from Fisher scientific (Toronto, Canada), carbon coated lithium iron phosphate C-$LiFePO_4$ from Phostech Lithium Inc. (Quebec, Canada), poly (vinylidene fluoride) (PVDF) from Kynar KF Polymer, carbon (CS65) form Timcal (Cambridge, UK). Silver wire for use as a counter electrode in ASV experiments, from Goodfellow (Huntingdon, England). (2 mm diameter, 99.99% purity). Al foil and carbon double side tape from Uline (Milton, Canada).

All the SECM measurements were conducted inside an argon-filled glovebox (MBraun, USA, $O_2 < 0.5$ ppm, $H_2O < 1.5$ ppm) and performed using an Electrochemical Probe Scanner 3 (Heka Elektronik, Germany).

4.3.2 Pt and Pt/Ga Microelectrode Fabrication

The fabrication protocol of Pt ultramicroelectrode has previously been published (Danis, Polcari, et al., 2015). The modification with metallic Ga was presented with in chapter 3.

4.3.3 $Li_{(1-x)}FePO_4$ Reference Electrode Fabrication and $LiFePO_4$ Film preparation

$Li_{(1-x)}FePO_4$ coated wire and $LiFePO_4$ were previously published (Lepage et al., 2011) and for the $Li_{(1-x)}FePO_4$ reference electrode see chapter 3.

The protocol for $LiFePO_4$ film (LFP) preparation consisted of casting slurry of $LiFePO_4$, PVDF as binder and carbon black in 2.5 mL of NMP per 1 g solid material. All the above chemicals were blended in the ratio of 8:1:1 (respectively) and mixed for 24 hours using a roller mill. Subsequently, the slurry obtained was cast on the Al current collector using a doctor blade before being vacuum dried at 100° C for 24 hours (Hossain et al., 2019; Lepage et al., 2019).

4.3.4 SECM Experiments

The SECM experiments were performed to detect the current of Li^+ emitted from a 3 mm × 3 mm square piece of LFP-electrode$^+$. The overall scheme of the electrochemical cell used for SECM is shown in Figure 4.1.A. A piece of carbon tape (double sided type) attached the LFP film to a glassy carbon electrode. This assembly acted as the second working electrode (W2) and was located in the center of an electrochemical cell. The first working electrode (W1) was the Pt/Ga cone shape microelectrode prepared above. W1, W2, counter and reference electrodes (Ag_xO and $Li_{(1-x)}FePO_4$) were immersed in 0.1 M solution of $TEABF_4$ in PC as electrolyte (Figure 4.1.B).

For recording the local current, W1 must be in close proximity to the surface (Polcari et al., 2016). In the presented experiments no redox mediator was added to the solution. Consequently, the distance from the surface was determined by approaching the tip to

the surface until the liquid Ga, touched the surface of the film, at which point a sharp increase in the current was observed at W1 and the electrode was stopped and raised (retracted) by 2µm. In order to confirm that the Ga surface was not modified during the experiment, ASV voltammograms were recorded before and after film measurements in a solution of 1 mM of $LiPF_6$. The overlapping ASV current curves confirmed that the electrode remained unchanged after touching the surface.

The current of Li^+ from different areas of the LFP film was recorded using LS-ASV at the tip of a Pt/Ga microelectrode at a distance of 2µm from the film surface. While it was found In chapters 2 and 3, that SWV can provide higher sensitivity and improved reproducibility, technical difficulties with instrument control precluded its use here. In LS-ASV absorption peak data reproducibility is demonstrated in figure 4.3.A. A potential of +0.4V vs. $Li_{(1-x)}FePO_4$ was applied to W2 during the SECM measurement to release Li^+ from the LFP film. To confirm that the origin of the signal was Li^+ from the film, local detection was performed for different locations of the film in the absence of this imposed potential in a separate experiment (Figure B.2). The currents detected from this blank test were negligible (<0.5 nA).

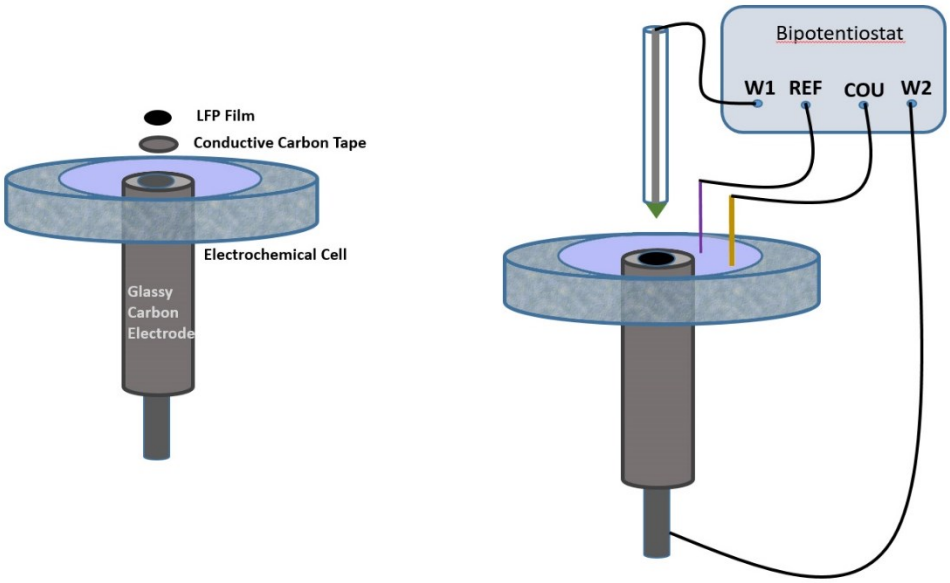

Figure 4.1 Scheme of electrochemical cell (A) and SECM set up (B) for Li^+ ion diffusion detection from LFP film.

In an attempt to determine the spatial resolution of the technique, the transport of Li^+ was delimited by a micrometer sized cylindrical pinhole. For this purpose, the Pt/Ga microelectrode was placed at the top of the hole at a distance of 2µm. Before the experiment, the position of the hole relative to the liquid probe was adjusted using a camera (Dino-Lite, AM-411T) by illuminating beneath the pinhole (Figure B1). Subsequently, the Pt/Ga microelectrode was approached to the hole and adjacent positions to determine the current of diffusing Li^+. In this cell assembly, the LFP film was placed flush against the backside of the pinhole substrate during the SECM experiment.

4.3.5 The Comparison the Area of Two Microelectrodes

The area of Pt/Ga microelectrode that was used for detection of the local current of the film and hole, must be close to the one that used for preparation of the calibration curve

(chapter 3) if the calibration curve is to be valid. This size conformity was verified using the micrographs of the probes i.e. the cross sectional areas (Figure 4.4.A).

4.4 Result and Discussion

4.4.1 Determination of Li^+ Ion Currents

ASV was used to detect the absorption/stripping of Li^+ to the Pt/Ga microelectrode at a distance of 2 μm from the surface (Figure 4.3.A). The cathodic current of the voltammogram (Figure 4.3.A) is associated with the absorption of Li metal into the Ga cone whereas, the anodic current which forms a peak, represents the subsequent lithium stripping. Recording voltammograms at the desired locations above the film allows the generation of a surface map (Figure 4.3.B) based on the peak stripping current of the ASV. To this end, the background for the stripping process was estimated by extrapolation of the current in the range of -1.5 to -1.8 V. Different locations at the surface of the film were chosen arbitrarily to evaluate the local detection method.

In order to release Li^+ from the cathode material, it is necessary to impose a current or a potential to oxidize the material. In this report, a constant potential (+0.4 V vs. $Li_{(1-x)}FePO_4$) was selected for film oxidation. The chronoamperometry of the film confirmed the LFP oxidation and established a steady-state current from the film over an extended period (Figure 4.2).

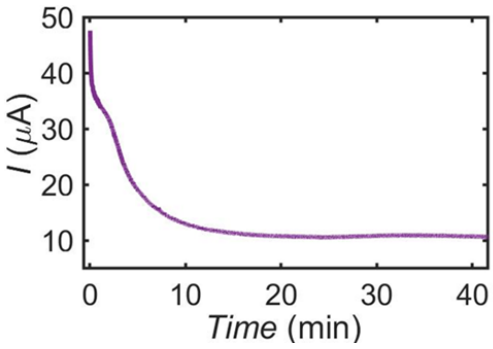

Figure 4.2 Chronoampherometry of Li^+ release from the film. The imposed potential to the film is +0.4 V vs. $Li_{(1-x)}FePO_4$

The SECM stripping current appears to increase over time *i.e.* the locations which were scanned first show currents around 45 nA whereas the last locations showed currents of 65 nA. The Li^+ current for each landed area was investigated using three ASV cycles, which showed a high degree of reproducibility in the presented data.

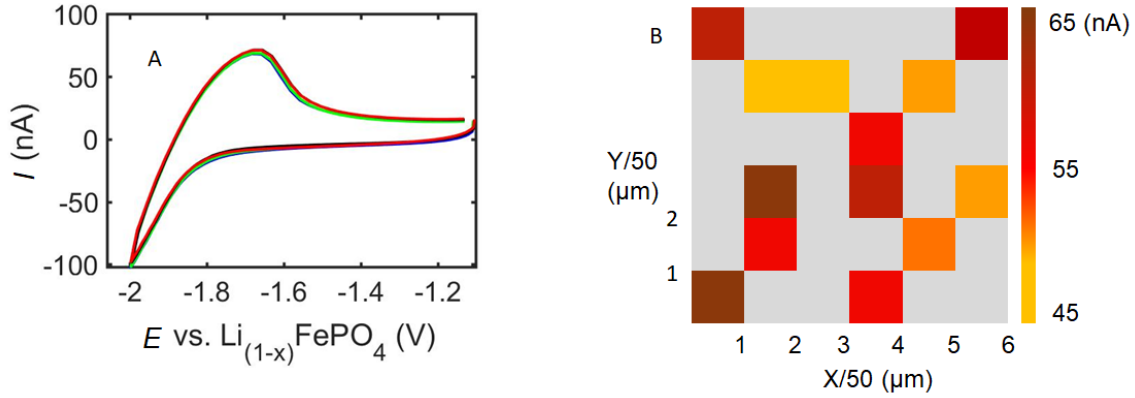

Figure 4.3 Mapping the LFP film surface. ASV of Li^+ released from a LFP film in a solution of 0.1 M $TEABF_4$ in PC, RE: $Li_{(1-x)}FePO_4$, CE: Ag_xO , scan rate 0.1 V s^{-1}, E_{sample} = 0.4 V vs. $Li_{(1-x)}FePO_4$ (A). Mapping diagram of the film. x and y are representing the direction in the surface plane of the film. Note that gray areas are not examined. Tip-surface distance: 2 μm (B).

The local Li^+ concentration was derived from the calibration curve previously presented (chapter 3) assuming an equivalent Pt/Ga microelectrode surface area (Figure 4.4.B). From the micrographs this equivalence assumption error was estimated to ~8.5%. Li^+

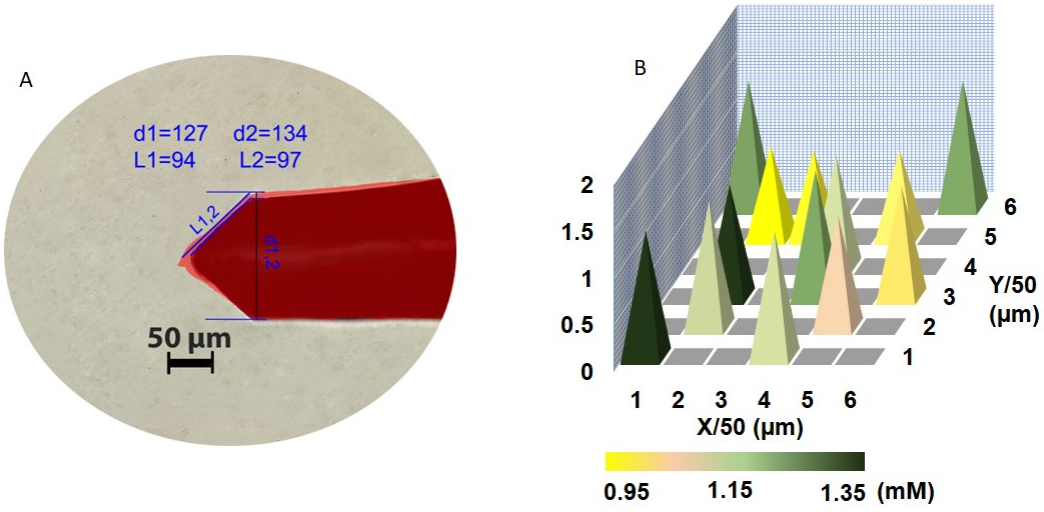

Figure 4.4 Comparison of the micrographs of Pt/Ga microelectrodes used to prepare the calibration curve and the Pt/Ga microelectrode used in SECM experiments (A) and map of Li^+ concentration for different locations of the surface of the film (B).

4.4.2 Microelectrode Performance

To examine the probe performance a series of validation tests were performed including microelectrode stability and microelectrode spatial resolution. The electrode stability was tested in a series of solutions with different concentrations (chapter 3).To confirm the electrode stability during the SECM measurements, LS-ASVs were recorded for 70 cycles in a solution of $LiPF_6$. Figure B.3 shows overlap confirming *I* vs. *E* curve probe stability.

To determine the SECM experiment resolution, a 20μm micropinhole (Figure B.1 in appendix of this thesis) was installed on top of the LFP film. The masked area of the surface prevents Li^+ transport to the microelectrode, so that only Li^+ which released from beneath the hole should reach the Ga/Pt probe. The spatial resolution is defined as the ability to distinguish between two structure or the smallest element that a sensor can detect (Leslie, 2018; Liang, S. et al., 2012). Here we used a slightly different definition, where resolution was defined as the lateral distance at which the microelectrode is capable of recording the Li^+ released from the pinhole. As such, Pt/Ga microelectrode scanned the surface masked and bare areas *i.e.* the hole (Figure 4.5 .A, providing the Li^+ concentration map (Figure 4.5.B) from ASV (Figure 4.6).

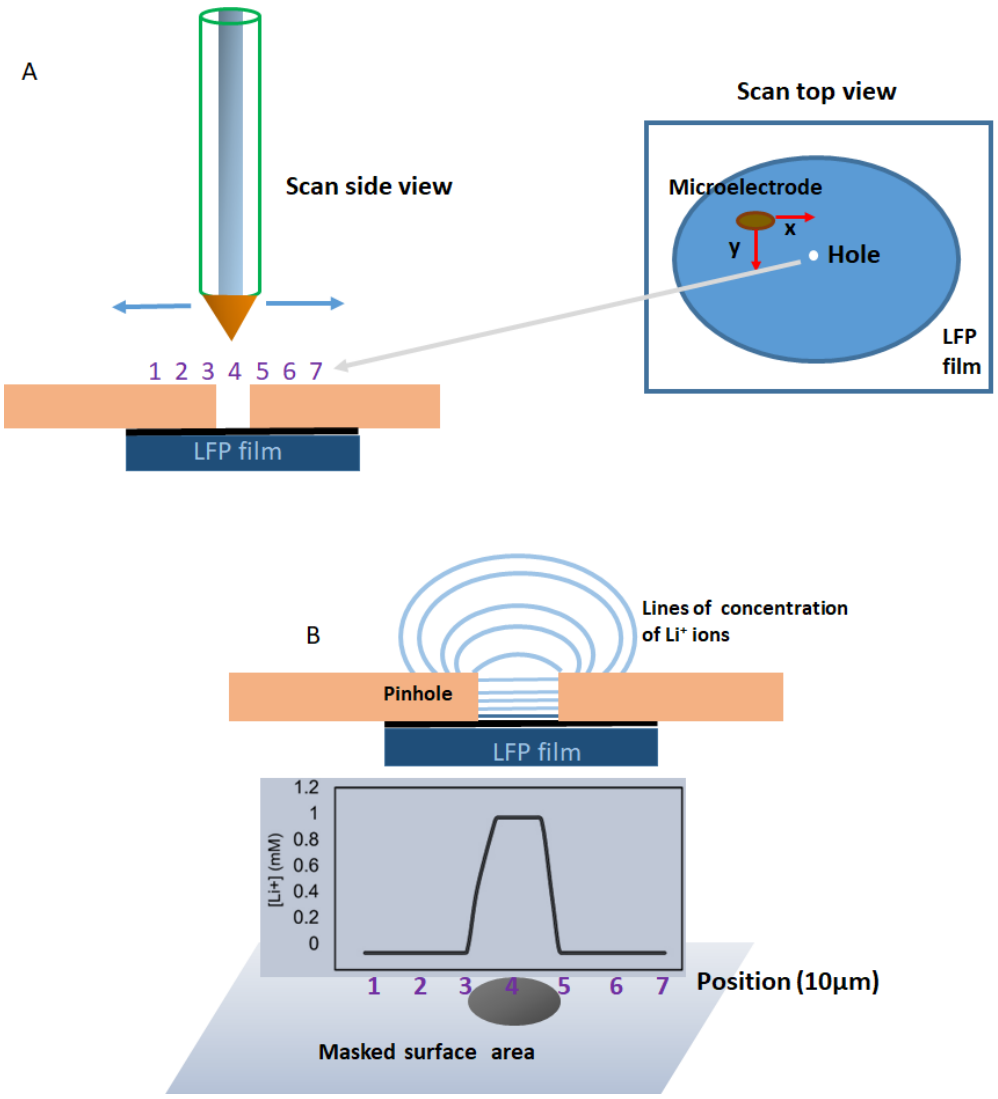

Figure 4.5 Scheme of the side view and top view of the scan with electrode and the current of Li^+ (A). (B) Experimental concentration profile for the LFP surface beneath the pinhole (20µm) for different locations in the solution of PC and 0.1 M $TEABF_4$ as support electrolyte, RE: $Li_{(1-x)}FePO_4$, CE: Ag_xO, scan rate 0.1 V s^{-1} E_{sample}= 0.4 V vs. $Li_{(1-x)}FePO_4$ (B).

The Li^+ concentration profile induced by the oxidative potential applied to the film and ensuing release of Li^+, follows the mass transport inherent to the pinhole geometry. In

proximity to the surface, the iso Li^+ concentration contour lines are parallel to the electrode surface, whereas in bulk of the solution they are approximately hemispherical.

Since an above detection limit stripping current was *only* detected at the position immediately above the hole (Figure 4.6), we deduce that the Pt/Ga microelectrode is *at least* capable of detecting the distinct release of Li^+ from "point" sources separated by 10 µm. (I.e. the lateral spatial resolution under the imposed conditions is smaller than or equal to 10 µm). It should be noted that the provided spatial resolution depends on the size and geometry of the Pt/Ga micro probe and the resolution of the scanning technique as well as the tip to surface distance. This is further detailed in chapter 5 where an experimental procedure is proposed to detect the resolution of technique with higher accuracy.

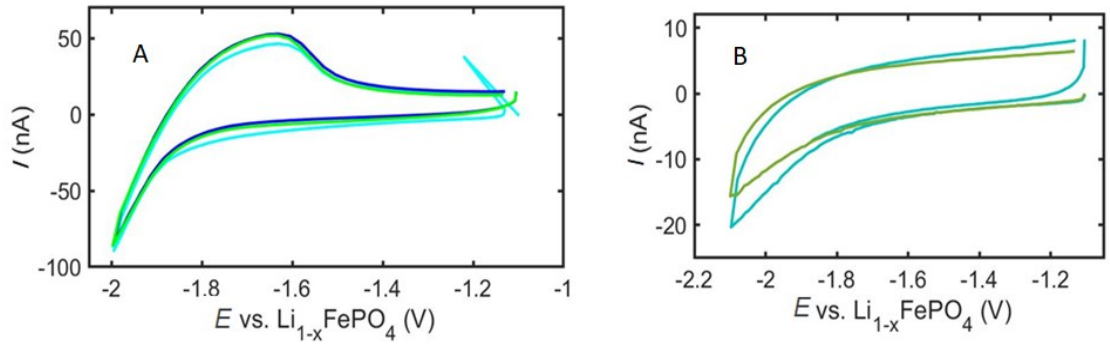

Figure 4.6 ASV of Li^+ at the top of the pinhole (20µm) (A) and the area which were masked (B), in the solution of PC and 0.1 M $TEABF_4$ as support electrolyte, RE: $Li_{(1-x)}FePO_4$, CE: Ag_xO, scan rate 0.1 V s^{-1} E_{sample}= 0.4 V vs. $Li_{(1-x)}FePO_4$.

The presented experiments differ from common electroanalytical theory which is based exclusively on diffusion and planar electrodes, as two different cations are in play and the electrode is porous leading to a redox reaction distributed over a volume. However,

in the following we will qualitatively examine the obtained data, to get a more detailed understanding of the electrochemical response and the ensuing Li^+ concentration gradient.

In cases where supporting electrolyte approximation and in cases where a single binary electrolyte is appropriating the electrolyte mass transport is given by (Newman & Thomas-Alyea, 2012) :

$$\frac{\partial C}{\partial t} = D\,\nabla^2 C \qquad (4.12)$$

For the binary electrolyte $D = \frac{u_+ D_- + D_+ u_-}{u_+ + u_-}$, and C is the concentration of the cation or anion D_+, D_- are the diffusion coefficients of the cation and anion in the organic solution, and u_+ ,u_- are the mobility of the cations and anions. In the supporting electrolyte approximation D and C simply refer to the diffusion coefficient and concentration of the electroactive species. In a potential step experiment, as applied to the LFP film, the surface concentration will initially be strongly reduced and we expect a Cottrellian behavior. In the case of linear diffusion this will lead to a current that decay as $\frac{1}{\sqrt{t}}$, i.e. specifically for a planar electrode:

$$i = {nFAD^{\frac{1}{2}}C}\Big/{(\pi t)^{\frac{1}{2}}} \qquad (4.13)$$

As such, the current response of the film shown in Figure 4.2, follows the expected behavior initially. However, at long times a steady state current (independent of time) is found. This is explained based on the charge curve of the LFP cathode material (Cui et al., 2020). During the majority of the constant current charging cycle, LFP generates a constant potential due to a phase separation process within the LFP material (Tomaszewska et al., 2019). So the constant current generates a constant potential, and

it follows that the constant potential imposed to the film in the SECM experiment would generate a constant current once the two-phase mechanism is dominating.

The film capacity can be calculated based on the chronoamprometric curve of the film Figure 4.2. using the S/M equation where S is the area under the chronoamperometry curve and M is the weight of the active material. The capacity of the film was (9.40 mAh g^{-1}) which divided by the theoretical capacity of the LFP (170 mAh g^{-1}) yields the delitiation degree of the film, approximately 0.055 compared to 1 for nominal $FePO_4$. The result of the calculation confirms that the film is in the plateau part of the charging curve which begins at approximate 3 % delithiation (Cui et al., 2020).

4.4.3 Discussion on the Contribution of Diffusion in the Current of Li^+

The transport of Li^+ from the film is theoretically dependent on both migration and diffusion (See introduction section 0.2.4). However, the amount of Li^+ injected (0.95-1.35 mM) compared to the total salt concentration (0.1M), as well as the $\frac{\partial \varphi(x)}{\partial x}$ term in Nernst-Plank equation (section 0.2.4), expected from passing a current density of 10-50 μA through approximately 1cm^2 of electrolyte with 3.3 S cm^{-1} conductivity allow us to use the supporting electrolyte approximation (Tyunina et al., 2011). Consequently, the diffusion expression for a semi-infinite diffusion system with a constant imposed current from a flat surface was used here (Bard & Faulkner, 2001) to provide the Li^+ concentration above the LFP film

$$C = \frac{j}{FD}\left(2\left(\frac{Dt}{\pi}\right)^{1/2} exp\left(\frac{x^2}{4Dt}\right) - x\ \text{erfc}\left[\frac{x}{2(Dt)^{1/2}}\right]\right) \qquad (14)$$

Where j is the current density, F is the faraday constant, t is the time, x is the distance from the surface of the film, D is the diffusion coefficient of Li^+. Using the equation above, the concentration profiles of diffused Li^+ were obtained (Figure 4.7).

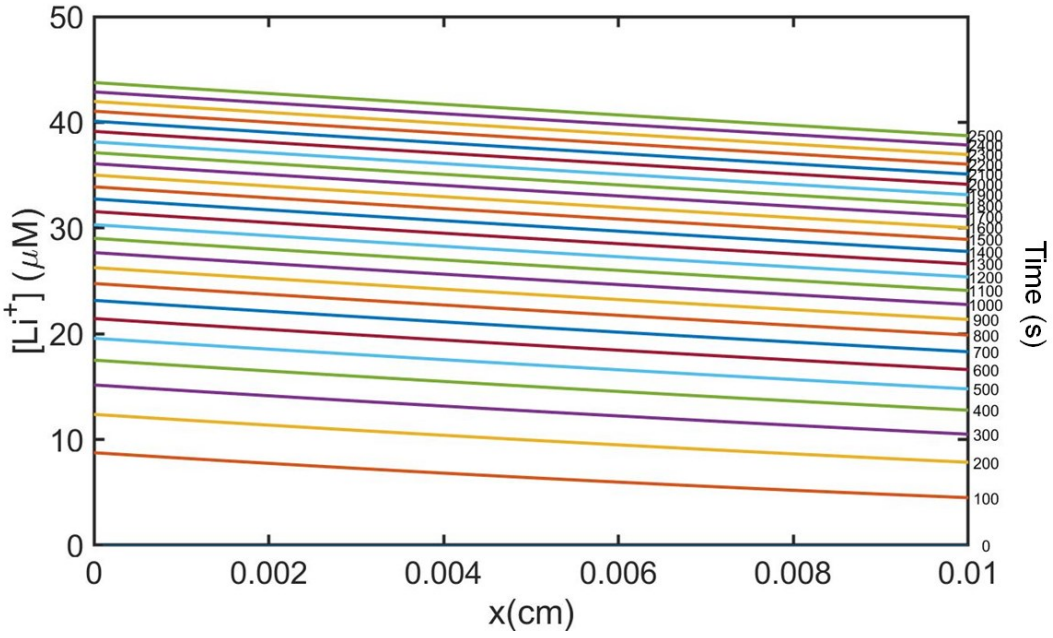

Figure 4.7 Time resolved Li^+ concentration profiles Li^+assuming a perfectly flat LFP film. The imposed current density, j=110 µA cm^{-2}. $D_{Li}^{+} = 2.2 \times 10^{-6}$ cm^2 s^{-1} (Tsunekawa et al., 2003).

From Figure 4.7 it is clear that the measured mM concentrations, several orders of magnitude greater than predicted from e.g. eq.14 suggests that the planar diffusion only approximation does not capture the full behavior. Clearly more sophisticated models should be developed.

4.5 Conclusion

In this work, we determined the local concentration of Li^+ released from a cathode material of a LIBs during charge using the SECM technique. For this purpose, the current of Li^+ released from a LFP film by applying the oxidative potential, was measured at the tip of Pt/Ga microelectrode, and correlated to concentration of Li^+ at each location using a calibration curve. The result was a surface map of the concentration Li^+ ions released to the electrolyte from electrode/ electrolyte interface. The current of Li^+ is driven by both migration and diffusion, however, the migration contribution seems to be dominant as the diffusion only analysis shows poor correlation to experimental results. Because the electrolyte contained a high salt concentration, using Nernst-Plank equation (0.2.4) for determining the migration portion is not feasible.

Importantly, unlike the classical SECM feedback modes the reduction potential of Li^+ degraded all tested mediator molecules. Consequently, all experiments were performed in the mediator-free solution media. The key feature being that the liquid Ga tip allowed direct contact with the surface.

Overall, the validity of the Pt/Ga microelectrode methodology for local detection of Li^+ was confirmed by recording Li^+ being transported through a micropinhole compared to the adjacent covered areas. The determined spatial resolution was smaller than or equal to 10 μm.

CHAPITRE V

CONCLUSION

5.1 Motivation of Study and Challenges

The main goal of the experimental work of the previous four chapters was the proposition of a methodology to study metal cation release from the cathode of LIBs into the electrolyte. Overall this work has three important aspects. First, the metal cations which were the target of study in the different chapters have a profound effect on the performance of the LIB. For instance, manganese cation leaching, which was the main focus of the study in chapter 2, has a serious negative impact on battery performance. The ionic current was the main subject of the study of chapters 3 and 4, as Li^+ exchanges between the cathode and anode during charge and discharge.Li^+. The current produced by these ions (Mn^{2+} or Li^+) is directly correlated with the provided calibration curve; therefore, the developed experiment can provide a powerful method for obtaining the cation concentration directly. As such, the performance of two trapping materials for Mn^{2+} elimination was evaluated using the current of manganese ions which remained in the solution.

Moreover, as it was discussed in chapters 3 and 4, using a Pt/Ga microelectrode and forming a Li/Ga alloy Li^+, the stripping current and subsequently, the concentration of Li^+ was determined. As such, the local concentration of Li^+ released from the LIB cathode material was measured.

The second fundamental advantage of this study was establishing a methodology to study the *local* behavior of species at the battery materials. For instance, a portion of chapter 4 was devoted to expanding a technique for recording the concentration of the Li^+ which diffused from the film surface at the interface of the electrode/electrolyte. The main purpose of this study was quantification of the heterogeneous Li^+ transport from solid material into the electrolyte. This provides information about the kinetics of the charge/discharge reaction. In addition, the second part of chapter 4 elaborated a method for obtaining the spatially resolved Li^+ detection by comparing the current of the film from a pinhole with the adjacent masked area which did not pass current.

The third significant advance of this thesis was to illustrate some serious challenges in metal cation detection in LIBs. For instance, the detection of the Mn^{2+} using ASV for solutions with a concentration of less than 0.5 mM was unreliable, i.e. the ASV LOD (330μM) was not sufficiently low for use in the studies of LIB. Hence, the detection method was changed to SWV and thus the contribution of the non-faradic current was greatly reduced and the stripping peaks could be recorded for lower concentrations (e.g. 0.1 mM) with high reproducibility (The features of SWV are described in detail in Chapter1). By solving this critical problem, this work will accelerate advancements in low-concentration detection of Mn^{2+}. Additionally, early attempts for Pt/Ga microelectrode preparation was based on direct Pt tip contact with the Ga source, but the results were not promising(Figure 5.1). To avoid random geometry and increase consistency in size and shape, a protocol for fabricating a conical Pt/Ga microprobe was developed.

In comparison with Hg, Ga act differently to form a microelectrode with Pt. Although the Ga source which was used in the experiment was liquid at room temperature, it does not show the tendency to spontaneously reflow to form a shape with the lowest interfacial free energy (Chiechi et al., 2008). By taking this into account, it can be

formed into metastable, non-spherical shapes like that of a cone which was produced in this work.

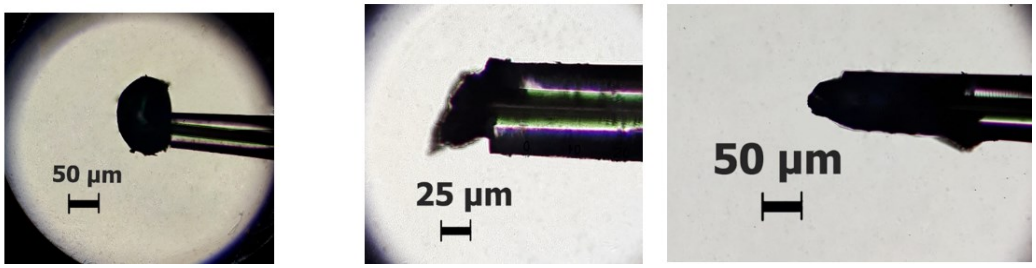

Figure 5.1 Micrographs of the Pt/Ga microelectrode with random geometry after direct contact with Ga source.

As it was discussed in chapter 4, one major challenge in Li^+ detection was the lack of a suitable mediator for use in feedback mode SECM to approach the surface, due to the mediator degradation at the reduction potential of Li^+. Eventually, the idea of landing onto the conductive surface using the liquid microelectrode, touching the surface and raising the electrode overcame this challenge.

5.2 Proposition of Future Works

The suggestions for future work in upcoming titles focus on the topic of local determination of the Mn^{2+} and Li^+ in LIB materials.

5.2.1 Local Quantification of Mn^{2+} From *Spinel* Cathode Material of LIBs

As described in chapter 2, *spinel* type cathode materials in LIBs release manganese ions to the electrolyte. Detection of local current for different areas of LMO films can be performed using Pt/Hg microelectrodes. A good choice of technique for this purpose

is SECM in the feedback and SG/TC mode. Using positive feedback mode, the microprobe (Pt/Hg microelectrode) will approach the LMO surface and the current of the Mn^{2+} ions will be recorded at the tip using SG/TC. Here MV isa proper choice as a mediator for the feedback mode. Figure 5.2 demonstrates the conditions of the experiment. The current of Mn^{2+} can be recorded using SWV.

$LiMnPO_4$ (LMP) is an *olivine* type manganese containing cathode that is stable during battery cycling without the effect of manganese leaching (Fang et al., 2008; Yang, L. et al., 2017). There should be no current of Mn^{2+} from the LMP film. As such, it will provide important evidence to confirm the current recorded from LMO in previous experiments stem from $Mn^{2+}$and there is no other source of current in the potential window of the experiment.

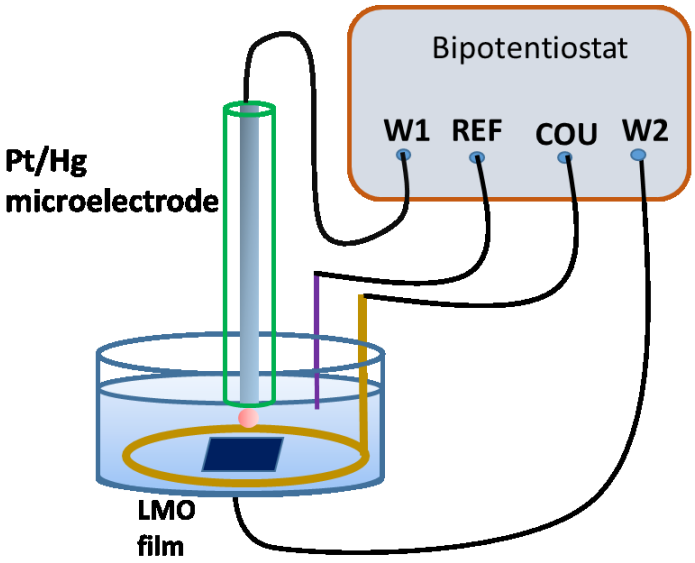

Figure 5.2 SECM set up for current detection of Mn^{2+} ions from LMO film. SWV of the Mn^{2+} ions released from the film in the solution of PC and 0.1 M $LiClO_4$ as support electrolyte. RE: $Li_{(1-x)}FePO_4$, CE: Ag_xO wire, scan rate 0.1 V s^{-1} E_{sample}= 0.85 V vs. $Li_{(1-x)}FePO_4$.

It is expected that by imposing a potential to the film of the *spinel* type LMO, Mn^{2+} ions dissolve more readily. The concentration of Mn^{2+} ions can be determined using the calibration curve presented in chapter 2. By measuring the concentration for different points, a surface map can be prepared that shows the release Mn^{2+} from the film. This map portrays important information about the quantity of cathode material leaching from different points and can be useful for studying the kinetics of this reaction. Moreover, it is possible to repeat the same experiment for samples with different tortuosity and porosity to study the relation of local leaching of Mn^{2+} with these parameters.

5.2.2 Determination of Li^+ Local Current in a Quasi Solid State Polymer Electrolyte

Solid Polymer Electrolytes (SPE) demonstrate some fundamental advantages over traditional LIB electrolytes. As it was elaborated in section 0.2.3, they especially improve safety compared to organic electrolytes. Studies on SPEs are of great importance, especially the lithium ion kinetics which are currently a limiting factor for their commercial application. This information opens avenues to better design the structure of SPEs and consequently improve the performance of the solid-state LIBs such as in the PEO/LiTFSI system. (Chen, F. et al., 2017; Zhao et al., 2008).

The goal of the experiment would be to detect the current of Li^+ at the interface of the SPE and a liquid electrolyte solution. It should be noted that in general there is no liquid electrolyte used in solid-state LIBs. However, there are a group of SPEs which consist of polymer matrices, a slab of Li (e.g. LiTFSI) and solvent. These systems are Quasi Solid Polymer Electrolytes (QSPE) and in this experiment, a QSPE would be the target of study (He, X. et al., 2021). A combination of PEO/LiTFSI and LFP electrode components immersed into the solution of electrolyte would serve as the SECM W2. A protocol of working electrode preparation could consist of two main parts, as follows. First the solid polymer electrolyte would be prepared by mixing PEO and LiTFSI in acetonitrile for 24 hours and then vacuum drying for 24 hours. The resulting film would be ground into powder and used as a binder for the preparation of the LIB cathode (e.g. LFP film). The protocol of the LFP preparation was detailed in chapter 3, and in this experiment, the slurry would be prepared using the same procedure, except replacing PVDF with the prepared polymeric binder. Finally, for LFP film preparation all of the materials in LFP slurry plus PEO and LiTFSI will be dissolved in acetonitrile, mixed and cast on an Al current collector using doctor blade (Chen, F. et al., 2017; Lepage et al., 2019).

The current of Li^+ from the electrode material prepared according to the above protocol would be recorded at a Pt/Ga microelectrode. The cell assembly for SECM would be similar to the electrochemical cell of chapter 4, and a mediator compound such as MV would be added to a solution of PC or DMC with $TEABF_4$ as supporting electrolyte. The reference and counter electrodes would be $Li_{(1-x)}FePO_4$ and Ag_xO respectively. The SG/TC could be a proper detection mode. As it was mentioned earlier, the electrochemical setup would require two working electrodes, W1 is the Pt/Ga microprobe which can approach to the surface to record the current of Li^+, and W2 which is the LFP and SPE system immersed in the solution of the electrolyte.

Similar to 5.2.1 of this chapter, the negative feedback mode and SG/TC are used in this detection scheme because of the need for the microprobe to approach the surface of the insulator polymer. In the film (W2) as soon as the potential is imposed, the cathode material is oxidized and Li^+ pass through the holes of the QSPE, and W1 which is located at a certain distance (for instance 3μm) of surface can record the current of Li^+. Once the microelectrode has approached the surface and the desired surface to tip distance has been established, the supporting electrolyte solution should be replaced with one without mediator. This step is necessary to prevent the negative impact from mediator reduction on the surface of Ga, as described in chapter 4 of this thesis. Afterwards, the local detection of Li^+ can be performed at the microelectrode near the substrate surface. In this state the microelectrode (W1) record the current of Li^+ which release from the cathode and QSPE system (W2).

5.2.3 Determination of Spatial Resolution in the Detection of Li^+ in LIB

In chapter 4, the spatial resolution of the local detection of Li^+ current was determined using a method in which the current of the Li^+ passing through a micropinhole was

detected at the Pt/Ga microelectrode. Then, based on the ability of the microprobe (Pt/Ga microelectrode) to record a distinct current, for the adjacent covered areas the spatial resolution of the technique was determined.

An extension of this work could be accomplished using a micro disk electrode with a specific diameter as W2. For instance, a 15 or 25 μm diameter Pt microelectrode could be selected and etched to desired depth (e.g. 65 μm). (Allen, 2014) Using a syringe, LFP slurry would then be injected into the hole of the etched microelectrode, filling part of the etched volume. Therefore, in this assembly, Li^+ is released from the hole by imposing the oxidative potential. Figure 3.5A shows this working electrode. The etching process can be done electrochemically and involves applying an AC 2.9 V to a solution of 30% $CaCl_2$ (sat.) + 10% HCl in H_2O. The depth of etching can be adjusted by the etching time (Arrigan, 2004).
Using such a system instead of the previous one (the cell assembly of the chapter 4) has several advantages. For instance, using a camera with a high performance zoom lens, the location of the microprobe on top of the tip can be independently confirmed. Secondly, the depth of the hole can be selected as can the diameter without constrains, in contrast to commercial pinholes that are available only in selected sizes. As detailed in the next paragraphs.

In the electrochemical cell of Figure 5.3.C the Pt/Ga microelectrode is located at the top of the Pt etched electrode. As Li^+ is released into the electrolyte from the top of the LFP when the oxidative potential is imposed, the Pt/Ga microelectrode can detect the concentration of the Li^+ using SWV and the calibration curves like the ones provided in Chapter 3.

In order to investigate the impact of the hole dimension on the current of released Li^+, the depth and diameter of the etched Pt microelectrode used in the experiment can be changed and the concentration profiles of Li^+ can be extracted for different depths and

dimensions. By scanning the top of the hole and nearby areas, the ability of the Pt/Ga microelectrode to record distinct currents is evaluated, and the minimum distance can be assigned as the spatial resolution of the microprobe.

Overall, the present study in this dissertation showed a promising result in the analysis of metal cations in micro-scale LIBs. The main goal of the proposed work in this chapter is to provide higher resolution or increase the accuracy in measurement of solution phase cation concentration in LIBs.

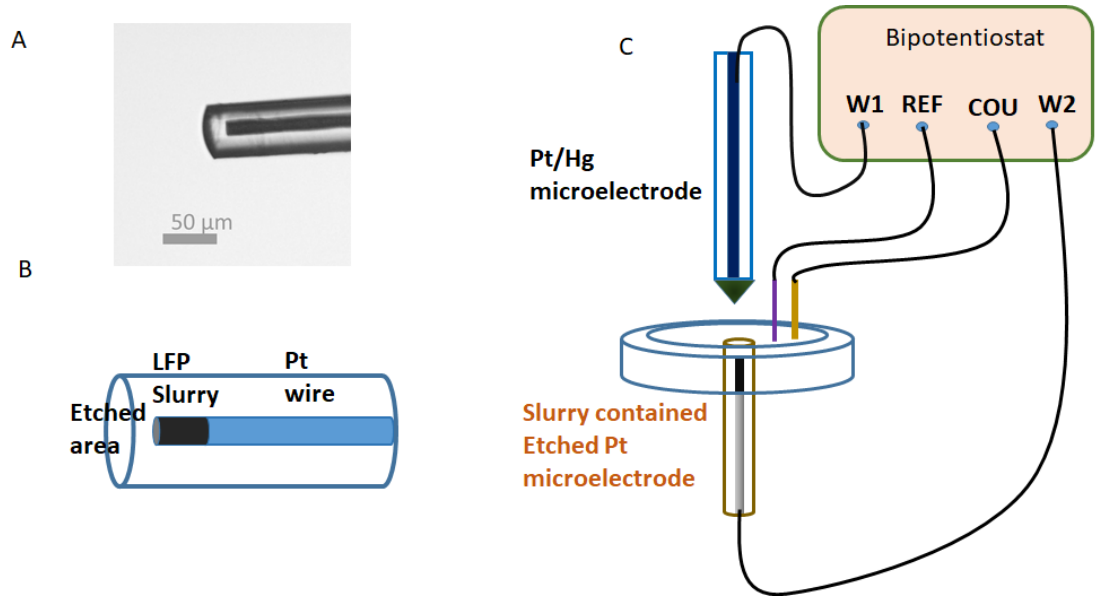

Figure 5.3 Side view of micrograph of an etched 10 µm Pt microelectrode (A), scheme of slurry contained etched microelectrode (B), Scheme of an electrochemical cell for determination of spatial resolution (C).

APPENDICE A

SUPPLEMENTARY INFORMATION FOR SQUARE WAVE ANODIC STRIPPING VOLTAMMETRY FOR LOCALIZED DETECTION OF Mn^{2+} IN LITHIUM-ION BATTERY ENVIRONMENTS

CV of platinum 25µm electrode in FcMeOH aqueous solution

Using FcMeOH as a material which is stable in aqueous solution is a standard material for investigating the performance of microelectrodes. The steady state current (i_{ss}) of the Pt microelectrode follows theory closely (Danis, Polcari, et al., 2015) .

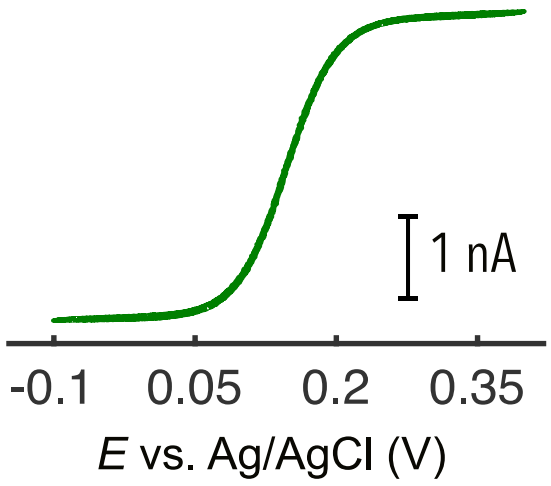

Figure A.1 Characterization of Pt disk microelectrodes. CV was performed in 1 mM FcMeOH in 0.1 M KCl (RE: Ag/AgCl, CE: Pt wire, -0.1 to 0.4 V, 0.01 V s^{-1}).

Mercury deposition chronoamperometry

The feature of the curve shows the sub processes of the mercury deposition on the tip of microelectrode. The first step of the figure shows the formation of the thin layer of Hg and Pt compounds like Pt_2Hg (Mauzeroll, 2007b; Yoshida, 1981), the second part with fluctuation indicating both Hg nucleation on the Pt tip, and droplet fusion. The last smooth part shows the growth of mercury spherical cap (Danis, Gateman, et al., 2015).

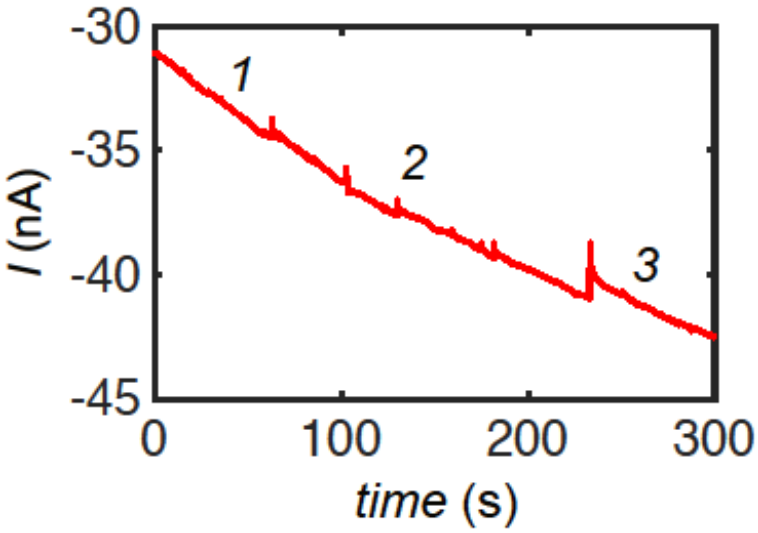

Figure A.2 Deposition of Hg hemisphere onto Pt microelectrode using chronoamperometry inside a glovebox. A potential of -800 mV vs. Ag QRE was applied for 300 s with the Pt microelectrode immersed 10mM $HgCl_2$ in 0.2 M $LiClO_4$/PC.

Typical ASV of Mn^{2+} solutions, using the Ag QRCE

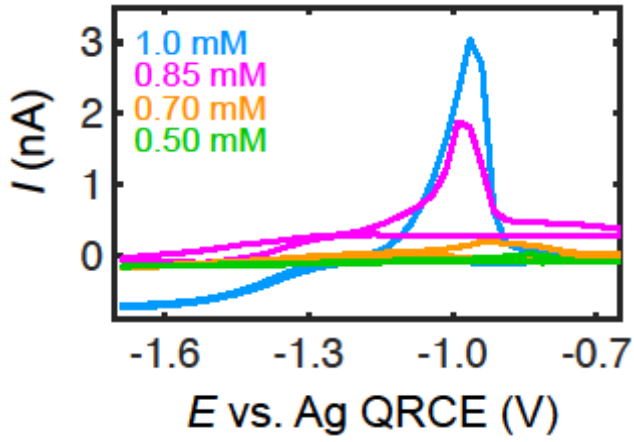

Figure A.3 Detection of Mn^{2+} using ASV. Electrochemical response at a Pt/Hg microelectrode in standard solutions of $MnCl_2$ (1-0.5 mM) (Electrolyte: 0.2M $LiClO_4$ in PC) RF: Ag QRCE scan rate: 50 mV s^{-1}.

APPENDICE B

SUPPLEMENTARY INFORMATION FOR LOCAL DETECTION OF LI^+ IN LITHIUM ION BATTERY MATERIALS USING PT/GA MICROELECTRODE

Microelectrode alignment at the top of the pinhole using a light beneath the hole

Using a light beam, the microelectrode above the hole was approximately adjusted. The adjustment was then completed using the electrode shadow.

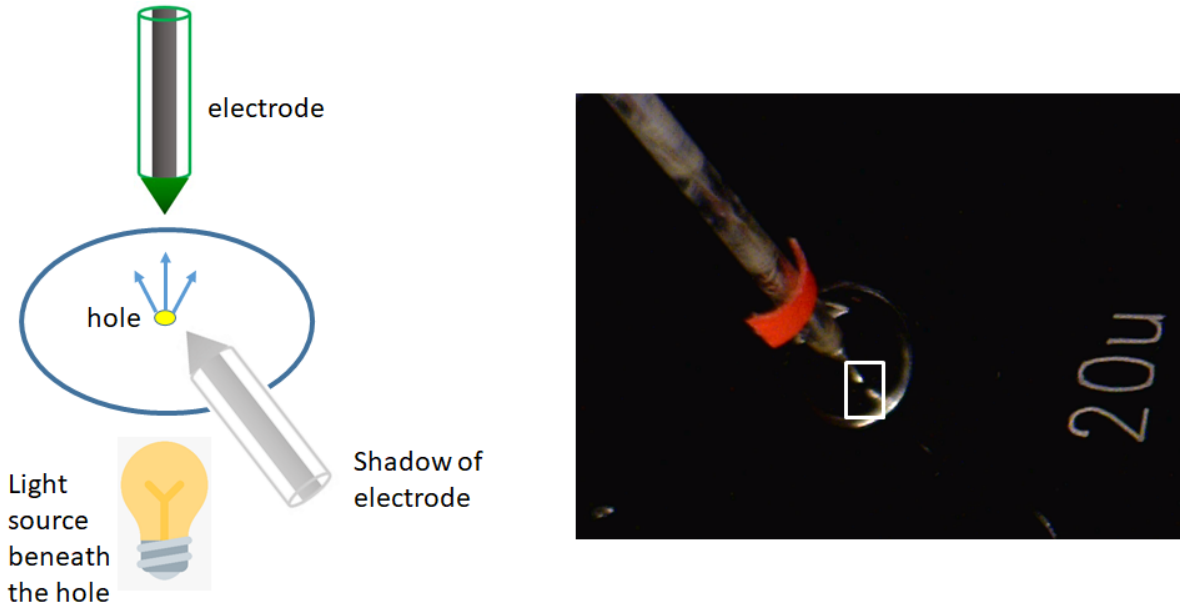

Figure B.1 scheme of microelectrode alignment at the top of the hole.

Local current from the LFP surface in the absence of film potential (the current of the film from different spots are negligible)

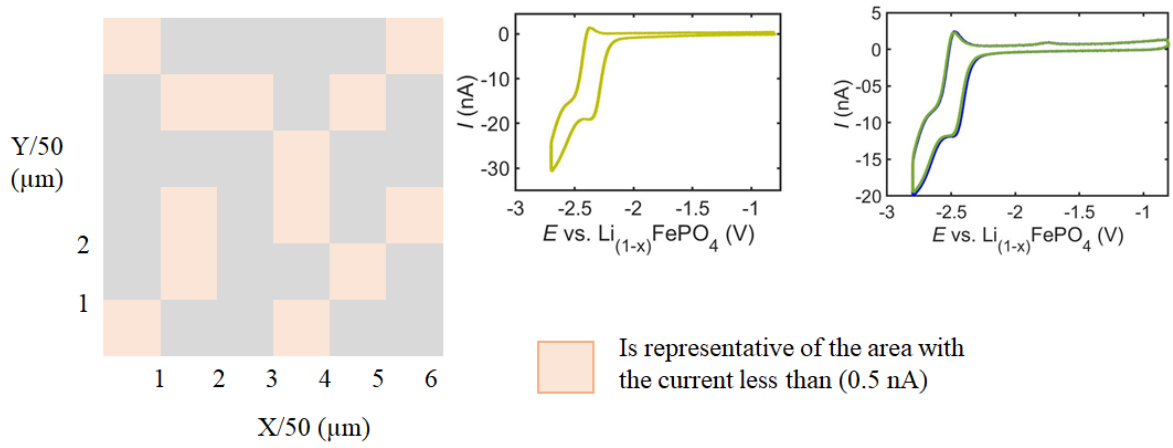

Figure B.2 Map of the surface for a film in the absence of imposed potential. This map was provided using the recorded current at the surface of Pt/Ga microelectrode in the solution of PC and 0.1M $TEABF_4$ as support electrolyte, RE: $Li_{(1-x)}FePO_4$, CE: Ag_xO, scan rate 0.1 V s^{-1} scan range: -0.7 to -2.65 V. Current for the scanned spots were very negligible or near zero and the microelectrode distance to the surface was 2 µm. The examples of the ASV of surface were included to the figure (the right hand).

ASV of the $LiPF_6$ solution in extended cycles

The reproducible response demonstrates the microelectrode stability during the experiment.

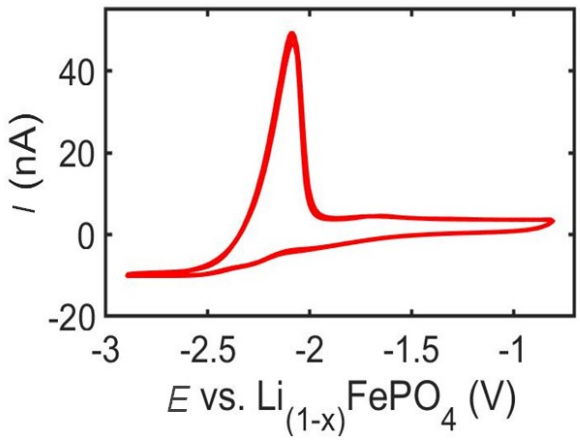

Figure B.3 Stability of Li^+ detection via ASV at a Pt/Ga microelectrode in $LiPF_6$ solution (supporting electrolyte: 0.1 M $TEABF_4$, counter and ref: $Li_{(1-x)}FePO_4$, scan rate: 100 mV/s), 70 overlapping CV cycles of 0.1 mM Li^+.

Challenges for Selection of Redox Mediator

In general, in feedback mode of SECM, a mediator molecule is added to the electrolyte solution. By using this mediator's redox current at the electrode, the distance of the tip to substrate can be determined. Depending on the conductive nature of the substrate (insulator or conducting), the current will decrease or increase as the surface is approached. (Fan et al., 2007; Polcari et al., 2016; Zoski, 2015). Unfortunately, the highly reducing potentials needed for Li plating at the Pt/Ga microelectrode reduces and decomposes the mediator as shown for the two mediators tested here *p*-

benzoquinone (*p*-BQ) and methylviologen dichloride (MV) (Figure B.4). The first cycles in the limited potential range of -0.5 to -1.5 V vs. $Li_{(1-x)}FePO_4$ show reproducibly the S shaped *I* vs. *E* curve associated with a CV dominated by hemispherical diffusion. However as the potential range was expanded to -0.5 to -2.7 V vs. $Li_{(1-x)}FePO_4$ for three cycles, the shape and intensity of the current change between significantly between cycles, indicating degradation. All SECM experiments here were performed in a solution with no mediator.

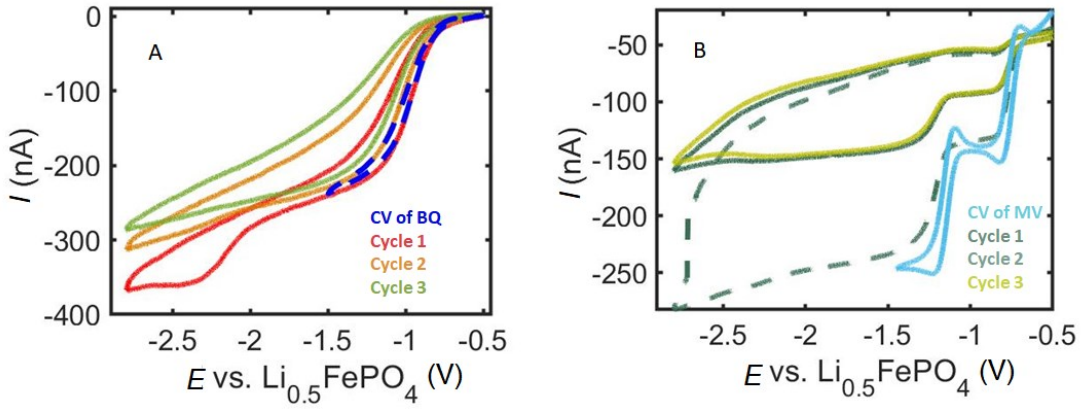

Figure B.4 Non-reproducible electrochemical responses from the solution of 1.0 M p-BQ (A) and MV (B) at Pt/Ga microelectrode in PC. RE, CE: $Li_{(1-x)}FePO_4$, scan rage: -0.5 to -2.7 V Scan rate: 0.1 V s^{-1}.

BIBLIOGRAPHIE

Abollino, O., Giacomino, A. Malandrino, M. (2019). *Voltammetry/Stripping Voltammetry: Encyclopedia of Analytical Science* (p. 238-257) P. Worsfold, C. Poole, A. Townshend & M. Miro,. Oxford: Academic Press. https://dx.doi.org/10.1016/B978-0-12-409547-2.14491-9

Abollino, O., Giacomino, A., Malandrino, M., Piscionieri, G. & Mentasti, E. (2008). Determination of mercury by anodic stripping voltammetry with a gold nanoparticle ‐ modified glassy carbon electrode. *Electroanalysis: An International Journal Devoted to Fundamental and Practical Aspects of Electroanalysis*, *20* (1), 75-83.

Ahmed, S., Nelson, P. A., Gallagher, K. G., Susarla, N. & Dees, D. W. (2017). Cost and energy demand of producing nickel manganese cobalt cathode material for lithium ion batteries. *Journal of Power Sources*, *342*, 733-740.

Aifantis, K. E. (2010). *High energy density lithium batteries: materials, engineering, applications: Next Generation Anodes for Secondary Li-Ion Batteries*(p.129-164) https://dx.doi.org 10.1002/9783527630011.

Aifantis, K. E. & Hackney, S. A. (2010). *High energy density lithium batteries: materials, engineering, applications: Current and potential applications of secondary Li batteries* (p. 81-101) https://dx.doi.org 10.1002/9783527630011.

Aifantis, K. E., Hackney, S. A. & Kumar, R. V. (2010). *High energy density lithium batteries: materials, engineering, applications: A Review of Materials and Chemistry for Secondary Batteries* (p. 53-80) https://dx.doi.org 10.1002/9783527630011.

Allen, D. (2014). *CIRP Encyclopedia of Production Engineering* (p. 483-488). Berlin, Heidelberg : Springer Berlin Heidelberg.

Amatucci, G., Blyr, A., Sigala, C., Alfonse, P. & Tarascon, J. (1997). Surface treatments of $Li_xMn_{(2-x)}O_4$ spinels for improved elevated temperature performance. *Solid State Ionics*, *104* (1-2), 13-25.

Armstrong, A. R. & Bruce, P. G. (1996). Synthesis of layered $LiMnO_2$ as an electrode for rechargeable lithium batteries. *Nature*, *381*(6582), 499-500.

Arrigan, D. W. (2004). Nanoelectrodes, nanoelectrode arrays and their applications. *Analyst*, *129*(12), 1157-1165.

Asanuma, H. & Toshima, N. (2000). *Porous Polymer Complexes for Gas Separations: Membrane Separations: Encyclopedia of Separation Science* (p 3947- 3952).

Atkins, P. W. & De Paula, J. (1998). *Physical chemistry* (p. 250-262). Oxford university press, Oxford UK.

Aurbach, D., Markovsky, B., Shechter, A., Ein‐Eli, Y. & Cohen, H. (1996). A comparative study of synthetic graphite and Li electrodes in electrolyte solutions based on ethylene carbonate‐dimethyl carbonate mixtures. *Journal of The Electrochemical Society*, *143*(12), 3809-3820.

Bachman, J. C., Muy, S., Grimaud, A., Chang, H.-H., Pour, N., Lux, S. F., Lamp, P. (2016). Inorganic solid-state electrolytes for lithium batteries: mechanisms and properties governing ion conduction. *Chemical reviews*, *116*(1), 140-162.

Baldo, M., Daniele, S. & Bragato, C. (2003). *Bismuth film microelectrodes for heavy metals monitoring by anodic stripping voltammetry*, (p.103-107). https://dx.doi.org 10.1051/jp4:20030254.

Banerjee, A., Ziv, B., Luski, S., Aurbach, D. & Halalay, I. C. (2017). Increasing the durability of Li-ion batteries by means of manganese ion trapping materials with nitrogen functionalities. *Journal of Power Sources*, *341*, 457-465.

Baracu, A. M. & Gugoasa, L. A. D. (2021). Recent Advances in Microfabrication, Design and Applications of Amperometric Sensors and Biosensors. *Journal of The Electrochemical Society*.

Bard, A. J., Fan, F. R. F., Kwak, J. & Lev, O. (1989). Scanning electrochemical microscopy. Introduction and principles. *Analytical Chemistry*, *61*(2), 132-138.

Bard, A. J. & Faulkner, L. R. (1983). Electrochemical methods fundamentals and applications. *Surface Technology*, *20* (1), 91-92.

Bard, A. J. & Faulkner, L. R. (2001). Fundamentals and applications. *Electrochemical methods*, *2*(482), 580-632.

Barker, J., Saidi, M. & Swoyer, J. (2003). Electrochemical insertion properties of the novel lithium vanadium fluorophosphate, LiVPO4 F. *Journal of the Electrochemical Society*, *150*(10), A1394-A1398.

Barton, Z. J. & Rodríguez-López, J. (2014). Lithium ion quantification using mercury amalgams as in situ electrochemical probes in nonaqueous media. *Analytical chemistry*, *86*(21), 10660-10667.

Batista Deroco, P., Giarola, J. d. F., Wachholz Júnior, D., Arantes Lorga, G. & Tatsuo Kubota, L. (2020). electrochemical sensing devices: *Comprehensive Analytical Chemistry* (p. 91-137). Elsevier.

Bekaert, E., Buannic, L., Lassi, U., Llordés, A. & Salminen, J. (2017). *Electrolytes for Li-and Na-ion batteries: concepts, candidates, and the role of nanotechnology. Emerging Nanotechnologies in Rechargeable Energy Storage Systems* (p. 1-43). Elsevier. https://dx.doi.org 10.1016/B978-0-323-42977-1.00001-7.

Bergner, S., Vatsyayan, P. & Matysik, F.-M. (2013). Recent advances in high resolution scanning electrochemical microscopy of living cells–a review. *Analytica chimica acta*, *775*, 1-13.

Besenhard, J., Winter, M., Yang, J. & Biberacher, W. (1995). Filming mechanism of lithium-carbon anodes in organic and inorganic electrolytes. *Journal of Power Sources*, *54*(2), 228-231.

Blair, S. M., Brodbelt, J. S., Marchand, A. P., Chong, H.-S. & Alihodžić, S. (2000). Evaluation of alkali metal binding selectivities of caged aza-crown ether ligands by microelectrospray ionization/quadrupole ion trap mass spectrometry. *Journal of the American Society for Mass Spectrometry*, *11*(10), 884-891.

Blomgren, G. E. (2016). The development and future of lithium ion batteries. *Journal of The Electrochemical Society*, *164*(1), A5019.

Brendel, P. J. & Luther, G. W., (1995, 1995/03/01). Development of a Gold Amalgam Voltammetric Microelectrode for the Determination of Dissolved Fe, Mn, O_2 in Porewaters of Marine and Freshwater Sediments. *Environmental Science & Technology*, *29*(3), 751-761. https://dx.doi.org 10.1021/es00003a024

Brownlee, B. J., Claussen, J. C. & Iverson, B. D. (2020). 3D Interdigitated Vertically Aligned Carbon Nanotube Electrodes for Electrochemical Impedimetric Biosensing. *ACS Applied Nano Materials*, *3*(10), 10166-10175.

Cai, C., Liu, B., Mirkin, M. V., Frank, H. A. & Rusling, J. F. (2002). Scanning electrochemical microscopy of living cells. 3. Rhodobacter s phaeroides. *Analytical chemistry*, *74*(1), 114-119.

Chan, H., Duh, J. & Sheen, S. (2003). LiMn2O4 cathode doped with excess lithium and synthesized by co-precipitation for Li-ion batteries. *Journal of power sources*, *115*(1), 110-118.

Chen, A. & Shah, B. (2013). Electrochemical sensing and biosensing based on square wave voltammetry. *Analytical Methods*, *5*(9), 2158-2173.

Chen, F., Yang, D., Zha, W., Zhu, B., Zhang, Y., Li, J., Sadoway, D. R. (2017). Solid polymer electrolytes incorporating cubic $Li_7La_3Zr_2O_{12}$ for all solid state lithium rechargeable batteries. *Electrochimica Acta*, *258*, 1106-1114.

Chen, L., Liu, T. & Ma, C. a. (2010). Metal complexation and biodegradation of EDTA and S, S-EDDS: a density functional theory study. *The Journal of Physical Chemistry A*, *114*(1), 443-454.

Chen Legrand, D., Barus, C. & Garçon, V. (2017). Square wave voltammetry measurements of low concentrations of nitrate using Au/AgNPs electrode in chloride solutions. *Electroanalysis*, *29*(12), 2882-2887.

Chen, Z., Belharouak, I., Sun, Y. K. & Amine, K. (2013). Titanium based anode materials for safe lithium ion batteries. *Advanced Functional Materials*, *23*(8), 959-969.

Chhin, D., Hossain, M. S. & Schougaard, S. B. (2020). 14. Modeling of Lithium-Ion Batteries. *Advanced Materials* (p. 353-388). https://doi.org/10.1515/9783110537734.

Chiechi, R. C., Weiss, E. A., Dickey, M. D. & Whitesides, G. M. (2008). Eutectic galliu ‐ indium (EGaIn): a moldable liquid metal for electrical characterization of self assembled monolayers. *Angewandte Chemie International Edition*, *47*(1), 142-144.

Cho, J., Kim, Y. J., Kim, T. J. & Park, B. (2001). Zero strain intercalation cathode for rechargeable Li Ion cell. *Angewandte Chemie International Edition*, *40*(18), 3367-3369.

Coetzee, J. & Ecoff, M. (1991). Potentiometric stripping analysis at microelectrodes in various solvents and some comparisons with voltammetric stripping analysis. *Analytical chemistry*, *63*(10), 957-963.

Creighton, J. & Withnall, R. (2000). The Raman spectrum of gallium metal. *Chemical Physics Letters*, *326*(3-4), 311-313.

Csoka, B. & Mekhalif, Z. (2009). Carbon paste-based ion-selective dual function microelectrodes for SECM measurements. *Electrochimica acta*, *54*(11), 3225-3232.

Cui, X., Tuo, K., Xie, Y., Li, C., Zhao, D., Yang, L., Li, S. (2020). Investigation on electrochemical performance at the low temperature of LFP/CP composite based on phosphorus doping carbon network. *Ionics*, *26*(8), 3795-3808.

Daniel, C., Mohanty, D., Li, J. & Wood, D. L. (2014). *Cathode materials review*, *vol. 1597*. American Institute of Physics.

Daniele, S. (2005). VOLTAMMETRY/Anodic Stripping. P. Worsfold, A. Townshend & C. Poole (dir.), *Encyclopedia of Analytical Science (Second Edition)* (p. 197-203). Oxford : Elsevier.

Daniele, S., Baldo, M. A., Ugo, P. & Mazzocchin, G. A. (1989). Determination of heavy metals in real samples by anodic stripping voltammetry with mercury microelectrodes: Part 1. Application to wine. *Analytica Chimica Acta*, *219*, 9-18.

Daniele, S., Bragato, C., Baldo, M. A. & Ciani, I. (2008). Application of thin-shielded mercury microelectrodes in anodic stripping voltammetry. *Talanta*, *77*(1), 235-240.

Daniele, S., Bragato, C., Ciani, I. & Baldo, M. A. (2003). Sphere Cap Mercury Microelectrodes for Scanning Electrochemical Microscopy Above an Insulating Substrate. *Electroanalysis: An International Journal Devoted to Fundamental and Practical Aspects of Electroanalysis*, *15*(7), 621-628.

Danis, L., Gateman, S. M., Snowden, M. E., Halalay, I. C., Howe, J. Y. & Mauzeroll, J. (2015). Anodic stripping voltammetry at nanoelectrodes: trapping of Mn^{2+} by crown ethers. *Electrochimica Acta*, *162*, 169-175.

Danis, L., Polcari, D., Kwan, A., Gateman, S. M. & Mauzeroll, J. (2015). Fabrication of carbon, gold, platinum, silver, and mercury ultramicroelectrodes with controlled geometry. *Analytical chemistry*, *87*(5), 2565-2569.

Dayeh, M., Ghavidel, M. Z., Mauzeroll, J. & Schougaard, S. B. (2019). Micropipette Contact Method to Investigate High Energy Cathode Materials by using an Ionic Liquid. *ChemElectroChem*, *6*(1), 195-201.

De Picciotto, L., Thackeray, M., David, W., Bruce, P. & Goodenough, J. B. (1984). Structural characterization of delithiated LiVO2. *Materials research bulletin*, *19*(11), 1497-1506.

Deng, D. (2015). Li ion batteries: basics, progress, and challenges. *Energy Science & Engineering*, *3*(5), 385-418.

Diaw, M., Chagnes, A., Carre, B., Willmann, P. Lemordant, D. (2005). Mixed ionic liquid as electrolyte for lithium batteries. *Journal of power sources*, *146*(1-2), 682-684.

Dimov, N., Xia, Y. & Yoshio, M. (2007). Practical silicon-based composite anodes for lithium-ion batteries: fundamental and technological features. *Journal of power sources*, *171*(2), 886-893.

Diouf, B. & Pode, R. (2015). Potential of lithium-ion batteries in renewable energy. *Renewable Energy*, *76*, 375-380.

Doughty, D. H. & Roth, E. P. (2012). A general discussion of Li ion battery safety. *The Electrochemical Society Interface*, *21*(2), 37-44.

Dunn, B., Kamath, H. & Tarascon, J. M. (2011). Electrical energy storage for the grid: a battery of choices. *Science*, *334*(6058), 928-935.

EC08, A. A. N. (2011). Basic overview of the working principle of a potentiostat/galvanostat (PGSTAT)–Electrochemical cell setup. *Metrohm Autolab. BV*, 1-3.

Eckhard, K., Chen, X., Turcu, F. & Schuhmann, W. (2006). Redox competition mode of scanning electrochemical microscopy (RC-SECM) for visualisation of local catalytic activity. *physical chemistry chemical physics*, *8*(45), 5359-5365.

Economou, A. & Fielden, P. (2003). Mercury film electrodes: developments, trends and potentialities for electroanalysis. *Analyst*, *128*(3), 205-213.

Energy, USA Energy Department (2017). *How Do Hybrid Electric Cars Work?* https://afdc.energy.gov/vehicles/how-do-hybrid-electric-cars-work

Engstrom, R. C. & Pharr, C. M. (1989). Scanning electrochemical microscopy. *Analytical Chemistry*, *61*(19), 1099A-1104A.

Etacheri, V., Marom, R., Elazari, R., Salitra, G. & Aurbach, D. (2011). Challenges in the development of advanced Li ion batteries: a review. *Energy & Environmental Science*, *4*(9), 3243-3262.

Fan, F. R. F., Liu, B. & Mauzeroll, J. (2007). Scanning electrochemical microscopy. *Handbook of electrochemistry* (p. 471-540). Elsevier.

Fang, H., Pan, Z., Li, L., Yang, Y., Yan, G., Li, G. & Wei, S. (2008). The possibility of manganese disorder in $LiMnPO_4$ and its effect on the electrochemical activity. *Electrochemistry communications*, *10*(7), 1071-1073.

Flamme, B., Garcia, G. R., Weil, M., Haddad, M., Phansavath, P., Ratovelomanana-Vidal, V. & Chagnes, A. (2017). Guidelines to design organic electrolytes for lithium-ion batteries: environmental impact, physicochemical and electrochemical properties. *Green Chemistry*, *19*(8), 1828-1849.

Fong, R., Von Sacken, U. & Dahn, J. R. (1990). Studies of lithium intercalation into carbons using nonaqueous electrochemical cells. *Journal of The Electrochemical Society*, *137*(7), 2009.

Forster, R. J. & Keyes, T. E. (2007). Ultramicroelectrodes. *Handbook of Electrochemistry* (p. 155-171). Elsevier.

Fritsch, S. & Navrotsky, A. (1996). Thermodynamic properties of manganese oxides. *Journal of the American Ceramic Society*, *79*(7), 1761-1768.

Gamry Instrument, I. (2015). *potentiostat fundamentals*. https://www.gamry.com/

Gherab, K., Al-Douri, Y., Hashim, U., Ameri, M., Bouhemadou, A., Batoo, K. M., Raslan, E. H. (2020). Fabrication and characterizations of Al nanoparticles doped ZnO nanostructures-based integrated electrochemical biosensor. *Journal of Materials Research and Technology*, *9*(1), 857-867.

Goodenough, J. & Mizuchima, K. (1981). *Electrochemical cell with new fast ion conductors* (patent).

Greenwood, N. N. & Earnshaw, A. (2012). *Chemistry of the Elements* Elsevier.

Gu, M., Belharouak, I., Zheng, J., Wu, H., Xiao, J., Genc, A., Zhang, J. G. (2013). Formation of the spinel phase in the layered composite cathode used in Li-ion batteries. *ACS nano*, *7*(1), 760-767.

Gu, Y., Fang, S., Yang, L. & Hirano, S.-i. (2021). A non-flammable electrolyte for long-life lithium ion batteries operating over a wide-temperature range. *Journal of Materials Chemistry A*.

Gummow, R., De Kock, A. & Thackeray, M. (1994). Improved capacity retention in rechargeable 4 V lithium/lithium-manganese oxide (spinel) cells. *Solid State Ionics*, *69*(1), 59-67.

Guyomard, D. & Tarascon, J. (1995). High voltage stable liquid electrolytes for $Li_{1+x}Mn_2O_4$/carbon rocking-chair lithium batteries. *Journal of Power Sources*, *54*(1), 92-98.

Han, L., Lehmann, M. L., Zhu, J., Liu, T., Zhou, Z., Tang, X., Chen, X. C. (2020). Recent Developments and Challenges in Hybrid Solid Electrolytes for Lithium-Ion Batteries. *Frontiers in Energy Research*, *8*, 202.

Hassan, S. A., ElDin, N. B., Zaazaa, H. E., Moustafa, A. A. & Mahmoud, A. M. (2020). Point-of-care diagnostics for drugs of abuse in biological fluids: application of a microfabricated disposable copper potentiometric sensor. *Microchimica Acta*, *187*(9), 1-9.

He, G., Li, Q., Shen, Y. & Ding, Y. (2019). Flexible amalgam film enables stable lithium metal anodes with high capacities. *Angewandte Chemie International Edition*, *58*(51), 18466-18470.

He, X., Ni, Y., Hou, Y., Lu, Y., Jin, S., Li, H., Chen, J. (2021). Insights into the Ionic Conduction Mechanism of Quasi‐Solid Polymer Electrolytes through Multispectral Characterization. *Angewandte Chemie International Edition*, *60*(42), 22672-22677.

Heiskanen, S. K., Kim, J. & Lucht, B. L. (2019). Generation and evolution of the solid electrolyte interphase of lithium-ion batteries. *Joule*, *3*(10), 2322-2333.

Horrocks, B. R., Mirkin, M. V., Pierce, D. T., Bard, A. J., Nagy, G. & Toth, K. (1993). Scanning electrochemical microscopy. 19. Ion-selective potentiometric microscopy. *Analytical Chemistry*, *65*(9), 1213-1224.

Hossain, M. S., Stephens, L. I., Hatami, M., Ghavidel, M., Chhin, D., Dawkins, J. I., Schougaard, S. B. (2019). Effective mass transport properties in lithium battery electrodes. *ACS Applied Energy Materials*, *3*(1), 440-446.

Houde. (2019). *Developing a promising sector for Quebec's economy*. https://propulsionquebec.com/en/

Howell, J. O. & Wightman, R. M. (1984). Ultrafast voltammetry and voltammetry in highly resistive solutions with microvoltammetric electrodes. *Analytical Chemistry*, *56*(3), 524-529.

Hu, Y., Li, H., Huang, X. & Chen, L. (2004). Novel room temperature molten salt electrolyte based on LiTFSI and acetamide for lithium batteries. *Electrochemistry communications*, *6*(1), 28-32.

Huang, L., Li, Z., Lou, Y., Cao, F., Zhang, D. & Li, X. (2018). Recent advances in scanning electrochemical microscopy for biological applications. *Materials*, *11*(8), 1389.

Illuminati, S., Annibaldi, A., Truzzi, C., Libani, G., Mantini, C. & Scarponi, G. (2015). Determination of water-soluble, acid-extractable and inert fractions of Cd, Pb and Cu in Antarctic aerosol by square wave anodic stripping voltammetry after sequential extraction and microwave digestion. *Journal of Electroanalytical Chemistry*, *755*, 182-196.

Inada, T., Kobayashi, T., Sonoyama, N., Yamada, A., Kondo, S., Nagao, M. & Kanno, R. (2009). All solid-state sheet battery using lithium inorganic solid electrolyte, thio-LISICON. *Journal of Power Sources*, *194*(2), 1085-1088.

Inokuchi, Y., Boyarkin, O. V., Kusaka, R., Haino, T., Ebata, T. & Rizzo, T. R. (2012). Ion selectivity of crown ethers investigated by UV and IR spectroscopy in a cold ion trap. *The Journal of Physical Chemistry A*, *116*(16), 4057-4068.

Inzelt, G. (2013). Pseudo-reference electrodes. *Handbook of Reference Electrodes* (p. 331-332). Springer.

Jang, Y. I., Huang, B., Chiang, Y. M. & Sadoway, D. R. (1998). Stabilization of LiMnO2 in the α - NaFeO2 Structure Type by LiAlO2 Addition. *Electrochemical and Solid State Letters*, *1*(1), 13.

Jiang, F. & Peng, P. (2016). Elucidating the performance limitations of lithium-ion batteries due to species and charge transport through five characteristic parameters. *Scientific reports*, *6*, 32639.

Johnson, C. S. (2007). Development and utility of manganese oxides as cathodes in lithium batteries. *Journal of Power Sources*, *165*(2), 559-565.

Jothimuthu, P., Wilson, R. A., Herren, J., Pei, X., Kang, W., Daniels, R., Papautsky, I. (2013). Zinc detection in serum by anodic stripping voltammetry on microfabricated bismuth electrodes. *Electroanalysis*, *25*(2), 401-407.

Kempaiah, R., Vasudevamurthy, G. & Subramanian, A. (2019). Scanning probe microscopy based characterization of battery materials, interfaces, and processes. *Nano Energy*, *65*, 103925. Doi: https://doi.org/10.1016/j.nanoen.2019.103925

Kerr, T., Gaubicher, J. & Nazar, L. (2000). Highly Reversible Li Insertion at 4 V in ε -$VOPO_4$/ α -$LiVOPO_4$ Cathodes. *Electrochemical and Solid-State Letters*, *3*(10), 460-462.

Kia, A., Wong, H. S. & Cheeseman, C. R. (2017, 2017/05/15/). Clogging in permeable concrete: A review. *Journal of Environmental Management*, *193*, 221-233. Doi: https://doi.org/10.1016/j.jenvman.2017.02.018

Klett, M., Giesecke, M., Nyman, A., Hallberg, F., Lindström, R. W., Lindbergh, G. r. & Furó, I. n. (2012). Quantifying mass transport during polarization in a Li ion battery electrolyte by *in situ* ^{7}Li NMR imaging. *Journal of the American Chemical Society*, *134*(36), 14654-14657.

Klusmann, E. & Schultze, J. (1997). pH-microscopy theoretical and experimental investigations. *Electrochimica acta*, *42*(20-22), 3123-3134.

Kounaves, S. P. (1997). *Voltammetric techniques* (pp. 709-726) : Prentice Hall, Upper Saddle River, NJ, USA.

Lee, M. J., Lee, S., Oh, P., Kim, Y. & Cho, J. (2014). High performance $LiMn_2O_4$ cathode materials grown with epitaxial layered nanostructure for Li-ion batteries. *Nano letters*, *14*(2), 993-999.

Lefrou, C. & Cornut, R. (2010). Analytical expressions for quantitative scanning electrochemical microscopy (SECM). *ChemPhysChem*, *11*(3), 547-556.

Lepage, D., Michot, C., Liang, G., Gauthier, M. & Schougaard, S. B. (2011). A soft chemistry approach to coating of LiFePO4 with a conducting polymer. *Angewandte Chemie*, *123*(30), 7016-7019.

Lepage, D., Savignac, L., Saulnier, M., Gervais, S. & Schougaard, S. (2019). Modification of aluminum current collectors with a conductive polymer for application in lithium batteries. *Electrochemistry Communications*, *102*, 1-4.

Leslie, R. V. (2018). 1.16 - Microwave Sensors. S. Liang, *Comprehensive Remote Sensing* (p. 435-474). Oxford , Elsevier.

Li, M., Lu, J., Chen, Z. & Amine, K. (2018). 30 years of lithium‐ion batteries. *Advanced Materials*, *30*(33), 1800561.

Liang, R. f., Wang, Z. x., Guo, H.-j., Li, X.-h., Peng, W. j. & Wang, Z.g. (2008). Fabrication and electrochemical properties of lithium-ion batteries for power tools. *Journal of Power Sources*, *184*(2), 598-603.

Liang, S., Li, X. & Wang, J. (2012). A systematic view of remote sensing. *Advanced remote sensing*, 1-31.

Lipson, A. L., Ginder, R. S. & Hersam, M. C. (2011). Nanoscale in situ characterization of li‐ion battery electrochemistry via scanning ion conductance microscopy. *Advanced Materials*, *23*(47), 5613-5617.

Lipson, A. L. & Hersam, M. C. (2013, 2013/04/25). Conductive Scanning Probe Characterization and Nanopatterning of Electronic and Energy Materials. *The Journal of Physical Chemistry C*, *117*(16), 7953-7963. Doi: 10.1021/jp312594s

Liu, Q., Wang, S., Tan, H., Yang, Z. & Zeng, J. (2013). Preparation and doping mode of doped $LiMn_2O_4$ for Li-ion batteries. *Energies*, *6*(3), 1718-1730.

Long, G. L. & Winefordner, J. D. (1983). Limit of detection. A closer look at the IUPAC definition. *Analytical chemistry*, *55*(7), 712A-724A.

Longobardi, F., Cosma, P., Milano, F., Agostiano, A., Mauzeroll, J. & Bard, A. J. (2006). Scanning electrochemical microscopy of the photosynthetic reaction center of Rhodobacter sphaeroides in different environmental systems. *Analytical chemistry*, *78*(14), 5046-5051.

Manthiram, A. (2020). A reflection on lithium-ion battery cathode chemistry. *Nature Communications*, *11*(1), 1-9.

Mauzeroll, J. (2007). Hg microhemispherical electrodes. *Handbook of Electrochemistry* (p. 235-243). Elsevier.

Mauzeroll, J., Hueske, E. A. & Bard, A. J. (2003). Scanning electrochemical microscopy. 48. Hg/Pt hemispherical ultramicroelectrodes: fabrication and characterization. *Analytical chemistry*, *75*(15), 3880-3889.

McNaught, A. D. & Wilkinson, A. (1997). *Compendium of chemical terminology* (vol. 1669) Blackwell Science Oxford.

Megahed, S. & Scrosati, B. (1994). Lithium-ion rechargeable batteries. *Journal of Power Sources*, *51*(1-2), 79-104.

Mei, Y., Huang, Y. & Hu, X. (2016). Nanostructured Ti-based anode materials for Na-ion batteries. *Journal of Materials Chemistry A*, *4*(31), 12001-12013.

Meyer, W. H. (1998). Polymer electrolytes for lithium-ion batteries. *Advanced materials*, *10*(6), 439-448.

Mezour, M. A., Morin, M. & Mauzeroll, J. (2011). Fabrication and characterization of laser pulled platinum microelectrodes with controlled geometry. *Analytical chemistry*, *83*(6), 2378-2382.

Mirceski, V., Skrzypek, S. & Stojanov, L. (2018). Square-wave voltammetry. *ChemTexts*, *4*(4), 1-14.

Mirkin, M. V. & Horrocks, B. R. (2000). Electroanalytical measurements using the scanning electrochemical microscope. *Analytica Chimica Acta*, *406*(2), 119-146.

Mirzaeian, M., Abbas, Q., Hunt, M. R. C., Galeyeva, A. & Raza, R. (2022). Na-Ion Batteries. A.-G. Olabi (dir.), *Encyclopedia of Smart Materials* (p. 135-147). Oxford : Elsevier.

Mizushima, K., Jones, P., Wiseman, P. & Goodenough, J. B. (1980). Li_xCoO_2 ($0< x<-1$): A new cathode material for batteries of high energy density. *Materials Research Bulletin*, *15*(6), 783-789.

Mizushima, K., Jones, P., Wiseman, P. & Goodenough, J. B. (1981). Li_xCoO_2 ($0< x\leqslant 1$): A new cathode material for batteries of high energy density. *Solid State Ionics*, *3*, 171-174.

Morkvėnaitė-Vilkončienė, I., Petkevičius, S., Keraitė, G., Šakalys, P. & Lenkutis, T. (2017). Positioning and control of scanning electrochemical microscopy. *Mokslas–Lietuvos ateitis/Science–Future of Lithuania*, *9*(6), 602-606.

Moser, Z. & Guminski, C. (1993). Hg-mn (mercury-manganese) system. *Journal of phase equilibria*, *14*(6), 726-733.

Moyna, Á., Connolly, D., Nesterenko, E., Nesterenko, P. N. & Paull, B. (2013). Iminodiacetic acid functionalised organopolymer monoliths: Application to the

separation of metal cations by capillary high-performance chelation ion chromatography. *Analytical and bioanalytical chemistry*, *405*(7), 2207-2217.

Mueller, T., Hautier, G., Jain, A. & Ceder, G. (2011). Evaluation of tavorite-structured cathode materials for lithium-ion batteries using high-throughput computing. *Chemistry of materials*, *23*(17), 3854-3862.

Murphy, D. & Christian, P. (1979). Solid state electrodes for high energy batteries. *Science*, *205*(4407), 651-656.

Musil, M. & Vondrák, J. (2014). Transference Number Measurements on Gel Polymer Electrolytes for Lithium-Ion Batteries. *ECS Transactions*, *63*(1), 315.

Nanjundaswamy, K., Padhi, A., Goodenough, J. B., Okada, S., Ohtsuka, H., Arai, H. & Yamaki, J. (1996). Synthesis, redox potential evaluation and electrochemical characteristics of NASICON-related-3D framework compounds. *Solid State Ionics*, *92*(1-2), 1-10.

Nazarov, V. A., Taryba, M. G., Zdrachek, E. A., Andronchyk, K. A., Egorov, V. V. & Lamaka, S. V. (2013). Sodium-and chloride-selective microelectrodes optimized for corrosion studies. *Journal of Electroanalytical Chemistry*, *706*, 13-24.

Nazri, G.-A. & Pistoia, G. (2008). *Lithium batteries: science and technology* Springer Science & Business Media.

Nebel, M., Grützke, S., Diab, N., Schulte, A. & Schuhmann, W. (2013). Microelectrochemical visualization of oxygen consumption of single living cells. *Faraday discussions*, *164*, 19-32.

Newman, J. & Thomas-Alyea, K. E. (2012). *Electrochemical systems* John Wiley & Sons.

Nitta, N., Wu, F., Lee, J. T. & Yushin, G. (2015). Li-ion battery materials: present and future. *Materials today*, *18*(5), 252-264.

Nyman, A. (2011). *An experimental and theoretical study of the mass transport in lithium-ion battery electrolytes*. KTH (dissertation).

Padhi, A., Nanjundaswamy, K., Masquelier, C., Okada, S. & Goodenough, J. B. (1997). Effect of structure on the Fe^{3+}/Fe^{2+} redox couple in iron phosphates. *Journal of the Electrochemical Society*, *144*(5), 1609.

Panascikaite, E. & Armalis, S. (2011). Determination of manganese in drinking water by anodic stripping voltammetry at a mercury film electrode. *Chemija*, *22*(1), 41-45.

Payne, N. A., Dawkins, J. I., Schougaard, S. B. & Mauzeroll, J. (2019). Effect of Substrate Permeability on Scanning Ion Conductance Microscopy: Uncertainty in Tip–Substrate Separation and Determination of Ionic Conductivity. *Analytical chemistry*, *91*(24), 15718-15725.

Pei, X., Kang, W., Yue, W., Bange, A., Heineman, W. R. & Papautsky, I. (2014). Improving reproducibility of lab-on-a-chip sensor with bismuth working electrode for determining Zn in serum by anodic stripping voltammetry. *Journal of the Electrochemical Society*, *161*(2), B3160.

Poizot, P., Laruelle, S., Grugeon, S., Dupont, L. & Tarascon, J. (2000). Nano-sized transition-metal oxides as negative-electrode materials for lithium-ion batteries. *Nature*, *407*(6803), 496.

Polcari, D., Dauphin-Ducharme, P. & Mauzeroll, J. (2016). Scanning electrochemical microscopy: a comprehensive review of experimental parameters from 1989 to 2015. *Chemical reviews*, *116*(22), 13234-13278.

Princeton. (2010) *Square Wave Voltammetry*. https://www.ameteksi.com/brands/princeton-applied-research

Pust, S. E., Maier, W. & Wittstock, G. (2008). Investigation of localized catalytic and electrocatalytic processes and corrosion reactions with scanning

electrochemical microscopy (SECM). *Zeitschrift für Physikalische Chemie*, *222*(10), 1463-1517.

Qiao, H. & Wei, Q. (2012). 10 - Functional nanofibers in lithium-ion batteries. Q. Wei, *Functional Nanofibers and their Applications* (p. 197-208). Woodhead Publishing.

Rahn, C. D. & Wang, C.Y. (2013). *Battery systems engineering* John Wiley & Sons.

Rao, B., Francis, R. & Christopher, H. (1977). Lithium- aluminum electrode. *Journal of The Electrochemical Society*, *124*(10), 1490.

Razak, M. R., Yusof, N. A., Haron, M. J., Ibrahim, N., Mohammad, F., Kamaruzaman, S. & Al-Lohedan, H. A. (2018). Iminodiacetic acid modified kenaf fiber for waste water treatment. *International journal of biological macromolecules*, *112*, 754-760.

Reddy, M. A., Pralong, V., Caignaert, V., Varadaraju, U. & Raveau, B. (2009). Monoclinic iron hydroxy sulphate: A new route to electrode materials. *Electrochemistry Communications*, *11*(9), 1807-1810.

Reducks. (2020) *New Potentiostathttps://pineresearch.com/blog/new-wavenow-wireless*

Rudolph, D., Neuhuber, S., Kranz, C., Taillefert, M. Mizaikoff, B. (2004). Scanning electrochemical microscopy imaging of rhodochrosite dissolution using gold amalgam microelectrodes. *Analyst*, *129*(5), 443-448.

Ryssdal. (2016). How an oil shortage in the 1970s shaped today's economic policy.

Saulnier, M., Auclair, A., Liang, G. & Schougaard, S. (2016). Manganese dissolution in lithium-ion positive electrode materials. *Solid State Ionics*, *294*, 1-5.

Schmuch, R., Wagner, R., Hörpel, G., Placke, T. & Winter, M. (2018). Performance and cost of materials for lithium-based rechargeable automotive batteries. *Nature Energy*, *3*(4), 267-278.

Schwamborn, S., Stoica, L., Chen, X., Xia, W., Kundu, S., Muhler, M. & Schuhmann, W. (2010). Patterned CNT arrays for the evaluation of oxygen reduction activity by SECM. *ChemPhysChem*, *11*(1), 74-78.

Scott, I. D., Jung, Y. S., Cavanagh, A. S., Yan, Y., Dillon, A. C., George, S. M. & Lee, S.-H. (2011). Ultrathin coatings on nano-$LiCoO_2$ for Li-ion vehicular applications. *Nano letters*, *11*(2), 414-418.

Scrosati, B. (2000). Recent advances in lithium ion battery materials. *Electrochimica Acta*, *45*(15-16), 2461-2466.

Scrosati, B. (2011). History of lithium batteries. *Journal of solid state electrochemistry*, *15*(7-8), 1623-1630.

Semeraro, C., Olabi, A.-G. & Dassisti, M. (2022). Sustainability Issues in Manufacturing and Operation of Second-Generation Flow Batteries. A.-G. Olabi (dir.), *Encyclopedia of Smart Materials* (p. 192-197). Oxford : Elsevier.

Serrapede, M., Denuault, G., Sosna, M., Pesce, G. L. & Ball, R. J. (2013). Scanning electrochemical microscopy: using the potentiometric mode of SECM to study the mixed potential arising from two independent redox processes. *Analytical chemistry*, *85*(17), 8341-8346.

She, D. & Allen, M. G. (2019). A micromachined freestanding electrochemical sensor for measuring dissolved oxygen. *Journal of Microelectromechanical Systems*, *28*(3), 521-531.

Shu, Z., McMillan, R. & Murray, J. (1993). Electrochemical intercalation of lithium into graphite. *Journal of The Electrochemical Society*, *140*(4), 922-924.

Shukla, R. P., Rapier, C., Glassman, M., Liu, F., Kelly, D. L. & Ben-Yoav, H. (2020). An integrated electrochemical microsystem for real-time treatment monitoring of clozapine in microliter volume samples from schizophrenia patients. *Electrochemistry Communications*, *120*(3), 106850.

Simões, F. R. & Xavier, M. G. (2017). *Electrochemical sensors. Nanoscience and its Applications*, (p.155-178).

Snowden, M. E., Dayeh, M., Payne, N. A., Gervais, S., Mauzeroll, J. & Schougaard, S. B. (2016). Measurement on isolated lithium iron phosphate particles reveals heterogeneity in material properties distribution. *Journal of Power Sources*, *325*(1), 682-689.

Souto, R. M., González-García, Y., Battistel, D. & Daniele, S. (2012). In situ scanning electrochemical microscopy (SECM) detection of metal dissolution during zinc corrosion by means of mercury sphere-cap microelectrode tips.

Stephenson, D. E., Hartman, E. M., Harb, J. N. & Wheeler, D. R. (2007). Modeling of particle-particle interactions in porous cathodes for lithium-ion batteries. *Journal of the Electrochemical Society*, *154*(12), 1146-1148.

Stulík, K., Amatore, C., Holub, K., Marecek, V. & Kutner, W. (2000). Microelectrodes. Definitions, characterization, and applications (Technical report). *Pure and Applied Chemistry*, *72*(8), 1483-1492.

Suzuki, Y., Fukunaka, Y. & Goto, T. (2019). Interfacial phenomena associated with Li electrodeposition on liquid Ga substrates in propylene carbonate. *Electrochemistry Communications*, *100*, 20-25.

Takahashi, Y., Shevchuk, A. I., Novak, P., Murakami, Y., Shiku, H., Korchev, Y. E. & Matsue, T. (2010, 2010/07/28). Simultaneous Noncontact Topography and Electrochemical Imaging by SECM/SICM Featuring Ion Current Feedback Regulation. *Journal of the American Chemical Society*, *132*(29), 10118-10126.

Tarascon, J.M. (2010). Is lithium the new gold? *Nature chemistry*, *2*(6), 510-510.

Tarascon, J., Coowar, F., Amatuci, G., Shokoohi, F. & Guyomard, D. (1995). The Li $_x$$Mn_2O_4C$ system Materials and electrochemical aspects. *Journal of power sources*, *54*(1), 103-108.

Tarascon, J., McKinnon, W., Coowar, F., Bowmer, T., Amatucci, G. & Guyomard, D. (1994). Synthesis conditions and oxygen stoichiometry effects on Li insertion into the spinel $LiMn_2O_4$. *Journal of The Electrochemical Society*, *141*(6), 1421.

Tasaki, K., Goldberg, A., Lian, J. J., Walker, M., Timmons, A. & Harris, S. J. (2009). Solubility of lithium salts formed on the lithium-ion battery negative electrode surface in organic solvents. *Journal of The Electrochemical Society*, *156*(12), 1019-1027.

Thackeray, M., De Kock, A., Rossouw, M., Liles, D., Bittihn, R. & Hoge, D. (1992). Spinel electrodes from the Li-Mn-O system for rechargeable lithium battery applications. *Journal of the Electrochemical Society*, *139*(2), 363-368.

Thackeray, M., Johnson, P., Picciotto, L., Bruce, P. & Goodenough, J. (1984). Electrochemical extraction of lithium from LiMn2O4. *Materials Research Bulletin*, *19*(2), 179-187.

Tomaszewska, A., Chu, Z., Feng, X., O'Kane, S., Liu, X., Chen, J., Liu, L. (2019). Lithium-ion battery fast charging: A review. *ETransportation*, *1*(1), 100011.

Tsunekawa, H., Narumi, A., Sano, M., Hiwara, A., Fujita, M. & Yokoyama, H. (2003). Solvation and ion association studies of $LiBF_4$-propylenecarbonate and $LiBF_4$−propylenecarbonate−trimethyl phosphate solutions. *The Journal of Physical Chemistry B*, *107*(39), 10962-10966.

Tyunina, E. Y., Afanasiev, V. N. & Chekunova, M. D. (2011). Electroconductivity of tetraethylammonium tetrafluoroborate in propylene carbonate at various temperatures. *Journal of Chemical & Engineering Data*, *56*(7), 3222-3226.

Varzi, A., Raccichini, R., Passerini, S. & Scrosati, B. (2016). Challenges and prospects of the role of solid electrolytes in the revitalization of lithium metal batteries. *Journal of Materials Chemistry A*, *4*(44), 17251-17259.

Venton, B. J. & DiScenza, D. J. (2020). Chapter 3 - Voltammetry. B. Patel, *Electrochemistry for Bioanalysis* (p. 27-50). Elsevier.

Verma, P., Maire, P. & Novák, P. (2010). A review of the features and analyses of the solid electrolyte interphase in Li-ion batteries. *Electrochimica Acta*, *55*(22), 6332-6341.

Wang, J., Raistrick, I. & Huggins, R. A. (1986). Behavior of some binary lithium alloys as negative electrodes in organic solvent‐based electrolytes. *Journal of The Electrochemical Society*, *133*(3), 457-459.

Weeks, M. E. & Larson, M. E. (1937). JA Arfwedson and his services to chemistry. *Journal of Chemical Education*, *14*(9), 403.

Wei, C., Bard, A. J., Kapui, I., Nagy, G. & Tóth, K. (1996). Scanning electrochemical microscopy. 32. Gallium ultramicroelectrodes and their application in ion-selective probes. *Analytical chemistry*, *68*(15), 2651-2655.

Wei, C., Bard, A. J., Nagy, G. & Toth, K. (1995). Scanning electrochemical microscopy. 28. Ion-selective neutral carrier-based microelectrode potentiometry. *Analytical Chemistry*, *67*(8), 1346-1356.

Westbroek, P. (2005). 2 - Electrochemical methods. P. Westbroek, G. Priniotakis & P. Kiekens, *Analytical Electrochemistry in Textiles* (p 37-69). Woodhead Publishing.

Whittingham, M. S. (1976). Electrical energy storage and intercalation chemistry. *Science*, *192*(4244), 1126-1127.

Whittingham, M. S. (2004). Lithium batteries and cathode materials. *Chemical reviews*, *104*(10), 4271-4302.

Whittingham, M. S. & Gamble Jr, F. R. (1975). The lithium intercalates of the transition metal dichalcogenides. *Materials Research Bulletin*, *10*(5), 363-371.

Wikipedia. (2020). https://en.wikipedia.org/wiki/Electrochemical_stripping_analysis

Wikipedia. (2021a). *Diffusion Layer*. https://en.wikipedia.org/wiki/Diffusion_layer

Wikipedia. (2021b). *Squarewave voltammetry*. https://en.wikipedia.org/wiki/Squarewave_voltammetry

Williard, N., He, W., Hendricks, C. & Pecht, M. (2013). Lessons learned from the 787 Dreamliner issue on lithium-ion battery reliability. *Energies*, *6*(9), 4682-4695.

Winter, M., Barnett, B. & Xu, K. (2018). Before Li ion batteries. *Chemical reviews*, *118*(23), 11433-11456.

Winter, M. & Besenhard, J. O. (1999). Electrochemical lithiation of tin and tin-based intermetallics and composites. *Electrochimica Acta*, *45*(1-2), 31-50.

Wohlfahrt Mehrens, M., Vogler, C. & Garche, J. (2004). Aging mechanisms of lithium cathode materials. *Journal of power sources*, *127*(1-2), 58-64.

Xu, K. M. & Si, J. Y. (2007, 2007/08/01/). Development of Hg-Au Microelectrode for Measuring O_2, Mn^{2+}, Fe^{2+} and S_{2-} in Marine Sediment Pore Water. *Chinese Journal of Analytical Chemistry*, *35*(8), 1147-1150. doi: https://doi.org/10.1016/S1872-2040(07)60075-9

Xu, K. (2004). Nonaqueous liquid electrolytes for lithium-based rechargeable batteries. *Chemical reviews*, *104*(10), 4303-4418.

Xu, Y., Zhang, W., Shi, J., Zou, X., Li, Z. & Zhu, Y. (2016). Microfabricated interdigitated Au electrode for voltammetric determination of lead and

cadmium in Chinese mitten crab (Eriocheir sinensis). *Food chemistry*, *201(8)*, 190-196.

Yang, L., Wang, Y., Wu, J., Xiang, M., Li, J., Wang, B., Liu, H. (2017). Facile synthesis of micro-spherical $LiMn_{0.7}Fe_{0.3}PO_4/C$ cathodes with advanced cycle life and rate performance for lithium-ion battery. *Ceramics International*, *43*(6), 4821-4830.

Yang, S., Jia, J., Ding, L. & Zhang, M. (2003). Studies of structure and cycleability of $LiMn_2O_4$ and $LiNd_{0.01}Mn_{1.99}O_4$ as cathode for Li-ion batteries. *Electrochimica Acta*, *48*(5), 569-573.

Yao, P., Yu, H., Ding, Z., Liu, Y., Lu, J., Lavorgna, M., Liu, X. (2019). Review on polymer-based composite electrolytes for lithium batteries. *Frontiers in chemistry*, *7*, 522.

Yazami, R. & Touzain, P. (1983). A reversible graphite-lithium negative electrode for electrochemical generators. *Journal of Power Sources*, *9*(3), 365-371.

Yoshida, Z. (1981). Structure of Mercury Layer Deposited on Platinum and Hydrogen-evolution Reaction at the Mercury-coated Platinum Electrode. *Bulletin of the Chemical Society of Japan*, *54*(2), 556-561.

Yoshino, A. (2012). The birth of the lithium-ion battery. *Angewandte Chemie International Edition*, *51*(24), 5798-5800.

Yuan, X., Liu, H. & Zhang, J. (2011). *Lithium-ion batteries: advanced materials and technologies* CRC press.

Zaghib, K., Julien, C. & Prakash, J. (2003). *New trends in intercalation compounds for energy storage and conversion: Proceedings of the International Symposium* The Electrochemical Society (p. 28-32).

Zhang, L., Wu, H. B. & Lou, X. W. (2014). Iron-oxide-based advanced anode materials for lithium-ion batteries. *Advanced Energy Materials*, *4*(4), 1300958.

Zhao, J., Wang, L., He, X., Wan, C. & Jiang, C. (2008). Determination of lithium-ion transference numbers in $LiPF_6$–PC solutions based on electrochemical polarization and NMR measurements. *Journal of The Electrochemical Society*, *155*(4), A292.

Zhou, F., Unwin, P. R. 7 Bard, A. J. (1992). Scanning electrochemical microscopy. 16. Study of second-order homogeneous chemical reactions via the feedback and generation/collection modes. *The Journal of Physical Chemistry*, *96*(12), 4917-4924.

Zhu, G.-N., Wang, Y.-G. & Xia, Y.-Y. (2012). Ti-based compounds as anode materials for Li-ion batteries. *Energy & Environmental Science*, *5*(5), 6652-6667.

Zoski, C. G. (2015). advances in scanning electrochemical microscopy (SECM). *Journal of the Electrochemical Society*, *163*(4), 3088.

Zubi, G., Dufo-López, R., Carvalho, M. & Pasaoglu, G. (2018). The lithium-ion battery: State of the art and future perspectives. *Renewable and Sustainable Energy Reviews*, *89*(7), 292-308.